

STUDIES OF ORGANOMETALLIC AND BIOLOGICAL SYSTEMS WITH
FOURIER TRANSFORM ION CYCLOTRON RESONANCE
MASS SPECTROMETRY

By

GUI-HUA LISA LANG

A DISSERTATION PRESENTED TO THE GRADUATE SCHOOL OF THE
UNIVERSITY OF FLORIDA IN PARTIAL FULFILLMENT OF THE
REQUIREMENTS FOR THE DEGREE OF DOCTOR OF PHILOSOPHY

UNIVERSITY OF FLORIDA

1998

ACKNOWLEDGMENTS

Once an unprofessional fortune teller told me that my whole life would be smooth and easy because many people I would encounter in my life would help me achieve this smooth life. Although I have never believed the prediction, I still very much wanted it to be true from time to time, especially many times during my graduate studies. However, when the prediction failed to become true, I tended to think that no one had ever helped me in my whole life, and everything I had achieved so far was solely by my own effort. Of course, I was very wrong, and there are many special people in my life who have influenced and helped me to get on the path which takes me farther than I would pursue on my own. Since I could not possibly thank every one of them, I would like to take this chance to thank some of them from the bottom of my heart for being so “ordinary” in my life.

First of all, I would like to give my thanks to Dr. John R. Eyler, my advisor, and Dr. David E. Richardson for their patience, encouragement, and guidance. Although Dr. Eyler has always been busy with his chairmanship since I joined his group, he has always tried to find time for discussions and to provide his vital advice. I have learned abundantly from Dr. Richardson over the years, and his office door was always open to me whenever I needed help. Another person who needs to be acknowledged here is Dr. Cliff H. Watson. He taught me how to operate the instruments in the laboratory and some

necessary trouble shooting skills. I also want to thank Joy Trisha Mendez for providing all the electrospray samples used in chapter 6 and for her friendship.

Second, I want to express my sincere appreciation to one of my committee members, Dr. Nancy Denslow, from whom I learned a great deal in the area of biochemistry and biological mass spectrometry, especially during the time I was preparing my oral. My gratefulness also extends to other committee members: Dr. William Weltner Jr. for his professional and personal advice, Dr. Martin Vala for letting me using his outer office while I wrote, and Dr. Jim Winefordner for always being there.

Third, I want to thank Dr. Philip Brucat for his many inspirational talks during my writing and for his valuable advice. I want to acknowledge Dr. John George, my undergraduate advisor at Mary Washington College (MWC), for his guidance, advice, encouragement, and his belief in me, and Dr. George King, one of my physics professors at MWC, for his frequent important advice which changed me from a very shy person to an open, active person in my undergraduate years. My gratitude also goes to my high school counselors, Ms. Margaret Harmon and Ms. Phillis Land, for their countless instances of help.

Next, I salute Eyler's former group members, Yarjing, Nathan, Dil, Eric, Joe, Kevin, Rich, and Tom, and the current group members, David, Mark, Amy, and Stan, for their support. Beautiful warm friendships have helped me to get through numerous difficult times, so I want to thank a few special friends here. I want to thank Astra for all her support, for being a such good friend, and for being there whenever I am in crisis. I want to thank Clara for her sincere advice and for being a good listener during my graduate school years. I also want to express my sincere gratitude to Mukta who has

strengthened my Christian belief and shown me the power of prayers over the years.

Many thanks go to Sulin for being such a great English translator when I really needed one during my two years at Washington and Lee high school, and for being a great friend throughout these years.

I want to extend my appreciation to my dearest family and relatives who are a group of the most important people in my life. My whole life is in debt to my parents who have always been there for me and who were so understanding and forgiving for the mistakes I have made over the years. I am very grateful to my “Mom”(aunt) and “Dad” (uncle) for the opportunity they gave me, and for their financial support for my undergraduate education. Without them, my family would never have had the chance to come to the States, and thus I would never have had the opportunity to pursue my education in the States. I also want to thank my brothers, sisters, nieces, nephews, cousins, aunts, and uncles.

At last but not the least, I want to thank Joe Mannion for his love, patient, understanding, and endless support during this long writing process.

These people mentioned above are just some of those who have really made an impact on my life. Without them, I would not be who I am today. Just as the fortune teller predicted, my life so far has been made possible with many people being so “ordinary” in my life.

TABLE OF CONTENTS

ACKNOWLEDGMENTS	ii
LIST OF ACRONYMS	vii
ABSTRACT	ix
CHAPTERS	
1 INTRODUCTION	1
2 THEORY AND BACKGROUND	9
Ionization Techniques	9
Mass Analyzers	15
Dissociation Techniques	34
3 ADDITIVITY OF FLUORINE SUBSTITUENT EFFECTS IN RUTHENOCENE IONIZATION ENERGISTICS	39
Introduction	39
Experimental	41
Results and Discussion	45
Conclusion	52
4 INTRINSIC REACTIVITY OF METAL-HYDROXIDE COMPLEXES: GAS-PHASE REACTIONS OF $[\text{Cp}_2\text{ZrOH}]^+$ WITH ALCOHOLS, AMINES, ETHERS, ESTERS, AND AMIDES	53
Introduction	53
Experimental	54
Results and Discussion	57
Conclusion	73

5	INFRARED MULTI-PHOTON DISSOCIATION (IRMPD) STUDIES OF SMALL PEPTIDES IN THE GAS PHASE.	75
	Introduction	75
	Experimental	77
	Results and Discussion	81
	Conclusion	108
6	INVESTIGATING CHEMICALLY MODIFIED RIBONUCLEASE A WITH ESI-FTICR/MS	110
	Introduction	110
	Experimental	115
	Results and Discussion	118
	Conclusion and Future Work.	139
7	CONCLUSIONS AND FUTURE WORK	141
	REFERENCES	145
	BIOGRAPHICAL SKETCH	154

LIST OF ACRONYMS

CAD	Collisionally activated dissociation
Cp	Cyclopentadienyl
CRM	Charged Residue Model
CS	Capillary-skimmer
EI	Electron impact/ionization
ESI	Electrospray ionization
ETE	Electron-transfer equilibrium
FTICR/MS	Fourier transform ion cyclotron resonance mass spectrometry
FTMS	Fourier transform ion cyclotron resonance mass spectrometry
HPLC	High pressure liquid chromatography
IEM	Ion Evaporation Model
IRMPD	Infrared multiphoton dissociation
MALDI	Matrix assisted laser desorption ionization
MCp ₂	Metallocene structure
MS ⁿ	MS/MS experiment or multistage tandem mass spectrometry
MS	Mass spectrometry
m/z	Mass-to-charge
MWC	Mary Washington College

NMR	Nuclear magnetic resonance spectroscopy
NHS-acetate	N-hydroxysuccimide acetate
PD	Photodissociation
rf	Radiofrequency
RNase A	Ribonuclease A
REU	Research experience for undergraduate students
SORI-CAD	Sustained off-resonance irradiation collisionally activated dissociation

Abstract of Dissertation Presented to the Graduate School
of the University of Florida in Partial Fulfillment of the
Requirements for the Degree of Doctor of Philosophy

STUDIES OF ORGANOMETALLIC AND BIOLOGICAL SYSTEMS WITH
FOURIER TRANSFORM ION CYCLOTRON RESONANCE
MASS SPECTROMETRY

By

Gui-hua Lisa Lang

December 1998

Chairperson: Professor John R. Eyster
Major Department: Chemistry

Fourier transform ion cyclotron resonance mass spectrometry (FTICR/MS) equipped with various ionization techniques such as internal and external electron impact (EI) and electrospray ionization (ESI) has been employed for gas phase studies of two different classes of molecules: organometallic and biological.

One of the organometallic studies determined the free energies of ionization ($\Delta G_{i,350}^\circ$) for eight ruthenium complexes with the general formula $(\eta^5\text{-C}_5\text{Me}_5)(\eta^5\text{-C}_5\text{Me}_{5-n}\text{F}_n)\text{Ru}$ with $n = 0 - 5$. This study was accomplished using an internal EI technique in combination with electron-transfer equilibrium (ETE) reactions. The additivity of fluorine substituent effects in ruthenocene ionization energetics was also investigated.

The other organometallic study investigated the reaction strength of Cp_2ZrOH^+ ($\text{Cp} = \eta^5\text{-cyclopentadienyl}$) with some selected alcohols, esters, ethers, amines, and

amides using an external EI approach. The ETE method was also applied here to determine the free energies of ionization ($\Delta G_{i, 350}^{\circ}$) for Cp_2ZrOR^+ complexes, and a relative $\Delta G_{i, 350}^{\circ}$ ladder was established. The external EI study produced improved results from an earlier internal EI approach, and a brief comparison of the two experiments is given.

One of two biological projects was to inspect the correlation between the gas phase fragmentation patterns of 14 peptides and the locations within the peptides of the arginine residue. Gas-phase peptide ions were formed by ESI and infrared multiphoton dissociation (IRMPD) produced by a CO_2 laser was used to fragment the ions in the trap. The fragmentation patterns obtained were compared with those from sustained off-resonance irradiation collisionally assisted dissociation (SORI-CAD).

The second system of biological interest studied in this work was a chemically modified ribonuclease A (RNase A). This work showed that ESI-FTICR/MS can provide rapid scanning of sample purity, successfully detect a single modification of RNase A with N-hydroxysuccinimide acetate (NHS-acetate), and accurately follow the denaturation and chemical digestion process performed on RNase A. Various gas-phase dissociation methods were attempted to dissociate the native and modified RNase A to pinpoint the exact location of the modification.

CHAPTER 1 INTRODUCTION

Fourier transform ion cyclotron resonance (FTICR) mass spectrometry (MS) has been a versatile and popular analytical tool since the introduction of the concept of FTMS by Comisarow and Marshall in the early 1970s.¹ The inventive combination of FT to MS removed many earlier restrictions such as low mass range, low mass resolving power, and slow scanning speed from which MS had suffered. Beside circumventing earlier limitations, FTMS provides ultrahigh resolution mass measurements, longer trapping time for ions in the cell, the ability to perform MSⁿ experiments, and the flexibility of interfacing with many ionization techniques such as electrospray ionization, laser desorption, matrix assisted laser desorption, traditional electron impact/ionization and chemical ionization. For comparison, FTICR/MS can trap ions for long periods of time (up to 5×10^4 seconds) compared to less than a microsecond ion lifetime for a time-of-flight mass spectrometer and a range of 10-100 microseconds for a quadrupole mass spectrometer. This luxury of long ion trapping times conveniently allows various ion manipulations such as ion-molecule reactions and multiple dissociation experiments in ion traps. Although FTICR/MS was originally used primarily for studies of gas-phase chemical reactions, improvements made over the past 10 years, especially the successful interfacing of the electrospray ionization (ESI) technique to MS in 1984 independently by Aleksandrov and co-workers² and Yarmashita³ has revolutionized the applications of MS.

Following the successful application of ESI methods, FTICR/MS has been extended into the biological field, and it has been shown capable of studying large molecules of biological interest. Due to its versatile applications in both gas phase ion/molecule reactions and biological areas, FTICR/MS is the ideal method for investigating organometallic and biological systems.

The FTICR/MS characteristic of long ion trapping time at low pressure ($\sim 10^{-9}$ torr) and the ability to repetitively empty the cell of previous reactants and products led to many gas phase reaction studies including ion-molecule reaction rate determination⁴ and measuring physical quantities such as collision complex lifetimes,⁵ equilibrium constants,⁶ electron affinities,⁷ and ionization potentials.⁸ At low pressure, ion clustering interferences are eliminated, and reactions are exclusively bimolecular.

The improvement of high mass range detection since the introduction of FTMS has enabled mass spectrometric studies of ion-molecule reactions involving many organometallic compounds. For example, the positive ion/molecule condensation chemistry of three organometallic compounds was reported by Parisod and Comisarow,⁹ the formation of organometallic ions in the gas phase by reaction of Rh^+ with alkanes was studied by Byrd and Freiser,¹⁰ and metal-switching reactions were discovered in which a metal ion displaces another metal bound in a metallocene structure (MCP_2).¹¹ In addition to this list, the thermodynamic properties for many organometallic compounds have been extensively investigated and reported by Ryan and Richardson.^{12,14}

Thermodynamic data are essential for truly understanding a chemical system and its reactivity. Although a large amount of thermochemical information has been obtained for many small organic and inorganic compounds, this type of information is limited for

larger and more complex organometallic compounds. Therefore, determination of thermodynamic data for organometallic compounds is needed to further their understanding.

The thermochemistry of organometallic species has recently gained increasing attention due to the possible importance of these compounds in catalysis. For example, copper, zinc, and many transition metal organometallic complexes play important catalytic roles in biological systems.¹⁵⁻¹⁹ Understanding these systems would help to explain their reaction pathways and catalytic mechanisms. Combining the electron-transfer equilibrium (ETE) method¹² to FTICR/MS can lead to a powerful technique for the study of organometallic systems in the gas phase and the derivation of useful thermodynamic information such as free energies of ionization and reaction equilibrium constants.

Although the development of the FTMS approach freed ICR mass spectrometers from many earlier limitations, expanding the available mass range from small molecules to larger ones, FTICR/MS could not be applied to solve biological problems until the introduction of new ionization techniques such as ESI and matrix assisted laser desorption ionization (MALDI).²⁰ One of the reasons that MS was not able to be applied to biological systems prior to the development of ESI and MALDI was the problem of introducing large ions into the gas phase without destroying their structures. This problem was not solved until the successful interfacing of ESI to MS. ESI and MALDI techniques are usually referred to as “soft” ionization techniques, which retain the structures of biomolecules and have high sensitivity, allowing detection of picomole-to-femtomole levels of material, thus enabling the direct analysis of biological fluids with a minimum amount of sample preparation. One difference between ESI and MALDI mass spectra is

that ESI generates multiple charge states while MALDI primarily generates singly charged molecular ions. The molecular weights of biomolecules can be read directly from a MALDI spectrum, while some simple calculations are required for deriving molecular weights for ESI spectrum. Since ESI produces multiple charge states, and MS detects m/z ratios, most of the mass-to-charge (m/z) ratios of large biomolecules appear in the 100 - 3000 m/z region of the mass spectrum. Generally, ESI-FTICR/MS provides higher mass resolving power than MALDI-FTICR/MS. Although the detailed mechanism of ion formation in the ESI process still remains under debate and speculation, a substantial amount of recent literature has shown that many weak associations in solution do survive the ESI process and transfer to the gas phase.²¹ Some of the weak associations which have been studied with ESI-FTICR/MS include noncovalent complexes such as enzyme-substrate, receptor-ligand, host-guest, intact multimeric proteins, DNA duplex and quadruplex species, oligonucleotide complexes with drugs and proteins, and protein-drug complexes.²²⁻²⁴

Due to the availability of various dissociation techniques in FTICR mass spectrometry, biomolecular ions can be fragmented in the gas phase for primary structure analysis. In addition to collision-assisted dissociation and MSⁿ analysis,²⁵ the combination of enzymatic digestion followed by MS detection of fragments has been successfully applied to sequence determinations of proteins.²⁶ The result of mass spectrometric analysis of proteolytic peptide mixtures, especially after high pressure liquid chromatography (HPLC) separation of the peptides, is called a mass-spectrometric peptide mapping. Given the ability to perform direct analyses of multicomponent proteolytic peptide mixtures (or peptide mapping), MS has already been demonstrated to be a

powerful method for the identification of covalent post-translational modifications^{27,28} and the unequivocal characterization of multiple chemical modification sites in proteins²⁹ by mapping differences between the expected and the observed primary structures. Such peptide mapping is very efficient compared with classical biochemical methods, in which each collected chromatographic fraction is sequenced by automated Edman degradation.³⁰

One problem with ESI/FTMS is that ionic buffers disturb the spraying process and compete with analyte molecules for charges. Some involatile substances can form a solid cage which prevents escape of the analyte from the evaporating droplet. Upper limits for common contaminants in protein solutions are about 1 mM for ionic salts and 0.01% for ionic detergents.³⁰ Therefore, desalting the sample, either by HPLC or dialysis, or simple dilution is usually needed prior to the sample introduction.

Throughout the work presented in this dissertation, the versatility of FTICR/MS has been demonstrated by applying the technique to study two series of organometallic complexes and two biological systems. Basically, the dissertation can be viewed as three separate sections: i) discussing the theory and applications of a FTICR mass spectrometer in chapter 2; ii) using FTICR/MS and ion-molecule reactions to investigate intrinsic properties of two sets of organometallic compounds reported in chapters 3 and 4; and iii) exploring FTICR/MS applications in the biological area with two biologically related projects presented in chapters 5 and 6.

Theoretical aspects of a mass spectrometer, especially the basic principles of FTICR, including derivation of the ion cyclotron frequency equation, ion motions in an ICR cell, and ion excitation and detection, will be briefly discussed in chapter 2. Essential components of a FTICR mass spectrometer such as the superconducting magnet, ultrahigh

vacuum chamber, ICR cell, and data processing station are presented. Ionization techniques such as electron impact used for organometallic studies and electrospray used for biological studies are also discussed in chapter 2. The two most commonly used theories for explaining electrospray ion formation are summarized in the electrospray ionization section.

Chapters 3 and 4 deal with organometallic studies. Chapter 3 summarizes the investigative results of free energies of ionization (ΔG_i°) for eight ruthenocene organometallic compounds with the general formula $(\eta^5\text{-C}_5\text{Me}_5)(\eta^5\text{-C}_5\text{H}_{5-n}\text{F}_n)\text{Ru}$ ($n = 0$ to 5), including two isomeric structures, obtained using the ETE method and FTICR/MS. The questions of ligand and substituent additivity for these eight metallocenes are addressed with the results obtained.

Chapter 4 investigates the catalytic reactivity of a zirconium hydroxide complex, Cp_2ZrOH^+ (Cp = cyclopentadienyl), with various organic families such as alcohols, esters, ethers, amines, and amides. In the ICR cell the organic reagents, admitted to the high vacuum through precision leak valves, reacted with zirconium hydroxide ions, which were produced using electron impact (EI) in an external source and transferred into the ICR cell. The reaction mechanisms were checked with isotopically labeled $\text{Cp}_2\text{ZrO}^{18}\text{H}^+$ complexes using a few alcohol and ester compounds. The relative energies of some Cp_2ZrOR^+ products were established by the ETE method and FTICR/MS. The results obtained from external EI and internal EI methods are briefly compared, and the logical reasons that contribute to the different reaction results from the two approaches are also speculated upon in chapter 4.

Chapters 5 and 6 demonstrate the strength of FTICR mass spectrometry in biological studies. One well known advantage associated with mass spectrometric analysis of biological compounds is time saving partial protein sequencing with multiple MS experiments. In the work reported in chapter 6, modifications of a protein with a known sequence have been sequenced and identified, but it is still impossible to sequence an unknown protein with only MS even though that is the ultimate goal for a structural mass spectrometrists. However, if more is known about how locations of amino acid residues within the proteins affect peptide fragmentation in the gas phase, it would make the ultimate goal more reachable. This relationship between gas phase peptide fragmentation patterns and the locations of amino acid residues in a protein was investigated, and the results obtained are reported in chapter 5. Small peptides with 3 to 6 amino acid residues were dissociated in the ICR cell with the infrared multiphoton dissociation (IRMPD) technique, a low energy dissociation method, after they were introduced into the vacuum by electrospray ionization. Each peptide contained at least one basic amino acid residue in its sequence to assure that each peptide was protonated so it could be delivered into the gas phase from solution. Other dissociation techniques, especially the sustained off-resonance collisionally activated dissociation (SORI-CAD) method,³¹ another low energy dissociation method, were also applied to these peptides for comparison purposes.

Chapter 6 illustrates the power of FTICR/MS in identifying modification of a protein by following the chemical modification of the enzyme ribonuclease A (RNase A). In this chapter, the advantage of FTICR/MS for rapid screening of the purity of a sample is demonstrated. Interpretation of the mass spectrum to identify post-modified proteins is elaborated, and the reasons that various gas phase dissociation techniques failed to

dissociate the protein are discussed. The development of a proper method for trying to identify the modification sites of the modified protein is addressed. The initial results obtained from a different approach, which combines the enzymatic digestion technique, reverse phase HPLC separation, and FTICR/MS, are reported.

CHAPTER 2 THEORY AND BACKGROUND

Mass spectrometry (MS) has become one of the most important physical methods in analytical chemistry today³² due to its high sensitivity and versatility. MS is one of the few methods that is entirely suitable for the identification or quantitative measurement of trace amounts of chemicals.³³ Three basic functions of a mass spectrometer include producing gas-phase ions from sample molecules with various ionization techniques in the source; separating and detecting gas-phase ions according to their mass-to-charge (m/z) ratio in the analyzer; and then processing the separated ions with different data processing techniques. Some selected topics which are relevant to this thesis will be discussed in the following sections: the EI and ESI ionization techniques, the basic principles of FTICR/MS, and four dissociation techniques.

Ionization Techniques

The initial step of the MS method is to produce ions which can be later transferred into the high vacuum to be analyzed. Conventionally, ions were produced using internal ionization technique such as electron ionization (EI) inside the mass spectrometer, where the ion analysis process also occurs. However, some recently developed external ionization methods, such as electrospray, produce ions at atmospheric pressure, although the ion analysis process still takes place in a vacuum. Some of the common ionization

techniques are summarized in **Table 2-1**³³ below. Since only internal and external EI and electrospray ionization techniques were used in this thesis, a more detailed discussion of these techniques will be given in the following sections.

Table 2-1.

Some common ionization methods

Ionization method	Sample preparation for ionization	Thermal input associated with ionization	Method category
EI	As vapor	Relatively high	Thermal
CI	As vapor	Relatively high	Thermal
FAB	Dissolved in matrix	Virtually none	Energetic particle bombardment
ICP Inductively Coupled Plasma	Usually dissolved in liquid, then ionized in argon plasma	Relatively high	Thermal
GD Glow Discharge	Usually solid, then ionized in high voltage discharge	Relatively high	Thermal
MALDI	Mixed with matrix	Virtually none	Energetic particle bombardment
ESI	Dissolved in solvent	Virtually none	Field desorption

Electron Ionization

Electron ionization, also known as electron impact (EI), was the first ionization method to be used routinely in mass spectrometry. It is still one of the most popular

techniques for initiating the study of gas phase ion-molecule reactions. The EI source is a small enclosure traversed by an electron beam which originates from a heated filament and is then accelerated through a potential of 30-70 eV into the source. Gas-phase molecules of interest in the source then interact with these electrons. As a result, some of the molecules lose an electron to form a positively charged ion, and some other molecules gain an electron to form a negatively charged ion. Depending on the polarity of the detector, either positive or negative ions can be detected. With this method, many molecular ions usually retain sufficient internal energy after ionization to decompose further to form fragment ions that can be used to characterize the structure of the neutral molecules. The excess energy can also be lost to the environment by introducing a time delay which allows the “hot” ions to react and transfer the excess internal energy to the background gases or a gas introduced into the cell for this purpose.

The basic ionization principles are essentially the same for both internal and external EI methods in FTICR/MS. The only difference is the initial location of ion formation. An internal EI technique produces ions within the homogeneous magnetic field while an external EI technique produces ions in a source region which is outside of the fringe field of the magnet. The ions produced with external EI have to be transferred into the analyzer using some type of ion guide or a series of optics. One of the advantages of using external EI is elimination of neutrals from the cell, which provides cleaner gas phase reactions, since only ions and not their parent neutrals are transferred to the cell. Pictorial diagrams of an internal and external EI setup are shown in **Figure 2-1**.

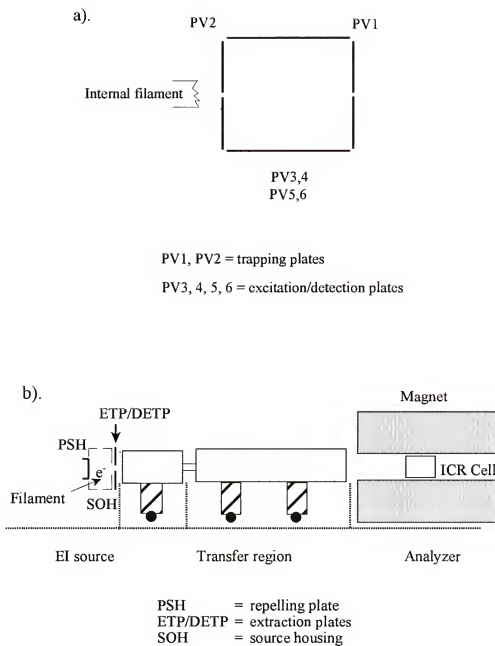


Figure 2-1.

Schematic diagram of Bruker's a) Internal and b) External EI source.

Electrospray Ionization

The first studies of the ESI phenomenon date back two and one-half centuries,³⁴ and extensive early studies of electrospray as an ionization method were done by Malcom Dole and co-workers in 1968.^{35,36} However, not until the successful interfacing of ESI (see **Figure 2-2**) to MS in 1984^{2,3} as a soft ionization technique to introduce structurally sensitive biological systems into the gas phase, did ESI become popular in the MS community.

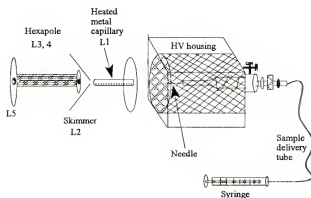


Figure 2-2.

Bruker's external ESI source with hexapole ion accumulation, heated metal capillary, needle housing, sample delivery tube, and syringe.

In the electrospray ionization process, the dissolved analyte molecule is protonated by the solvent and then delivered to the high voltage needle tip through a solution delivery tube. The syringe pump controls the flow rate to be in the range of 0.3-5 $\mu\text{l}/\text{min}$, and the analyte is usually sprayed at a concentration about 10^{-6} M in 49:49:2 methanol/water/acetic acid or acetonitrile/water/acetic acid. Addition of acetic acid to the ESI solvent assures sufficient protons to protonate basic analyte molecules and to provide

a stable spray current. Analyte ions emerge as a fine spray of charged droplets from the high electric potential (3 - 4 kV) needle at atmospheric pressure. As ions pass through the capillary into the high vacuum chamber which hosts the mass analyzer, the solvent in the charged droplets evaporates with the aid of the heated capillary or a countercurrent flow of a drying gas. The capillary is located about 1 cm away from the needle and kept around 100V. The production of positive or negative ions depends on the polarities of the needle and capillary. If the needle is positively charged, positive ions are produced, and the capillary is held at lower positive voltages to allow ions into the vacuum. Conversely, negative needle voltages produce negative ions, and a less negative potential on the capillary transfers the negative ions into the vacuum.

Although much research has been devoted to investigation of the mechanism of gas-phase ion formation in the ESI method (**Figure 2-3**),^{37,38} it is still very much under active study.

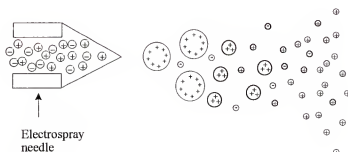


Figure 2-3.
ESI ionization mechanism

Currently, one of two main theories used to explain the mechanism of ion formation in ESI is the Charged Residue Model (CRM), originated by Malcolm Dole.^{35,36}

The other theory is the Ion Evaporation Model (IEM), proposed by Iribarne and Thomson.^{39,40} Dole's CRM is based on experiments conducted using dilute solutions of polystyrene molecules in a bath gas of nitrogen at atmospheric pressure. As the solvent evaporates from the charged droplets, the charge density on the droplets' surface increases until it reaches the Rayleigh limit.⁴¹ At this point, the Coulombic repulsive forces between the surface charges exceed the surface tension, resulting in division of the original charged drops. If the division process continues until each droplet contains only a single molecule which retains part of the original charge, the mass-to-charge ratios of these small droplets will be detected. However, aqueous electrolyte solutions do not easily lose dissolved ions due to an energy barrier, which is the electrostatic interaction between the ionic charge and the dipole of the surrounding solvent molecules. This energy barrier prevents the ion from leaving the surface. With a large number of experimental results, Iribarne and Thomson suggested that at a certain stage of the evaporation the net charge on the droplet with its small radius was sufficient to produce an electric field which was strong enough to give the ions an adequate potential energy to evaporate directly from the surface.

Mass Analyzers

After the ions are produced in the source region, they are transferred into the analyzer region through an ion guide or a series of electrical lenses; then a mass analyzer sorts the ions according to their m/z ratio and detects them. There are different mass analyzers which can be used to achieve this purpose, and some of the common ones are presented in **Table 2-2**. Since all data reported in this thesis were collected using FTICR mass spectrometers, the mass analyzer discussion will focus on only FTICR/MS.

Table 2-2.

Some common mass analyzers

Mass analyzer name	Quadrupole MS	Magnetic sector MS	Time of Flight MS (TOF/MS)	Ion trap MS (IT/MS)	Ion cyclotron resonance MS (ICR/MS)
Reference	Dawson, 1976 ⁴²	Duckworth, Barber, and Venkatasubramanian, 1988 ⁴³	Cotter, 1992; ⁴⁴ Vestal, Juhasz, and Martin, 1995 ⁴⁵	March, Hughes, 1989 ⁴⁶	Buchanan, 1991 ⁴⁷

Fourier Transform Ion Cyclotron Resonance Mass Spectrometry

Brief history. The beginning of FTICR/MS can be traced back to the early 1930s when the cyclotron accelerator was invented by Lawrence and Livingston.⁴⁸ Since then FTICR/MS has undergone numerous stages of development. In 1950, Sommer and Hipple developed the Omegatron,⁴⁹ which was the first cyclotron instrument designed to detect ions based on their mass-to-charge (m/z) ratio. In 1960, detection of cyclotron motion by a marginal oscillator which measured power absorption during excitation was introduced by Wobschall.^{50,51} However, the major breakthrough of FTICR/MS came in the mid 1970s when Comisarow and Marshall introduced Fourier transform (FT) analysis with pulsed and frequency sweep (chirp) excitation followed by broadband detection of an induced transient signal.^{52,53}

The introduction of FT/MS improved upon the earlier limitations of scanning ICR/MS, which included restricted mass range, low mass resolution, and slow scanning speeds. Now FTICR/MS is known for its ultrahigh mass resolving power, accurate mass measurement, wide mass range, simultaneous detection of all ions, ion remeasurement,

long ion storage time, high resolution ion isolation, and multistage tandem mass spectrometry (MSⁿ).⁵⁴

Although the hardware and software of the technique have changed over the years, the basic principles of FTICR/MS have stayed the same. Detailed descriptions of the basic principles can be found in many ICR papers,⁵⁵⁻⁵⁹ so only brief explanation will be given here.

Derivation of the ICR equation. FTICR/MS operates on the basis of the classical motion of ions under the influence of electric and magnetic fields. When a particle of mass m and charge q with initial velocity \vec{v} is placed in a magnetic field \vec{B} , it is influenced by the Lorentz force \vec{F}_L .

$$\vec{F}_L = q \vec{v} \times \vec{B} \quad (\text{Equation 2.1})$$

and a centrifugal force F_c .

$$F_c = \frac{m v^2}{r} \quad (\text{Equation 2.2})$$

where r is the radius of the helical path that the charged particle travels under the influence of a magnetic field.

As **Figure 2-4** shows, the magnitude of the Lorentz force must be equal to the magnitude of the centrifugal force in order to keep the ions in the cyclotron orbit. This means that equation 2.1 equals equation 2.2 to give equation 2.3.

$$q v B = \frac{m v^2}{r} \quad (\text{Equation 2.3})$$

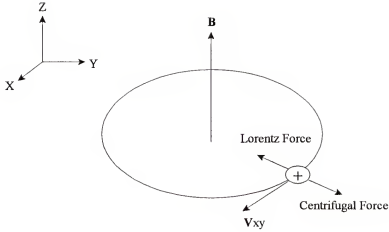


Figure 2-4.

Forces acting on a charged particle in a magnetic field.

Rearranging equation 2.3 gives equation 2.4, which gives an expression for the radius, r , of the cyclotron orbit,

$$r = \frac{m v_{\perp}}{q B} \quad (\text{Equation 2.4})$$

where v_{\perp} is the velocity component perpendicular to the magnetic field. Equation 2.3 can also be rearranged to give equation 2.5 below.

$$\frac{v_{\perp}}{r} = \frac{q B}{m} \quad (\text{Equation 2.5})$$

Since $\frac{v_{\perp}}{r}$ is the expression for angular frequency, ω_c , equation 2.5 can be used to derive the famous and fundamental ICR equation,

$$\omega_c = \frac{qB}{m}. \quad (\text{Equation 2.6})$$

It is also known that $\omega_c = 2\pi\nu_c$, so ion cyclotron angular frequency can also be expressed in linear frequency, ν_c .

$$\nu_c = \frac{q B}{2\pi m} \quad (\text{Equation 2.7})$$

According to equations 2-6 and 2-7, the value of an ion's cyclotron frequency in a known uniform magnetic (no electric) field is inversely related to its mass-to-charge ratio. Since frequency is a physical property which can be measured more accurately than any other, FTICR/MS provides ultrahigh mass measurement accuracy.

Ion motions in the ICR cell. If ions are initially formed along the magnetic field axis, they are confined radially by their ion cyclotron orbital motion. However, without any further restraint, ions would travel along a helical path and be lost from the homogenous region of the magnet along the direction of the magnetic field (usually defined as the z axis). In order to prevent ions from being lost in this direction, an electrostatic potential (or trapping potential) is applied axially to repel the ions back to the center of the ion trap, which is located in the most homogenous region of the magnetic field. The typical values of this electrostatic potential are 1-2 volts. This introduction of the trapping voltage achieves the purpose of keeping ions from escaping along the z-axis, but it also introduces unwanted effects including: the linear relationship between the ICR orbital frequency and the m/z ratio is no longer true, ICR line broadening and m/z shifting phenomena are introduced, and a new ion motion, the trapping ion motion, arises.

Squeezing ions axially is analogous to squeezing a balloon from two ends. When ions are forced back into the center of the trap from z-axis, they bulge out in the middle or radially in the trap. The outwardly pushing force that results from the trapping potential is exactly opposite in direction to the magnetic component of the Lorentz force. The net result of the new force is to reduce the "effective" magnetic field strength. Since the ion

cyclotron frequency, ω_c , is proportional to the magnetic field strength, introduction of the trapping potential will lower the observed ω_c .

The trapping voltage in any shape of an ion trap has been well approximated by a “quadrupolar” potential as in equation 2.8,⁶⁰

$$V(x,y,z) = V_T \left[\gamma - \left(\frac{\alpha}{a^2} \right) (x^2 + y^2 - 2z^2) \right] \quad (\text{Equation 2.8})$$

where V_T is the electrostatic trapping voltage applied to the trapping plates, α and γ are numerical constants that depend on the shape of the ion trap, and a is the ion trap dimension. Equation 2.9 gives the description of the Lorentz force in the presence of an electric field, \vec{E} ,

$$F_L = m \frac{d^2 \vec{r}}{dt^2} = m \frac{d\vec{v}}{dt} = q\vec{E} + q\vec{v} \times \vec{B} \quad (\text{Equation 2.9})$$

where \vec{r} is the vector position of the ion at time t . Substituting the resulting electric

field, $\vec{E} = -\vec{\nabla} V(x,y,z)$, from equation 2.8 into 2.9, three linear second-order

differential equations are derived to describe the motions of ions in a given magnetic and electrostatic trapping field. The equation involving only the z -coordinate can be solved independently to give the trapping frequency, ν_T , in equation 2.10.

$$\nu_T = \sqrt{\frac{q\alpha V_T}{\pi^2 m a^2}} \quad (\text{Equation 2.10})$$

The solutions for the two remaining differential equations in x and y give the other two types of ion motions: the ion cyclotron orbital motion, whose frequency is reduced to ω_c , (equation 2.11), and a natural magnetron motion with a frequency ω_m (equation 2.12).

$$\omega_{+} = \frac{1}{2} \left(\omega_c + \omega_c \sqrt{1 - \frac{m}{m_{crit}}} \right) \quad (\text{Equation 2.11})$$

where

$$m_{crit} = \frac{q a^2 B^2}{8 \alpha V_T} \quad (\text{Equation 2.11a})$$

$$\omega_{-} = \frac{1}{2} \left(\omega_c - \omega_c \sqrt{1 - \frac{m}{m_{crit}}} \right). \quad (\text{Equation 2.12})$$

Some typical experimental values for the three natural ICR motions (ion cyclotron orbital motion, trapping motion, and magnetron motion) in a 1 in. cubic cell are shown in **Table 2-3** to give one a good feel about the relative frequency contribution from each motion. The experimental conditions used to calculate the values in the table are: $a = 1.0$ in., $\alpha = 1.386$ for a cubic cell, $B = 3.0$ Tesla, and $V_T = 1.0$ V.

Table 2-3.

Natural ion motional frequencies (Hz) for singly charged ions trapped in a quadrupolar potential with a 3 Tesla magnetic field and 1.0 V electrostatic trapping field.⁶¹

Motion	m=100	1000	10,000	m _{crit} =50,492
$v_{+} \approx qB/2\pi m$	460,430	45,837	4,366	456
$v_{-} \approx \alpha V_T / \pi a^2 B$	228	229	240	456
$v_T \approx (\alpha q V_T / \pi^2 m a^2)^{1/2}$	14,496	4,584	1,450	645

ICR cells. As discussed in the last section, the ions have to be confined in a finite volume in order to be excited and detected in the homogenous region of the magnet. The confined dimension is achieved by using an ion trap which is known as the ICR analyzer cell or just ICR cell. For FTICR mass spectrometrists, the ICR cell is usually described as the heart of the FTICR mass spectrometer because it provides the three most important

functions: trapping or confining most of the ions by a static homogeneous magnetic field and an electrostatic trapping potential, exciting and/or ejecting their cyclotron motion by an alternating (r.f.) excitation electric potential, and detecting the image currents induced by the coherent ion cyclotron motion. Over the years, many different shapes of ICR cells^{54,62} have been designed to meet the researcher's specific need or to eliminate certain unwanted features of the cell. In the next three sections, I will discuss three different ICR cells: the standard cubic cell, the RF-shimmed infinity cell, and the dual-cell.

Standard Cubic ICR cell. The cubic cell⁶³ is the ancestor of ICR analyzer cells, and a diagram of a typical cubic cell is shown in **Figure 2-5**. As shown in the diagram, the cell is made of two trapping plates, two excitation plates, and two detection plates. The trapping plates are perpendicular to the direction of the magnetic field, and the small hole in the middle of each trapping plate allows ions or laser beams to enter the cell.

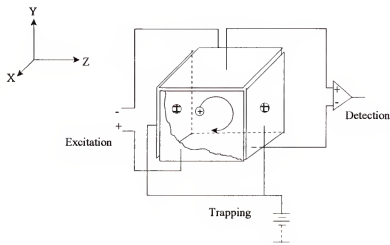


Figure 2-5.

A standard cubic ICR cell consists of six plates: front and back plates are excitation plates, top and bottom are detection plates, and left and right are trapping plates.

RF-shimmed infinity cell. A well defined operation of the excitation event in a FTICR pulse experiment is a crucial prerequisite for obtaining reliable relative signal intensities, good resolution for MS/MS selection, and optimum phase coherence of the excited ion packets. Therefore, finding a proper excitation method is on the minds of many research scientists, and one of the most successful examples is SWIFT,⁶⁴ which assumes a linear dependence of ICR signals with the excitation power. However, the linearity requirement cannot be fulfilled even in the simple case of an off-resonance single-frequency excitation pulse.⁶⁵ The non-linearity character can lead to ejection of ions along the magnetic field, and it arises from the coupling of axial and radial ion motions during the excitation event in standard ICR cells. The excitation of the axial ion motion is especially effective for frequencies equal to $2\omega_i$ ⁶⁶ and $\omega_c + 2\omega_b$ ⁶⁷ where ω_c is the cyclotron frequency, and ω_i is the trapping frequency. Improvements of trying to reduce the radiofrequency (rf) components of the excitation power, which are parallel to the magnetic field lines, were made separately by Marshall's⁶⁸ and Russell's⁶⁹ groups. In their studies, the guard ring principle, introduced in the early 1950s by Sommer et al.⁴⁹ for the Omegatron detector, was adapted. By properly adjusting the rf voltages applied to the individual guard wire or guard ring the rf excitation field can be shimmed to be nearly homogeneous within the ion trap. Although the ion excitation is somewhat optimized in this way, the sensitivity for detecting the image currents is reduced because the guard rings partially screen the detection electrodes. Introduction of rod electrodes⁶⁹ for the detection restores the peak current measurement, but the signal intensity is distributed over a series of odd harmonics of the cyclotron frequency, $k\omega_c$ where $k = 1, 3, 5, \dots$

The basic idea behind Infinity cells, reported by P. Caravatti and M. Allemann in 1991,⁷⁰ is to modify the electric excitation rf field of a cell of finite dimensions and to give

the ions an “illusion” of an infinitely long cell. The infinity cell eliminates the parallel component of the electric excitation rf field, which arises from the finite dimensions of ion traps, and achieves the “illusion” effect. As the Bruker Infinity cell shows in **Figure 2-6**, the standard trapping electrodes are replaced by a series of metallic segments, and these segments exhibit the potential contours of an imaginary plane perpendicular to the axis of an infinity long cylindrical cell. The outermost segments are capacitively coupled to the excitation rf on the adjacent excitation electrodes, and the connection of the different segments to an appropriate resistive voltage-divider chain provides the correct gradation of the rf potential across the trapping plate.

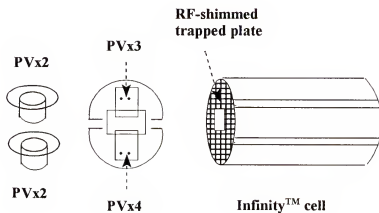


Figure 2-6.

Schematic diagram of the Bruker Infinity™ cell. PVx2, 3, and 4 are “side kick” plates.

Dual cell. The dual cell (see **Figure 2-7**) contains two cubic cells that share one trapping plate. These two cubic cells are connected to each other through a small orifice with a typical diameter of 2 mm. This arrangement provides the differential pumping between the high pressure cell (source) and the low pressure cell (analyzer) to give a pressure difference of 10^3 which leads to higher resolution. Ions are formed in the source

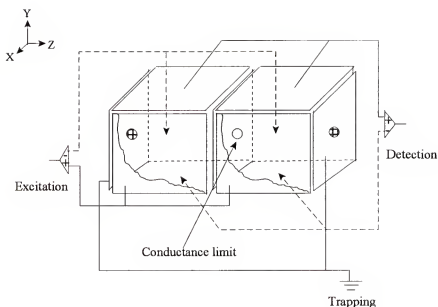


Figure 2-7.

A dual cell showing two excitation plates, two detection plates, two trapping plates, and the middle plate splitting two cells. The conductance limit connects two separated cells.

cell and then are transferred into the analyzer through the orifice in the common trapping plate.

In fact, each cell has all the features of a single cell. Providing that the common plate acts as one of the trapping plates of a single cell, each side of a dual cell can be used as an independent cell. If the common plate is grounded during ion formation, a statistical equilibrium of the ion population between the two cells is expected.^{47,58}

Excitation and detection of ion cyclotron motion. Excitation is a process to accelerate ions in the cell to larger cyclotron orbits by absorbing energy from an externally applied oscillating electric field (r.f.) of the same frequency. When ions are first generated, they have different kinetic energies. Therefore, when they enter the cell, ions of different size have different cyclotron radii, and ions with the same mass have different

phases of motion. When ions absorb the resonant r.f. energies, their cyclotron orbits increase, and they spiral outward (**Figure 2-8 b**). If ions of a given mass are irradiated long enough at their resonant frequencies, their cyclotron orbits eventually become large enough to strike the cell plates and be neutralized by the plates. The process of losing ions to the cell plates is referred as ion ejection or ion isolation. During the ion ejection/isolation process, unwanted ions are eliminated from the cell to provide a cleaner environment for the ions of interest. When the ions of interest are isolated, they are resonantly excited to larger orbits, and coherent ion motion is achieved at this time (see **Figure 2.8 c**).

After a group of coherently excited ions has been excited to larger orbits (but not large enough to be ejected from the cell), positive and negative charges will be induced on the detecting plates as shown in **Figure 2-8 d**. In this process, negative charges would be induced on the bottom plate from the proximity of the positive ions, and positive charges would be induced on the top detection plate. However, when the positive ions move away from the bottom detection plate and closer to the top plate, negative charges will be induced on the top detection plate while positive charges are induced on the bottom detection plate. Since the two detection plates are connected in a closed circuit, the result is an induced alternating current which is usually referred as the “image current”.

The image current is directly proportional to the ion density inside the ICR cell as given by equation 2.13,

$$I_s(t) = \frac{Nq^2rB}{ma} \sin \omega t \quad (\text{Equation 2.13})$$

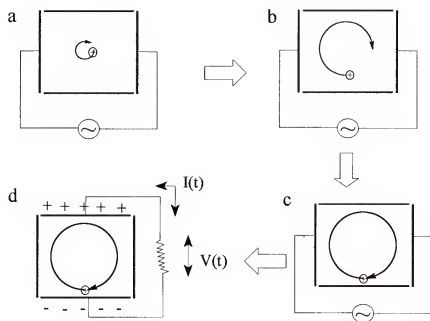


Figure 2-8.

Schematic diagram of ion excitation and detection. a) A positively charged particle moves in a cyclotron motion with a small radius. b) After the charged particle absorbs r.f. energy it increases its cyclotron radius. c) "Packed" ions move together in cyclotron motion after coherence is achieved. d) Image current $I(t)$ induced by the alternating positive and negative charges is converted to voltage and detected on the detection plates.

where $I_s(t)$ is image current, N is number of ions in the cell, and a is the dimension of the cell. However, the direct linear relationship between the ion density and the image current can be distorted if too many ions are inside of the cell due to the space charge effect. The image current is converted to a voltage, then the voltage is amplified by a preamplifier and digitized by an analog-to-digital converter. The voltage signal of each ion mass is given in the expression of equation 2.14,

$$V_s(t) = \frac{Nqr}{aC} \sin\left(\omega t - \frac{\pi}{2}\right) \quad (\text{Equation 2.14})$$

where $V_s(t)$ is the voltage signal, and C is the circuit capacitance. Due to ion-molecule collisions inside the cell, the signal recorded decays with time. The time domain signal is Fourier transformed to give a frequency spectrum which can be converted to a mass spectrum.

Ions are usually excited with one of three common types of excitation: (1) impulse excitation, (2) chirp excitation, or (3) stored waveform inverse Fourier transform (SWIFT) excitation.

Impulse excitation. In the impulse excitation technique,⁷¹ a peak voltage with an amplitude of more than 100 V and a pulse duration of about 0.5 μ s is applied to the excitation plates. During this short period of time, all ions in the cell are accelerated to larger cyclotron orbits. This method is good for exciting ions with a broad mass range.

Chirp excitation. In the chirp excitation method, all ions over the mass range of interest are resonantly excited by applying a fast-sweep rf excitation pulse to the excitation plates. The r.f. frequency is swept from the lowest to the highest frequencies to meet the requirements of the spectrum. This is a simple implementation to excite a wide mass

range without the need for high r.f. amplitudes as required in impulse excitation.⁷² The problem associated with this technique is that the power spectrum is non-uniform in amplitude. The non-uniform power spectrum causes an uneven excitation for ions of different m/z values, and the relatively broad frequency tailing on both sides of the power spectrum limits the frequency selectivity.⁵⁹

SWIFT waveform excitation. The SWIFT excitation technique⁶⁴ eliminates the problems associated with chirp excitation. Any desired excitation magnitude spectral profile can be specified as a discrete magnitude spectrum, and then inversely Fourier transformed to produce the corresponding time domain excitation waveform. The resulting excitation provides a optimally flat and selective excitation.

ICR experimental pulse sequence. A typical pulse sequence used in an FTICR experiment is given in **Figure 2-9**. The sequence starts with a quench pulse, which removes residual ions from previous experiments. Immediately following the quench pulse is an ion formation pulse which allows the ions to be produced and trapped in the analyzer. After the selected ions are isolated during an ion selection pulse, a short delay is added to let the isolated ions relax back to the center of the cell. Then, either a collision gas can be introduced to about 10^{-7} torr through the pulsed valve for a CID reaction, or a laser pulse can be turned on for a photodissociation experiment. Next, a variable reaction delay can be chosen which reduces the pressure in the analyzer to the original pressure of 10^{-9} torr. Finally, the ions of interest are excited and detected sequentially during the excitation and detection pulses.

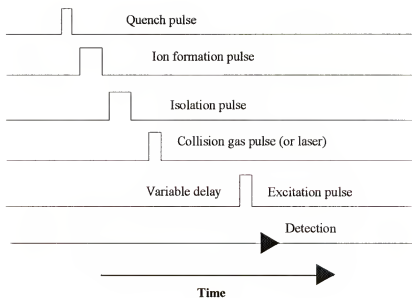


Figure 2-9.
Representation of a typical ICR pulse sequence.

Hardware. A FTICR mass spectrometer (see **Figure 2-10**) consists of four essential components: a solenoidal superconducting magnet, an ultra-low pressure vacuum system, an analyzer cell, and a data system.

Magnetic field. The (usually superconducting) magnet used in ICR/MS has a cylindrical opening in the middle where the ICR cell is located. Commercially available magnets which are commonly seen in the research laboratories come in various field strengths of 3 to 9.4 Tesla. Magnets with higher field strengths such as 14 T and 21 T have also been constructed in a few national laboratories. In general the higher the magnetic field strength, the better the mass spectrometer operating characteristics. Nine advantages associated with a higher magnetic field for FTICR/MS⁷³ are:

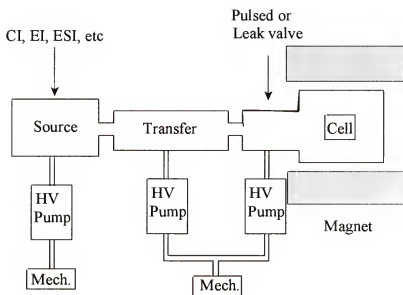


Figure 2-10.

Schematic diagram of a FTICR mass spectrometer with source, transfer, and cell regions.

1. The mass resolving power increases linearly with increasing the magnetic field, B .

$$\left| \frac{m}{\Delta m} \right| = \left| \frac{qB}{m\Delta\omega_c} \right| \quad (\text{Equation 2.15})$$

2. The mass resolving power for two dimensional FTICR spectra is improved by B^2 .
3. The speed of acquiring time-domain data with a given mass resolving power is linearly proportional to B . T is the data acquisition period.

$$\left| \frac{m}{\Delta m} \right| = 0.132 \frac{qBT}{m} \quad (\text{Equation 2.16})$$

4. Ion cyclotron kinetic energy increases quadratically with increasing magnetic field strength.

$$m \frac{v_c^2}{2} = \frac{q^2 B^2 r^2}{2m} \quad (\text{Equation 2.17})$$

5. The upper mass limit increases quadratically with increasing magnetic field strength. The variable a is a characteristic dimension of the trap, and α is a geometric factor determined by the trap shape.

$$\frac{m}{q} = \frac{a^2 B^2}{4\alpha V_T} \quad (\text{Equation 2.18})$$

6. The ion trapping efficiency is increased so ions can be held for longer period of time in the trap.

7. The ion density in the cell is also increased with increasing the magnetic field strength. n_{\max} is the maximum ion density.

$$n_{\max} = \frac{B^2}{8\pi m} \quad (\text{Equation 2.19})$$

8. Increasing magnetic field linearly improves the quadrupolar axialization⁷⁴ efficiency.
9. The maximum number of ions defined by onset of peak coalescence is proportional

to B^2 . (Maximum number of ions, above which two closely spaced resonances coalesce, is much less than the maximum number of ions that may be confined in a Penning trap.)

Ultra-high vacuum. In order to provide ultrahigh mass resolving power, FT mass spectrometers require ultra-low pressures ($\leq 10^{-8}$ torr) in the cell region. To achieve ultra-low pressures, differential pumping is most often used since a substantial pressure difference has to be achieved from atmospheric pressure, in which the ions are formed externally, to $\leq 10^{-8}$ torr in the cell where the ions are excited and detected. In the example given in **Figure 2-10**, the whole vacuum chamber is divided into three sections consisting of the source region ($\approx 10^{-6}$ torr), the transfer region ($\approx 10^{-7}$ torr), and the analyzer region ($\leq 10^{-8}$ torr). The source region hosts various external ionization techniques. The transfer region contains ion guides or electrostatic lenses which are used to guide externally produced ions into the ICR cell. The analyzer region holds the most important component of the instrument, the ICR cell. The respective pressure in each region can be achieved with various types of pumps such as oil diffusion pumps, turbo-molecular pumps, or cryopumps (liquid He). Although turbo-molecular pumps and cryopumps are commonly seen with the newer FTICR instruments, oil diffusion pumps are still being used on the older instruments. Details of the vacuum pumping setup for each FTMS instrument used in this thesis are provided in the proper experimental section of the chapter.

ICR cell. See discussion of ICR cells given earlier.

Data system. Different FTMS companies use different data acquisition and analysis systems to operate their mass spectrometers. For example, the Xmass software with a Silicon Graphics computer controls Bruker's FTMS instruments; an Odyssey data system interfaced with a Sun station operates the Finnigan FTMS instruments; and Ionspec uses PC computer systems for its instruments.

As the block diagram of a FTICR mass spectrometer in **Figure 2-11** illustrates, once the induced image current is detected in the ICR cell, it is converted to voltage, then the voltage is amplified with a preamplifier, digitized using an analog-to-digital converter (ADC), and stored in a computer to be processed later.

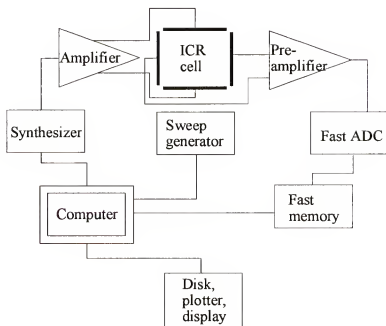


Figure 2-10.

A block diagram of a FTICR mass spectrometer.

Dissociation Techniques

The advantage of an ion trap MS is its capability of holding the ions in the trap for as long as 5×10^4 seconds prior to detection.⁷⁵ During this long trapping time, beside measuring molecular weights of ions, various gas phase reactions can be carried out with these trapped ions, such as MS^n experiments, collisionally activated dissociation (CAD) experiments, and ion-molecule reactions. The MS^n experiments combined with different CAD methods lead to extensive examination of the gas-phase reactions and ion

dissociation, which reveals useful structural information for precursor ions. In general, an MS experiment is carried out by applying a dissociation method to selected precursor ions to increase the internal energy of the ions. Subsequently, the precursor ions dissociate, and the fragment ions are excited and detected using the standard procedures. Ion activation can be achieved by several means summarized in **Table 2-4**. Only four dissociation methods are discussed with details below.

Collisionally Activated Dissociation

Collisionally activated dissociation, also known as collisionally induced dissociation (CID), was first introduced independently by Jennings⁷⁶ and McLafferty⁷⁷ in 1968. In a CAD experiment, the first step is to isolate ions of interest (or precursor ions) by ejecting unwanted ions using one of the excitation methods discussed earlier. Then the precursor ions are resonantly excited to a certain kinetic energy by a r.f. frequency. Next the activated ions react with a collision gas at a pressure 10^{-7} torr or higher, which is introduced into the analyzer cell through a pulsed valve. In this step, the collision process converts the translational energy of the precursor ions into internal energy, which is followed by a unimolecular decomposition to yield the products. After a short reaction delay time, all ions including the undissociated precursors and fragment ions are excited and detected. The CAD method has worked very well for small organic molecules, but it does not work well for large biological systems because the method can not convert enough translational energy to a desirable amount of internal energy to cause sufficient fragmentation of the biological precursor ions due to the very many degrees of freedom that a large biomolecule possesses.⁸⁸

Sustained Off-Resonance Irradiation Collisionally Activated Dissociation

The problem encountered by the CAD method as mentioned above can be eliminated with the SORI-CAD technique. In the SORI-CAD method, the precursor ions are excited by an off-resonance electric field with the irradiation frequency 500-2000 Hz away from the cyclotron frequency of the precursor ion. As a consequence, the ions can be activated and deactivated through multiple cycles with a period corresponding to the difference between the irradiation frequency and the natural cyclotron frequency of the ions. This multiple activation and deactivation cycle technique allows the ions to be irradiated or activated for longer periods of time without being ejected from the cell, and the precursor ions can also undergo multiple collisions with the collision gas to accumulate enough internal energy to cause sufficient fragmentation. The typical collision energy is less than 10 eV, so low energy fragmentation pathways can be accessed with SORI-CAD. SORI-CAD has been used to study fragmentation pathways of nucleotides⁷⁸ and the gas phase structures of proteins such as cytochrome C.⁷⁹ Disadvantages of SORI-CAD include the formation of off-axis product ions and the unwanted ejection of product ions that may fall into the region of the irradiation frequency.⁸⁰

Photodissociation

Photodissociation is the generation of fragmentation following absorption of photons, and it was initially applied to FTMS by Dunbar.⁸¹ In the PD method, ions absorb one or more photons until they gain sufficient energy to dissociate into fragments, so the primary requirement (or disadvantage) of the method is that the precursor ions must contain a chromophore which absorbs photons at the irradiating wavelength. Depending on the absorption wavelength of the chromophore, irradiation wavelength ranges from 193

nm for UV photodissociation to 10.6 μm for IR photodissociation. Applications of PD can be found in many fields of chemistry, ranging from studying the energetics of gas-phase dissociations of small ions⁸² to the sequencing of large mass oligonucleotides.⁸⁶

Table 2-4.

Some common dissociation techniques and their primary references

Dissociation technique	Relevant reference(s)
collisionally activated dissociation (CAD)	Jennings, 1968 ⁷⁶ , Haddon & McLafferty, 1968 ⁷⁷ , McLuckey 1992 ⁸³ , Cooks, 1995 ⁸⁴ , Cody, Burnier & Freiser 1982 ⁸⁵ .
multiple excitation collisional activation (MECA)	Williams, Henry, & McLafferty, 1990 ⁸⁶ , Guan, Hofstadler, & Laude, 1993 ⁸⁷ .
sustained off-resonance irradiation for collisionally activated dissociation (SORI-CAD)	Gauthier, Trautman, & Jacobson, 1991 ³¹ , Senko, Speir, & McLafferty, 1994 ⁷⁹ .
very low energy collision-induced dissociation (VLE-CID)	Boering, Rolfe, & Brauman, 1992 ⁸⁸ .
capillary-skimmer dissociation (CS)	Smith, 1990 ⁸⁹ , Little, 1994 ⁹⁰
surface-induced dissociation (SID)	Mabud, Dekrey, & Cooks, 1985 ⁹¹
electron-induced dissociation (EID)	Cody & Freiser, 1987 ⁹² , Gord, 1992 ⁹³ .
photodissociation (PD)	Chen, Hays, & Dunbar, 1984 ⁸¹ , Peiris, 1993 ⁹⁴ .
blackbody infrared radiative dissociation (BIRD)	Price, Schnier, & Williams, 1996 ⁹⁵

Capillary-Skimmer Dissociation

Capillary-skimmer dissociation, also known as nozzle-skimmer dissociation, has mainly been reported for studying large biomolecules.^{90,96} In this technique, the dissociation process takes place at relatively high pressures in the ESI source region where the high pressure allows a large number of low-energy collisions, resulting in ion

activation and subsequent dissociation of ions. The amount of dissociation of ions obtained from this method is influenced by the potential gradient difference between the capillary and skimmer, and the effective dissociation occurs within a certain potential difference. The product ions can result from various charge states of the molecular ions. Multiple dissociation experiments cannot be carried out using this technique because once the ions have left the external ESI source and are transferred into the analyzer cell, they can only be manipulated in the cell. However, other dissociation techniques can be used to gain further useful information about the fragmented ions resulting from the CS dissociation process.

CHAPTER 3

ADDITIVITY OF FLUORINE SUBSTITUENT EFFECTS IN RUTHENOCENE IONIZATION ENERGETICS

Introduction

Ionization energy is an important quantity for characterizing the thermodynamics of oxidation-reduction reactions for molecules.^{12,14} The thermochemistry of organometallic compounds has especially received increasing attention as researchers attempt to study thermodynamic contributions to reactivity and catalysis.⁹⁷ Studies have determined this intrinsic property for many atoms and organic molecules in the gas phase.⁹⁸⁻¹⁰⁰ However, ionization energies have been determined for far fewer organometallic compounds.

Traditionally, thermochemical quantities were measured with combustion reaction calorimetry¹⁰¹ and ionization energies were derived using photoelectron spectroscopy (PES).^{102,103} The vertical ionization energies determined by PES can only be an accurate measurement of the adiabatic gas-phase ionization energy if the differences in equilibrium geometries of the ion and neutral complexes are small,^{12,14} and any structural changes can result in a vertical ionization potential which is significantly different from the adiabatic ionization potential referenced at 0 K.¹⁰⁴ Therefore, if one is primarily interested in determining thermochemical quantities near room temperature, the electron-transfer equilibrium (ETE) method coupled to statistical mechanics has proven to be an attractive alternative to PES.^{12,14}

Mautner's group conducted early ETE studies of ion gas-phase ionization thermochemistry using pulsed high-pressure mass spectrometry (PHPMS).¹⁰⁵ In this technique, the K_{eq} for ETE can be extracted from a time plot of ion currents corresponding to the reaction equilibrium, which is established in a high pressure source following ion production by a pulsed high energy electron beam. The ETE reaction can also be followed using ion trap mass spectrometry such as FTICR/MS. As described in chapter 2 of this dissertation, FTICR/MS can trap ions for many seconds after the ions are produced and transferred into the trap. The ions in the cell are assumed to be nearly thermalized through hundreds of collisions within several seconds of trapping time in a 10^{-8} - 10^{-5} torr pressure range. This thermalizing process relaxes the ions back to center of the cell, and the thermalized ions can react more efficiently with the reaction reagents introduced through the leak valves.

The fluorine-substituted ruthenium complexes $(\eta^5\text{-C}_5\text{Me}_5)(\eta^5\text{-C}_3\text{F}_3)\text{Ru}$ (1)¹⁰⁶ and $(\eta^5\text{-C}_5\text{H}_5)(\eta^5\text{-C}_3\text{F}_3)\text{Ru}$ (2)¹⁰⁷ were synthesized and reported by Hughes and co-workers, and their gas-phase ionization free energies (ΔG_i°) were determined by Richardson and co-workers.¹³ The gas-phase ionization free energy study found that fluorine is not an unusual substituent as compared to the other halogens with moderately electron-withdrawing substituents. The γ parameter describes the effect of a given modified Cp ligand on the ionization energies for the d^6 and d^8 metallocenes. A γ value of 1.5 was obtained for the $(\eta^5\text{-C}_3\text{F}_3)$ ligand, indicating that five fluorine substituents raised the ionization free energy relative to $(\eta^5\text{-C}_5\text{H}_5)$. However, neither the effect of an individual fluorine Cp substituent on oxidation energetics, nor if the effects of multiple fluorine substituents are additive, are known at this time. Since a fluorine substituent possesses the

unusual combination of a strong electron withdrawing effect and significant electron donation to the ring, it cannot be assumed that the effect is additive. Furthermore, it is not known if ligand additivity can be assumed for $\eta^5\text{-C}_5\text{F}_5$ and any Cp derivative L in $(\eta^5\text{-C}_5\text{F}_5)(\text{L})\text{M}^{0/+}$ metallocene ionization energetics, as has proven to be the case for a few other ruthenocenes $\text{LL}'\text{Ru}^{0/+}$ (errors in predicted values ≤ 3 kcal/mol).¹⁰⁸

In the present work, the ETE method with FTICR/MS was chosen to investigate the free energies of ionization (ΔG_i°) in the gas phase for fluorine-substituted ruthenocenes with formulas $(\eta^5\text{-C}_5\text{Me}_5)(\eta^5\text{-C}_5\text{Me}_{5-n}\text{F}_n)\text{Ru}$ ($n = 1 - 5$) and for $(\eta^5\text{-C}_5\text{H}_5)(\eta^5\text{-C}_5\text{F}_5)\text{Ru}$ (**2**). The questions of ligand and substituent additivity for these eight metallocenes will be addressed with the results obtained.

Throughout this thesis, the ligand $\eta^5\text{-cyclopentadienyl}$ ($\eta^5\text{-C}_5\text{H}_5$) and its permethylated derivative $\eta^5\text{-pentamethylcyclopentadienyl}$ ($\eta^5\text{-C}_5\text{Me}_5$) are abbreviated as Cp and Cp*, respectively, and their structures are given in **Figure 3-1**. Representative structures of the fluorine substituted ruthenocenes are also shown in **Figure 3-1**.

Experimental

Material

All eight fluorinated ruthenocene samples studied in this project, with general formula $(\eta^5\text{-C}_5\text{Me}_5)(\eta^5\text{-C}_5\text{H}_{5-n}\text{F}_n)\text{Ru}$ ($n = 1$ to 5) and $(\eta^5\text{-C}_5\text{H}_5)(\eta^5\text{-C}_5\text{F}_5)\text{Ru}$, were provided by Russell P. Hughes of the Department of Chemistry, Dartmouth College. The compounds $(\eta^5\text{-C}_5\text{Me}_5)(\eta^5\text{-C}_5\text{F}_5)\text{Ru}$ (**1**),¹⁰⁶ $(\eta^5\text{-C}_5\text{H}_5)(\eta^5\text{-C}_5\text{F}_5)\text{Ru}$ (**2**),¹⁰⁷ and $(\eta^5\text{-C}_5\text{Me}_5)(\eta^5\text{-C}_5\text{H}_{5-n}\text{F}_n)\text{Ru}$ ($n = 1$ to 4)¹³ were prepared and reported by Hughes and coworkers. Nuclear magnetic resonance (NMR) spectroscopy and mass

spectrometry were used to check the purity of these samples. All the electron transfer reagents were purchased from Aldrich, and the liquid samples were degassed by several freeze-pump-thaw cycles prior to use.

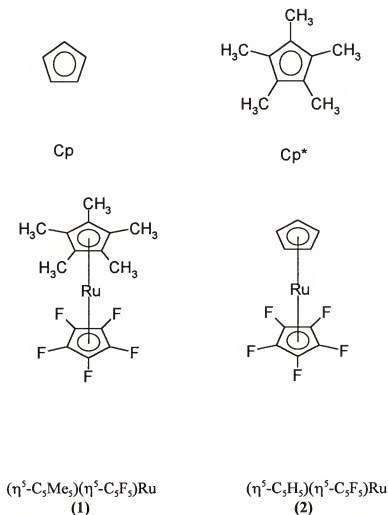


Figure 3-1.

A representative structure sketch for Cp, Cp*, (η⁵-C₅Me₅)(η⁵-C₅F₅)Ru (1), and (η⁵-C₅H₅)(η⁵-C₅F₅)Ru (2).

Mass Spectrometer

All experiments reported here were performed with an FTICR/MS instrument that included a 3.0 tesla horizontal bore, room temperature Oxford superconducting magnet

(Oxford Instruments, Cryomagnetic Systems, Osney Mead, Oxford OX2 ODX, England), a Nicolet FTMS-1000 vacuum system, and an IonSpec personal computer based data system. A schematic drawing of the instrument is given in **Figure 3-2**. The magnet had an inside diameter of 6 inches cylindrical opening; the vacuum system had an inside diameter of 2.875 inches; and the experiments in this project were done with a standard 1 inch cubic stainless steel ICR cell.

The vacuum chamber indicated in **Figure 3-2** was evacuated by an Alcatel 300 L/s oil diffusion pump which was fore-pumped by a mechanical pump, and it maintained a low 10^{-8} torr pressure. The ICR cell was located in the center of the homogenous magnetic field, and an internal filament assembly was located next to the ICR cell and on the opposite side from the solids probe. The inlet system was pumped by an Alcatel 150 L/s oil diffusion pump which was also backed by a mechanical pump. The inlet system was heated, with its temperature controlled at about 100°C. Liquid samples and solid samples with relatively high vapor pressures were introduced into the vacuum through two Varian precision leak valves contained in the sample inlet system. Solid samples with relatively low vapor pressures were admitted using a stainless steel solids insertion probe. The temperature of the solids probe was controlled to provide the proper sample pressure for the reactions of interest.

Due to the high stray magnetic fields, the nude ionization gauge used for measuring the pressure of the vacuum chamber was shielded with μ -metal and placed in a position away from the ICR cell. This configuration resulted in pressure measurements which were a factor of two lower than the true pressure at the FTICR cell when the gate valve of the 300 L/s pump was in a 1/4th open position.¹⁰⁹ Since all experiments were

conducted with the gate valve in its 1/4 open position, all pressures measured and used for rate constant calculations throughout the project were multiplied by a factor of two. The ionization gauge was connected to a Granville-Phillips digital ionization gauge controller.

The mass spectrometer was equipped with a bake-out controller which allowed the operator to heat the vacuum chamber between experiments to provide a clean vacuum for the next experiment. In the studies presented in this chapter, the vacuum chamber was baked-out for ca. 8 hours between studies on different samples.

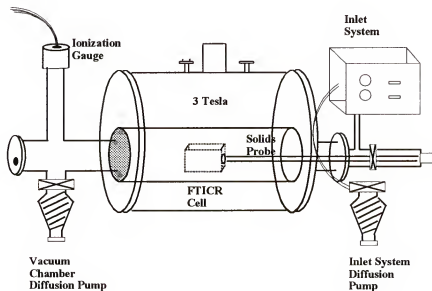


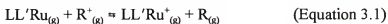
Figure 3-2.

Schematic diagram of 3 telsa FTICR instrument including standard cubic analyzer cell, nude ionization gauge, solids probe, and inlet system.

Results and Discussion

Sample Preparation

In this project, the ETE method was used for investigating the thermal equilibrium reactions of the eight ruthenocene compounds with several organic reference compounds. (See **Figure 3-3**). The FTICR/MS instrument was used to follow the general reaction represented by equation 3.1, where $LL'Ru_{(g)}$ is the ruthenocene compound of interest, R is the reference compound, and L and L' are the ligands of the ruthenocene compounds.



The ruthenocene derivatives were sublimed from the solids probe to give partial pressures in the 1×10^{-7} - 1×10^{-6} torr range. For all of the ruthenocene derivatives additional heating of the solids probe was required to generate partial pressures of the neutrals in the 1×10^{-7} torr range. All the reference compounds were admitted to the vacuum through a Varian precision leak valve, and the molecular ions were produced by internal electron impact. The number of ions generated was controlled by the electron energy and the electron current of the filament to provide good ion signals with minimal unwanted fragment ions. Electron-transfer equilibrium was established for the ruthenocene derivatives and the reference compounds when the product ion intensities reached a constant ratio. Even though the equilibrium was usually established in less than 2 seconds, the reaction was monitored for another 10-13 seconds to ensure true equilibrium.

Data Treatment

The reaction free energies (ΔG_{et}°) were determined using equation 3.2. The temperature of the ICR cell was previously determined to be 350 K with an Omega RTD

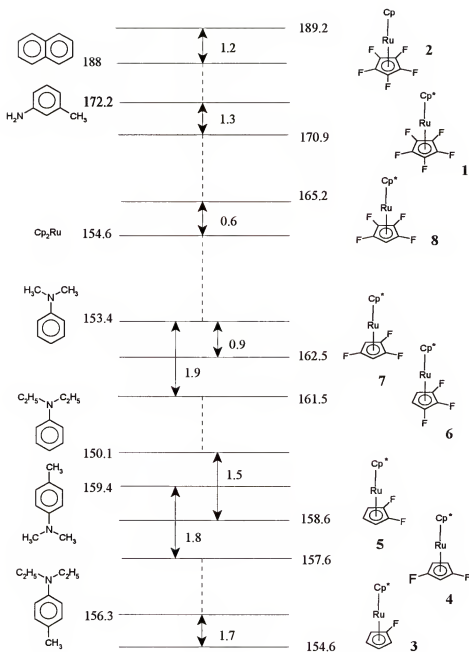


Figure 3-3.

Free energy ladder. Reference compounds are on the left. $\Delta G_{\text{et}}^{\circ}$ and $\Delta G_{\text{I}, 350}^{\circ}$ values are on the right. All energies are in kcal mol⁻¹.

thin film detector,¹⁰⁸ and this temperature was used in the free energy calculations.

$$\Delta G_{\text{et},350\text{K}}^{\circ} = -RT \ln K_{\text{eq}} = -RT \ln \{[I(\text{M}^+)\text{P}_{\text{R}}]/[I(\text{R}^+)\text{P}_{\text{M}}]\} \quad (\text{Equation 3.2})$$

The reactant ions and neutrals were allowed to equilibrate at the known pressures $\text{P}_{\text{LL,Ru}}$ and P_{R} , and the ion populations (I) in the analyzer cell were determined from the mass spectrum. If the free energy of ionization ($\Delta G_{\text{i},350\text{K}}^{\circ}$) for the reference compound (R), is known, then the corresponding energy for the ruthenocene compound can be obtained from equation 3.3.

$$\Delta G_{\text{i},350\text{K}}^{\circ}(\text{M}) = \Delta G_{\text{i},350\text{K}}^{\circ}(\text{R}) + \Delta G_{\text{et},350\text{K}}^{\circ} \quad (\text{Equation 3.3})$$

Previously reported $\Delta H_{\text{i}}^{\circ}$ values and estimates of $\Delta S_{\text{i}}^{\circ}$ for the reference compounds have been used to derive $\Delta G_{\text{i},350\text{K}}^{\circ}(\text{R})$ values at 350 K.^{105,110-112} The pressures for neutrals were obtained directly from the N_2 -calibrated ion-gauge reading and were likely to be low for both the metallocenes and the reference compounds. However, the assumption was made that the reference compounds and the metallocenes have similar ion gauge sensitivities and system factors so that the equilibrium constants, which depend on the pressure ratios, could be obtained with acceptable accuracy. Previous pressure calibration studies in our laboratory¹⁰⁸ showed that the assumption is approximately true for the reference compounds and for non-fluorinated metallocenes if the pumping speed in the main chamber is reduced substantially. Thus, the relative ionization free energies are estimated to be accurate within $\pm 0.5 \text{ kcal mol}^{-1}$. Due to pressure errors, it is estimated that the absolute errors are $\pm 1.5 \text{ kcal mol}^{-1}$. Note that an unusually large pressure ratio error of 5/1 would lead to an error of $\pm 1.1 \text{ kcal mol}^{-1}$ in $\Delta G_{\text{et}}^{\circ}$ at 350 K.

Free Gas-Phase Ionization Energies ($\Delta G_{\text{et}}^{\circ}$) of the Eight Fluorine Substituted Ruthenocenes

Typical results for the ETE experiments with the ruthenocenes and the organic reference compounds are shown in **Figure 3-4**. These data were collected with a total pressure of 2.7×10^{-7} torr and a $\text{Cp}^*\text{RuC}_6\text{HF}_4$ to Cp_2Ru ratio of 1.3:1. The $\Delta G_{\text{i},350}^{\circ}$ value of $\text{Cp}^*\text{RuC}_6\text{HF}_4$ is $165.2 \text{ kcal mol}^{-1}$. The measured $\Delta G_{\text{i},350}^{\circ}$ values for the ETE reactions of all eight fluorine substituted ruthenocenes with various reference compounds are also shown in **Figure 3-3** as a free energy ladder. The derived values of $\Delta G_{\text{i},350}^{\circ}$ are displayed next to the compounds in the ladder. The value obtained in this work for **1** agrees within $\pm 0.1 \text{ kcal/mol}$ with that reported earlier.¹³ Typical calculations of K_{eq} , $\Delta G_{\text{et}}^{\circ}$ and $\Delta G_{\text{i},350}^{\circ}$ values are illustrated with the reaction of $\text{Cp}^*\text{RuC}_6\text{HF}_4$ and Cp_2Ru in equation 3.4. The reference reagents were first ionized with internal EI to give Cp_2Ru^+ . Then the Cp_2Ru^+ ions reacted with $\text{Cp}^*\text{RuC}_6\text{HF}_4$ sublimed from the solids probe. The reaction equilibrium was achieved within 8 seconds of reaction delay as shown in **Figure 3-4**.



A plot of $\Delta G_{\text{i},350}^{\circ}$ vs the number of fluorines, n , in $(\eta^5\text{-C}_5\text{Me}_5)(\eta^5\text{-C}_5\text{Me}_{5-n}\text{F}_n)\text{Ru}$ ($n = 0 - 5$) is shown in **Figure 3-5**. The data points form a straight line with a slope of $3.7 \pm 0.5 \text{ kcal mol}^{-1} n^{-1}$ (95% confidence interval) and $r^2 = 0.96$. The results show that fluorine substituent effects are essentially additive, with each additional fluorine raising the ionization energy by $\sim 3.7 \text{ kcal mol}^{-1}$.

γ Parameter of Ligand Substituent Effect

The parameter γ , developed earlier by Ryan et.,¹⁰⁸ describes the effect of a given modified Cp ligand on the ionization energetics for the d^6 (and d^8) metallocenes. This

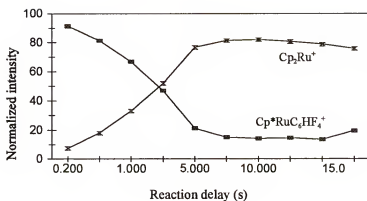


Figure 3-4.

A typical ETE experiment of the reaction of $\text{Cp}^*\text{RuC}_6\text{HF}_4$ and Cp_2Ru complexes.

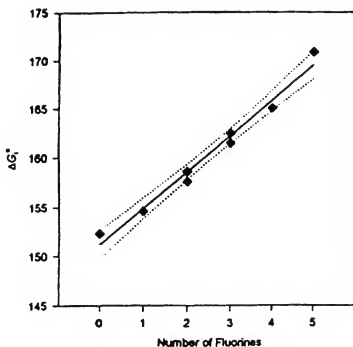


Figure 3-5.

Plot of $\Delta G_{i, 350}^\circ$ values vs number of fluorines. The solid line is the linear regression, and the dotted lines are 95% confidence intervals.

parameter is assigned to the entire ligand rather than any particular substituent since the sum of individual substituent parameters does not necessarily describe the effect of multi-substituted Cp ligands accurately. However, an additive ligand effect is assumed so that the effect of two different Cp ligands is assumed to be described by the sum of the individual γ parameters.

Table 3-1.

Free Energies of Ionization and Derived $\gamma(L)$ Values

Ligand	$\Delta G_{i,350}^{\circ}$ (kcal mol ⁻¹)	$\gamma(L)$
$\eta^5\text{-C}_5\text{H}_5$	152.3	0 (defined)
$\eta^5\text{-C}_5\text{H}_4\text{F}$	154.6	0.23
$\eta^5\text{-1,3-C}_5\text{H}_3\text{F}_2$	157.6	0.46
$\eta^5\text{-1,2-C}_5\text{H}_3\text{F}_2$	158.6	0.54
$\eta^5\text{-1,2,3-C}_5\text{H}_2\text{F}_3$	161.5	0.76
$\eta^5\text{-1,2,4-C}_5\text{H}_2\text{F}_3$	162.5	0.84
$\eta^5\text{-C}_5\text{HF}_4$	165.2	1.0
$\eta^5\text{-C}_5\text{F}_5$	170.8	1.5 (1.7 \pm 0.2) ^a

^a See text for discussion

The general equation formulated to derive γ parameters is given in equation 3.5

$$\Delta G_i^{\circ}(L'LM) = a (\gamma_L + \gamma_{L'}) + \Delta G_i^{\circ}(\text{Cp}_2\text{M}) \quad (\text{Equation 3.5})$$

with L and L' as Cp derivatives and a as a "sensitivity constant" which depends on the metal M. $\Delta G_i^{\circ}(\text{Cp}_2\text{M})$ is ionization free energy of Cp_2M . For ruthenium metal, the previously determined constant a is 13.0¹⁰⁸ and $\Delta G_i^{\circ}(\text{Cp}_2\text{M})$ is 164.6 kcal mol⁻¹. With the experimentally determined ΔG_i° values given in **Table 3-1**, γ parameters for Cp derivatives in ruthenocenes can be determined using equation 3.6 by defining $\gamma(\text{Cp}^*) = -1$ and $\gamma(\text{Cp}) = 0$. The defining values of $\gamma(\text{Cp}^*) = -1$ and $\gamma(\text{Cp}) = 0$ imply that a negative value for γ_L means that a ligand L stabilizes the ionized form of the metallocene relative to the neutral, lowering the ionization energy.

$$\Delta G_i^\circ(\text{L L'M}) = 13.0 (\gamma_L + \gamma_{L'}) + \Delta G_i^\circ(\text{Cp}_2\text{Ru}) \quad (\text{Equation 3.6})$$

The derived γ values for the fluorinated Cp derivatives are tabulated in **Table 3-1** along with that of Cp for comparison. As **Table 3-1** shows, the overall trend is clearly additive with respect to F substituent effects. However, some small but reproducible deviations from additivity are observed. For example, when $n = 2$ or 3 , the two structural isomers appear to have about 1 kcal mol^{-1} difference in ΔG_i° values, but no particular trend is noticed with respect to the isomer structures. Further examination of **Table 3-1** reveals a larger jump in the ionization free energy values for $n = 4$ to 5 ($5.7 \text{ kcal mol}^{-1}$) than the rest. But the jump is still within the 95% confidence interval as **Figure 3-5** shows, and it may represent a “perfluoro” effect.¹⁰³ Since that effect is small enough, it may be accounted for by experimental error.

With the ΔG_i° value obtained from this study and the previous definition of $\gamma(\text{Cp})$ being 0, $\gamma(\eta^5\text{-C}_5\text{F}_5)$ is determined to be 1.9 for $\eta^5\text{-C}_5\text{F}_5$ with Cp as the other ligand using equation 3.6. However, $\gamma(\eta^5\text{-C}_5\text{F}_5)$ is 1.5 if the other ligand is Cp*. Since C_5Me_5 is a more electron-rich ligand than C_5H_5 , it is expected to reduce the ionization energy-raising effect of $\eta^5\text{-C}_5\text{F}_5$ more effectively than Cp itself. However, the number of systematically studied compounds with respect to ligand additivity is small, and the poorest additivity observed previously ($\text{L} = \text{indenyl}$)¹⁰⁸ also has a large range for its value of γ (-0.4 ± 0.2). With this small ligand additivity effect (the range of $\gamma(\text{C}_5\text{F}_5) = 1.7 \pm 0.2$ based on the two $\eta^5\text{-C}_5\text{F}_5$ metallocenes studied to date), it can be concluded that $\eta^5\text{-C}_5\text{F}_5$ is not unusual with respect to additivity.

Conclusion

The free energies of ionization for seven fluorine substituted ruthenocenes, $(\eta^5\text{-C}_5\text{Me}_5)(\eta^5\text{-C}_5\text{Me}_{5-n}\text{F}_n)\text{Ru}$ ($n = 1 - 5$), and $(\eta^5\text{-C}_5\text{H}_5)(\eta^5\text{-C}_5\text{F}_5)\text{Ru}$ (**2**) were investigated and determined with the ETE method, and the values ranged between 152.3 and 170.8 kcal/mole. $\eta^5\text{-C}_5\text{H}_5$ has the lowest gas-phase free ionization energy while $\eta^5\text{-C}_5\text{F}_5$ has the highest gas-phase free ionization energy. The results of this study show that each additional fluorine raises the ionization free energy by 3.7 ± 0.5 kcal mol⁻¹, and the energy difference between the two possible isomers for $n = 2$ and $n = 3$ was found to be less than or equal to 1 kcal mol⁻¹. This study suggests that the intrinsic effect of each fluorine substituent on ionization energy is additive without any unusual effect observed. The large jump from $n = 4$ to 5 (5.7 kcal mol⁻¹) may represent a “perfluoro” effect, but the effect is small and may be accounted for by experimental error.

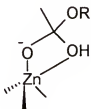
CHAPTER 4
INTRINSIC REACTIVITY OF METAL-HYDROXIDE COMPLEXES:
GAS-PHASE REACTIONS OF $[\text{Cp}_2\text{ZrOH}]^+$ WITH ALCOHOLS,
AMINES, ETHERS, ESTERS, AND AMIDES

Introduction

Many transition-metal compounds have been known to catalyze biopolymer cleavage in solution. This catalytic property could provide insights into methods for gas-phase fragmentation of peptide and ester bonds since the rapid cleavage of esters has usually been a prerequisite for catalysis of peptide bonds and phosphate ester hydrolysis in solution-phase studies. Metal-bound hydroxides are found in a variety of synthetic and biological catalysis that are active in hydrolysis of carboxylic acid and phosphoric acid derivatives. Many transition-metal complexes such as those containing palladium(II),¹⁵ zinc(II),¹⁶ cobalt(III),¹⁷ and copper(II)¹⁹ have been found to be important catalysis in biological systems for the cleavage of RNA, DNA, amides, and carboxylic and phosphate esters. In general, the pH dependence of catalysis can be used to show that a hydroxide complex ($\text{L}_x\text{M-OH}^n$) or its kinetic equivalent is responsible for the observed reactivity.

In reactions with activated esters (those with good leaving groups), metal hydroxides act as typical O-donor nucleophiles, and the reactivity is generally predictable from the pK_a of the metal-bound water.¹¹³ With unactivated substrates (which are better models for biological substrates), rates of catalyzed hydrolysis can be unusually high, and

the concept of bifunctional catalysis can be invoked in which a nucleophile (hydroxide) and an electrophile (the metal center) are in close proximity and can act in tandem to increase the catalytic reaction rate (e.g., via a zinc bound intermediate shown here).



The zirconium-hydroxide complex (Cp_2ZrOH^+) is a 14-electron zirconium(IV)-hydroxo complex which could serve as a model for bifunctional catalysis with the potential for gas-phase studies to reduce the complexity of the system. Its chemical features are similar to known solution catalysts (i.e., the metal center is not coordinatively saturated and is strongly electrophilic), and this suggests that it would be quite reactive. Coordinative unsaturation can lead to rapid binding of Lewis basic substrates since ligand displacement need not occur. Therefore, the zirconium-hydroxide complex has been chosen as a model to study the reactivities of metal-bound complexes. In this chapter, the results obtained from the investigation of the intrinsic reactivity of the Cp_2ZrOH^+ complex with various organic groups such as alcohols, esters, ethers, amines, and amides in the gas phase with FTICR/MS are reported and discussed.

Experimental

Materials

The complex $\text{Cp}_2\text{Zr}(\text{CH}_3)_2$ was obtained from Professor Richardson's laboratory in the Inorganic Division of the Chemistry Department at the University of Florida. Since

the $\text{Cp}_2\text{Zr}(\text{CH}_3)_2$ sample was sensitive to moisture in the air, it was kept in a dry box until it was ready to be transferred into the ionization chamber. All organic reagents except 4-nitrophenyl acetate, which was recrystallized by Celeste Regino in the Inorganic Chemistry Division at the University of Florida, were commercially purchased and used without further purification.

Mass Spectrometer

All experiments in this project were performed with a FTICR/MS instrument which consists of a 3.0 Tesla Oxford superconducting magnet (Oxford Instruments, Cryomagnetic Systems, Osney Mead, Oxford OX2 ODX, England), a Bruker external source vacuum chamber (Bruker Analytical Systems, Inc., Billerica, MA), and an Aspect 3000 data system. The schematic diagram of the instrument is given in **Figure 4-1**. The vacuum chamber of the instrument is divided into three separately pumped regions: source, ion transfer, and analyzer. In the source region, various types of ionization techniques such as external electron ionization and chemical ionization take place, and this region is evacuated to about 10^{-6} torr with a 330 l/s Balzer turbomolecular pump which is forepumped by a mechanical pump. The ion transfer region contains the electrostatic lenses which guide ions into the analyzing chamber, and it is pumped by a 70 l/s Balzer turbomolecular pump (Balzers, Hudson, NH). Finally, the analyzer region, which contains the rf-shimmed InfinityTM cell, is evacuated to a base pressure in the low 10^{-9} torr range using a 330 l/s Balzer moleculararturbo pump. The turbomolecular pumps of the ion transfer region and the analyzer region share one mechanical pump. The source chamber is connected to the main vacuum with a small orifice which can be blocked by a manual gate valve. All sample inlet valves and the solids probe loading port are pumped by an Edwards mechanical pump.

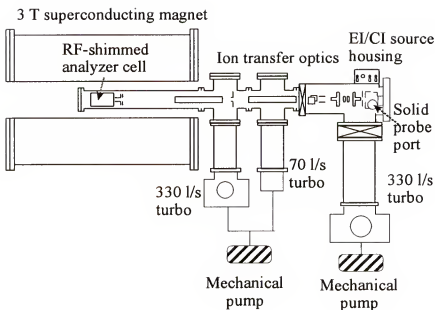


Figure 4-1.

Schematic diagram of the FTICR mass spectrometer including 3 tesla superconducting magnet and a Bruker external source vacuum chamber.

The mass spectrometer is controlled by an Aspect 3000 minicomputer with 24 bit word length. The computer is equipped with 192 K of memory, a FT co-processor for fast data treatment, and a fast ADC. The spectrometer operates in both high resolution and broad band FT modes.

Sample Handling

The starting complex, $\text{Cp}_2\text{Zr}(\text{CH}_3)_2$, which was air sensitive, was kept in a dry box until it was ready to be transferred to the ionization chamber. The first step of the sample transfer process was to load a small quantity of the $\text{Cp}_2\text{Zr}(\text{CH}_3)_2$ powder into a melting point capillary, which was then sealed with grease to prevent moisture contamination before it was taken out of the dry box. Prior to loading the sample-containing capillary

on a solids probe tip, the capillary was cut down to the proper length so it would fit securely in the probe tip. The air exposure time of the sample was kept to a minimum to reduce the amount of moisture contamination. After the sample tube was secured on the solids probe tip, the probe was inserted into the first region of the probe loading port, which was then rapidly evacuated by a mechanical pump to about 3.0×10^{-2} torr. Next, the valve separating the solids probe port from the source chamber was opened to allow the probe to be inserted into the source chamber. This allowed the sample to be located right next to the filament assembly of the external EI source. This setup enabled the sample vapor to be easily ionized by the electrons produced using the external EI ionization technique.

The temperature of the solids probe was maintained around 40-60°C to assure that there was sufficient sample vapor in the source region to be ionized so that optimal signals for the ions of interest could be obtained. The ions were produced with a proper electron energy to maximize the signals of the parent ions, $\text{Cp}_2\text{Zr}(\text{OH})^+$, and to minimize the formation of the fragment ion, Cp_2Zr^+ . The typical value of electron energy used throughout this study was 30 eV. H_2O , D_2O , and the organic reagents were introduced into the high vacuum through two Varian precision leak valves, and the amount of vapor leaked into the vacuum was adjusted to provide adequate reactivity of the ions of interest.

Results and Discussion

Preparation of Cp_2ZrOH^+

Equations 4.1 and 4.2 together illustrate the formation of $\text{Cp}_2\text{Zr}(\text{OH})^+$ from the neutral $\text{Cp}_2\text{Zr}(\text{CH}_3)_2$. As equation 4.1 shows, the first step was to produce $\text{Cp}_2\text{Zr}(\text{CH}_3)^+$

in the source region using the external electron impact/ionization technique. Then the $\text{Cp}_2\text{Zr}(\text{CH}_3)^+$ ion was transferred into the analyzer cell from the ionization source through a series of electrostatic lenses. The second step of the ionization process was to introduce H_2O or D_2O into the high vacuum through a Varian precision leak valve, so they could react with the $\text{Cp}_2\text{Zr}(\text{CH}_3)^+$ ions in the cell to produce zirconium hydroxide ions, $\text{Cp}_2\text{Zr}(\text{OH})^+$, as illustrated in equation 4.2. The amount of H_2O vapor leaked into the cell was adjusted to maximize the conversion of $\text{Cp}_2\text{Zr}(\text{CH}_3)^+$ to $\text{Cp}_2\text{Zr}(\text{OH})^+$.



After the $\text{Cp}_2\text{Zr}(\text{OH})^+$ ions were prepared, they were isolated using a combination of chirp and single shot excitation. They then reacted with organic reagents which were introduced into the analyzer cell. The amount of organic reagent leaked into the vacuum was adjusted to provide an optimal yield of the product ions of interest. A variable reaction delay applied to each experiment controlled the amount of the reaction.

All five isotopes of zirconium were observable in the spectra, with m/z 235 and 237 being the most abundant isotopes for $\text{Cp}_2\text{ZrCH}_3^+$ and Cp_2ZrOH^+ , respectively. The Cp_2Zr metallocene moiety is assumed to remain intact for all reactions. The gas-phase reactions of the isolated complex ions, Cp_2ZrOH^+ , with selected alcohols, ethers, esters, amines, and amides will be summarized and discussed in the following sections.

Reactions of Alcohols with Cp_2ZrOH^+

The results of the reactions with alcohols are given in **Table 4-1**. It can be seen from the Table that alkoxide complexes, Cp_2ZrOR^+ , are formed exclusively for all the alcohol compounds after elimination of an H_2O molecule during the reaction, as equation

4.3 illustrates. The product, Cp_2ZrOR^+ , of the reaction was observed immediately following the introduction of the alcohol vapor into the ICR cell. Further experiments have shown that the first product, Cp_2ZrOR^+ , reacted further with excess ROH in the cell to produce the second product complex, $[\text{Cp}_2\text{ZrOR} + \text{ROH}]^+$, at longer reaction delays.

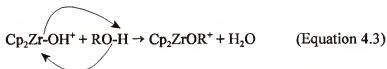


Table 4-1.

Results obtained for the reactions of Cp_2ZrOH^+ with selected alcohols. Only the main product ion of the reaction is listed here.

Name of the compound	Product	m/z	Neutral lost
CH_3OH (methanol)	$\text{Cp}_2\text{ZrOCH}_3^+$	251	H_2O
$\text{CH}_3\text{CH}_2\text{OH}$ (ethanol)	$\text{Cp}_2\text{ZrOCH}_2\text{CH}_3^+$	265	H_2O
$\text{C}_6\text{H}_5\text{OH}$ (phenol)	$\text{Cp}_2\text{ZrOC}_6\text{H}_5^+$	313	H_2O
$(\text{CH}_3)_3\text{COH}$ (t-butanol)	$\text{Cp}_2\text{ZrOC}(\text{CH}_3)_3^+$	293	H_2O
$(\text{CH}_3)_2\text{CHOH}$ (i-propanol)	$\text{Cp}_2\text{ZrOCH}(\text{CH}_3)_2^+$	279	H_2O
$\text{CH}_3(\text{CH}_2)_3\text{OH}$ (butanol)	$\text{Cp}_2\text{ZrO}(\text{CH}_2)_3\text{CH}_3^+$	293	H_2O

Typical spectra obtained for the reactions of Cp_2ZrOH^+ with alcohols are shown in **Figures 4-2 and 4-3**. **Figure 4-2** is a spectrum of the isolated Cp_2ZrOH^+ ions, and **Figure 4-3** shows the formation of the gas-phase product, $\text{Cp}_2\text{ZrOCH}_2\text{CH}_3^+$, with a 2.5 s reaction delay. The set of peaks at m/z 237.1 in **Figure 4-2** represents the parent ion Cp_2ZrOH^+ , and the set of signals at m/z 265.2 are due to the product ion, $\text{Cp}_2\text{ZrOCH}_2\text{CH}_3^+$. Comparison of **Figures 4-2 and 4-3** clearly demonstrates that the Cp_2ZrOH^+ ions were immediately converted to the main gas-phase product $\text{Cp}_2\text{ZrOCH}_2\text{CH}_3^+$. Peaks due to the minor product, $[\text{Cp}_2\text{ZrOC}_2\text{H}_5 + \text{HOC}_2\text{H}_5]^+$, at m/z 311.2 are also seen in the spectrum given in **Figure 4-3**.

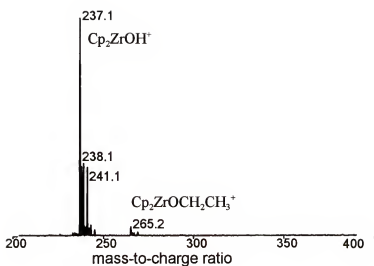


Figure 4-2.

Mass spectrum of isolated Cp_2ZrOH^+ ions with no reaction delay. The spectrum is the accumulation of 16 scans at a pressure of ca. 2×10^{-8} torr.

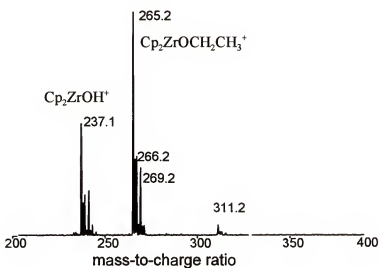


Figure 4-3.

Mass spectrum obtained for the reaction of Cp_2ZrOH^+ with ethanol following a 2.5s reaction delay. The signal at m/z 237.1 is the most abundant isotope of Cp_2ZrOH^+ , and m/z 265.2 is the most abundant isotope of the product $\text{Cp}_2\text{ZrOCH}_2\text{CH}_3^+$. The unlabeled peak at m/z 311.2 is the minor product $[\text{Cp}_2\text{ZrOCH}_2\text{CH}_3 + \text{CH}_3\text{CH}_2\text{OH}]^+$.

Reactions of selected alcohols with $\text{Cp}_2\text{ZrO}^{18}\text{H}^+$. Isotopic labeling studies for selected organic reagents with $\text{Cp}_2\text{ZrO}^{18}\text{H}^+$ were performed to investigate the reaction mechanism, and the results obtained are summarized in **Table 4-2**. The reaction mechanism of the alcohols with the zirconium hydroxide complex can be illustrated using the well accepted four-center/four-electron complex explanation as illustrated in **Figure 4-4**. For example, the reactions of $\text{Cp}_2\text{ZrO}^{18}\text{H}^+$ with ethanol and phenol suggest that the product Cp_2ZrOR^+ was formed by replacing the $-\text{O}^{18}\text{H}$ group of $\text{Cp}_2\text{ZrO}^{18}\text{H}^+$ with the $-\text{OR}$ group of the alcohols after the elimination of a H_2O^{18} molecule during the reaction.

Table 4-2.

Results for the reactions of $\text{Cp}_2\text{ZrO}^{18}\text{H}^+$ with selected reaction reagents

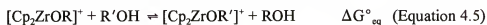
Name of the compound	Product	Neutral lost
$\text{CH}_3\text{CH}_2\text{OH}$ (ethanol)	$\text{Cp}_2\text{ZrOC}_2\text{H}_5^+$	H_2O^{18}
$\text{C}_6\text{H}_5\text{OH}$ (phenol)	$\text{Cp}_2\text{ZrOC}_6\text{H}_5^+$	H_2O^{18}
$(\text{CH}_3)_2\text{CO}_2$ (methyl acetate)	$(\text{Cp}_2\text{ZrO}^{18}\text{H} + \text{C}_3\text{H}_6\text{O}_2)^+$	-----
$\text{CH}_3\text{CO}_2\text{C}_2\text{H}_5$ (ethyl acetate)	$(\text{Cp}_2\text{ZrO}^{18}\text{H} + \text{C}_4\text{H}_8\text{O}_2)^+$	-----
$\text{CH}_3\text{CO}_2\text{H}$ (acetic acid)	$\text{Cp}_2\text{ZrO}_2\text{CCH}_3^+$	H_2O^{18}

Determination of relative Zr-O bond energies ($\Delta\Delta G^\circ_{\text{Zr-O}}$) for selected

Cp_2ZrOR^+ complexes. **Table 4-3** summarizes the free energy of the reactions ($\Delta G^\circ_{\text{eq}}$)

and the relative Zr-O bond energies ($\Delta\Delta G^\circ_{\text{Zr-O}}$) of selected Cp_2ZrOR^+ complexes.

Although the absolute Zr-O bond energies of Cp_2ZrOR^+ complexes cannot be determined from this study, the relative Zr-O bond energies of Cp_2ZrOR^+ complexes can be estimated as illustrated below. The kinetic reactions can be described using equation 4.5,



where R and R' are H, methyl, ethyl, i-propyl, s-butyl, or t-butyl. Equation 4.5 can be broken down into three separate equations:

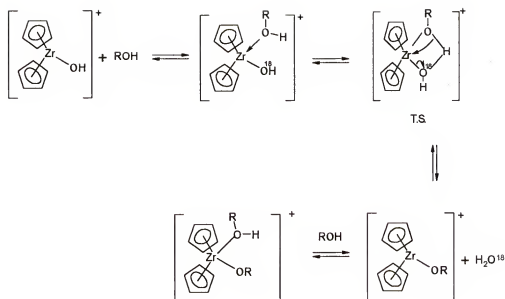


Figure 4-4.

Reaction scheme of an alcohol compound with $\text{Cp}_2\text{ZrO}^{18}\text{H}^+$. T.S. is the reaction transition state.

Table 4-3.

Free energies ($\Delta G^\circ_{\text{eq}}$) determined for selected reactions described in equation 4.5, and the relative bond strength of Zr-O ($\Delta\Delta G^\circ_{\text{Zr-O}}$) determined for each reaction pair.

Reaction pair	$\Delta G^\circ_{\text{eq}}(\text{kcal/mol})$	$\Delta\Delta G^\circ_{\text{Zr-O}} \pm 0.7(\text{kcal/mol})$
$\text{Cp}_2\text{ZrOH}^+/\text{CH}_3\text{OH}$	2.6~3.2	12.22
$\text{Cp}_2\text{ZrOCH}_3^+/\text{C}_2\text{H}_5\text{OH}$	0.7~0.8	0.49
$\text{Cp}_2\text{ZrOCH}_3^+/\text{i-propanol}$	1.2~1.6	1.88
$\text{Cp}_2\text{ZrOCH}_3^+/\text{t-butanol}$	1.5~1.6	2.17
$\text{Cp}_2\text{ZrOC}_2\text{H}_5^+/\text{i-propanol}$	0.7~0.8	1.35
$\text{Cp}_2\text{ZrOC}_2\text{H}_5^+/\text{s-butanol}$	1.3~1.4	2.64
$\text{Cp}_2\text{ZrOC}_2\text{H}_5^+/\text{t-butanol}$	1.0~1.1	1.93



From the analog of Hess's law, the addition of equations 4.6, 4.7, and 4.8 gives back equation 4.5, so the values of $\Delta G^\circ_{\text{eq}}$ can be expressed as:

$$\Delta G^\circ_{\text{eq}} = \Delta G^\circ_{\text{Zr-OR}} - \Delta G^\circ_{\text{Zr-OR}'} + \Delta G^\circ_{\text{rxn}} \quad (\text{Equation 4.9})$$

Let $\Delta G^\circ_{\text{Zr-OR}} - \Delta G^\circ_{\text{Zr-OR}'} = \Delta\Delta G^\circ_{\text{Zr-O}}$, and rearrange equation 4.9 to obtain the expression given in equation 4.10, which can be used to calculate the relative Zr-O bond energy:

$$\Delta\Delta G^\circ_{\text{Zr-O}} = \Delta G^\circ_{\text{eq}} - \Delta G^\circ_{\text{rxn}} \quad (\text{Equation 4.10})$$

In equation 4.10, $\Delta G^\circ_{\text{rxn}}$ is approximately equal to $\Delta H^\circ_{\text{rxn}}$ by assuming that under the current experimental conditions the contribution of $T\Delta S^\circ_{\text{rxn}}$ is insignificant compared to the values of $\Delta H^\circ_{\text{rxn}}$. The $T\Delta S^\circ_{\text{rxn}}$ term is ignored for all calculations in this chapter. $\Delta H^\circ_{\text{rxn}}$ can be determined using Hess's law with the standard enthalpy information given in the CRC handbook,¹¹⁴ and $\Delta G^\circ_{\text{eq}}$ is determined using equation 4.11,

$$\Delta G^\circ_{\text{eq}} = -RT \ln K_{\text{eq}} \quad (\text{Equation 4.11})$$

where R in equation 4.11 is the gas constant, and T is the temperature of the ions in the ion trap. For external ionization sources, ions are initially formed outside of the cell and have to be transferred into the cell through a series of electrostatic lenses. Ions in the cell are assumed to be at room temperature, 298.15 K, and this value was used for all $\Delta G^\circ_{\text{eq}}$ calculations in this chapter. The reaction equilibrium constant, K_{eq} , can be determined using the expression given in equation 4.12,

$$K_{\text{eq}} = \frac{I_{[\text{Cp}_2\text{ZrOR}]^+} P_{\text{ROH}} \alpha_{\text{ROH}}}{I_{[\text{Cp}_2\text{ZrOR}]^+} P_{\text{R}'\text{OH}} \alpha_{\text{R}'\text{OH}}} \quad (\text{Equation 4.12})$$

where I is the normalized intensity of the ion, p is the pressure of the neutral gas in torr, and α is the pressure correction factor to correct the sensitivity difference that the ion gauges might have toward different neutrals in the cell.¹¹⁵

Typical equilibrium data obtained for the alkoxide reactions described in equation 4.5 are illustrated using the kinetic reaction of $\text{Cp}_2\text{ZrOC}_4\text{H}_9^+$ with ethanol given in **Figure 4-5**. **Figure 4-5** is a kinetic plot of the natural logarithm of the normalized ion intensity, $\ln(I)$, versus the reaction delay in seconds. It can be seen from **Figure 4-5** that as the starting ion $\text{Cp}_2\text{ZrOC}_4\text{H}_9^+$ disappears with the reaction delay, the product ion $\text{Cp}_2\text{ZrOC}_2\text{H}_5^+$ increases in concentration. After a 3 second reaction delay is applied, both products $\text{Cp}_2\text{ZrOC}_4\text{H}_9^+$ and $\text{Cp}_2\text{ZrOC}_2\text{H}_5^+$ lose their ion intensities due to the formation of three new adduct products, $[\text{Cp}_2\text{ZrOC}_2\text{H}_5 + \text{C}_4\text{H}_9\text{OH}]^+$, $[\text{Cp}_2\text{ZrOC}_2\text{H}_5 + \text{C}_4\text{H}_9\text{OH}]^+$, and $[\text{Cp}_2\text{ZrOC}_4\text{H}_9 + \text{C}_4\text{H}_9\text{OH}]^+$. As the kinetic plot in **Figure 4-5** shows, a reaction equilibrium between the $\text{Cp}_2\text{ZrOC}_4\text{H}_9^+$ complex and the $\text{Cp}_2\text{ZrOC}_2\text{H}_5^+$ complex was established after 5 seconds of reaction delay. This reaction equilibrium was used to determine the K_{eq} value of the reaction.

The formation of three adduct products for the reaction of t-butoxide complex with ethanol is consistent with the other alcohols studied earlier. At longer reaction delays, some of the product ions, Cp_2ZrOR^+ , were converted to similar adduct products observed for the reactions of the t-butoxide complex and ethanol. These adduct complexes have one common feature - four electron donating ligands around the zirconium metal center. This suggests that the most stable structure of the zirconium complexes seen in this study consists of four electron donating ligands including two Cp complexes, one -OR, and one ROH. The zirconium complexes with four electron

donating substituents are also seen for other classes of organic compounds such as ethers, amines, and amides (these results are discussed later).

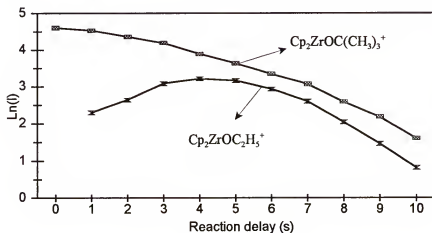


Figure 4-5.

Plot of $\ln(I)$ vs. reaction delay for the reaction: $[\text{Cp}_2\text{ZrOC}_4\text{H}_9]^+ + \text{C}_2\text{H}_5\text{OH} \rightleftharpoons [\text{Cp}_2\text{ZrOC}_2\text{H}_5]^+ + \text{C}_4\text{H}_9\text{OH}$. The reactant ions and the product ions are labeled on the plot.

The relative Zr-O bond energies of the Cp_2ZrOR^+ complexes are represented as an energy ladder given in **Figure 4-6**. The vertical axis of the diagram is $\Delta\Delta G^\circ_{\text{Zr-O}}$ in kcal/mol, and the right column of the diagram represents the -R substituent of the Cp_2ZrOR^+ complex. All reactions were studied with either the methoxide complex or the ethoxide complex. It can be seen from **Figure 4-6** that the $\Delta\Delta G^\circ_{\text{Zr-O}}$ value obtained for the reaction of Cp_2ZrOH^+ and $\text{Cp}_2\text{ZrOCH}_3^+$ is 10 times larger than the rest of the $\Delta\Delta G^\circ_{\text{Zr-O}}$ values. In fact, the $\Delta\Delta G^\circ_{\text{Zr-O}}$ values between the alkoxide complexes are relatively small, with a typical value less than 4 kcal/mol, as shown in **Figure 4-7**.

During the earlier derivation of $\Delta G^\circ_{\text{eq}}$ in this chapter, $\Delta G^\circ_{\text{Zr-OR}} - \Delta G^\circ_{\text{Zr-OR}'}$ was defined as $\Delta\Delta G^\circ_{\text{Zr-O}}$. This definition relates $\Delta\Delta G^\circ_{\text{Zr-O}}$ of the reactions to the relative Zr-

O bond energies of the Cp_2ZrOR^+ complexes. A small $\Delta\Delta G^\circ_{\text{Zr-O}}$ value means that the Zr-O bond strength is similar between the two alkoxide complexes while a large $\Delta\Delta G^\circ_{\text{Zr-O}}$ value suggests a large difference in the Zr-O bond strength of the complexes. Hence, the small $\Delta\Delta G^\circ_{\text{Zr-O}}$ values obtained for the alkoxide complexes as shown in **Figure 4-6** suggest that the Zr-O bond strength between the alkoxide complexes is similar. **Figures 4-6 and 4-7** show that the $\Delta\Delta G^\circ_{\text{Zr-O}}$ value increases as the -R group gets larger. This trend implies that an alkoxide complex with a larger -R group can form a stronger Zr-O bond than a complex with a smaller -R substituent. The formation of the stronger Zr-O bond for the complex with larger -R substituent is due to the polarizability property of the -R group. The larger the -R group, the easier it can be polarized, and the better an electron donating group it becomes. Therefore, a stronger Zr-O bond can be formed for alkoxide complexes with larger -R substituents. Since Zr is an electron-insufficient metal center in the complexes, it binds more strongly with a larger R group, such as a butyl group, compared to a smaller methyl group. From the experimental results, the order of the Zr-O bond strength for the alkoxide complexes can be obtained as follows: $\text{Cp}_2\text{ZrOH}^+ < \text{Cp}_2\text{ZrOCH}_3^+ < \text{Cp}_2\text{ZrOC}_2\text{H}_5^+ < \text{Cp}_2\text{ZrOCH}(\text{CH}_3)_2^+ < \text{Cp}_2\text{ZrOCHCH}_2(\text{CH}_3)_2^+ < \text{Cp}_2\text{ZrOC}(\text{CH}_3)_3^+$.

The $\Delta\Delta G^\circ_{\text{Zr-O}}$ value determined for the t-butoxide complex from the reaction of the methoxide complex is 0.25 kcal/mol lower than the $\Delta\Delta G^\circ_{\text{Zr-O}}$ value obtained from the reaction of ethoxide. The $\Delta\Delta G^\circ_{\text{Zr-O}}$ value between the methoxide complex and the isopropoxide complex is 0.04 kcal/mol lower than the $\Delta\Delta G^\circ_{\text{Zr-O}}$ value estimated from the reaction of ethoxide complex and the isopropanol compound. These differences are probably due to experimental errors.

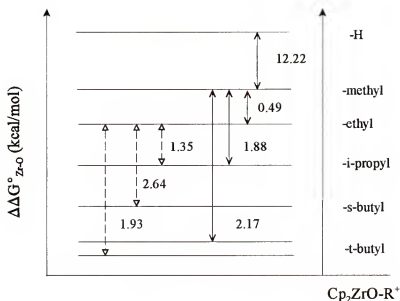


Figure 4-6.

The relative Zr-O bond strength ($\Delta\Delta G^\circ_{\text{Zr-O}}$) in ± 0.7 kcal/mol for selected Cp_2ZrOR^+ complexes where R = H, methyl, ethyl, i-propyl, s-butyl, and t-butyl. The diagram is not drawn to scale.

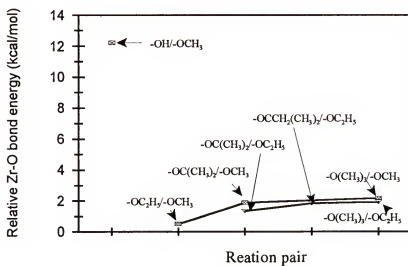
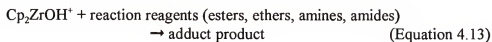


Figure 4-7.

The plot of the $\Delta\Delta G^\circ_{\text{Zr-O}}$ values (± 0.7 kcal/mol) determined from the reaction pairs studied.

Reactions of Cp_2ZrOH^+ with Other Organic Families: Esters, Ethers, Amines, and Amides

Reactions of Cp_2ZrOH^+ with four other classes of organic compounds were investigated using the same method as for the alcohol studies. The results obtained for the reactions of these four classes of organic compounds are summarized in **Table 4-4**. As the Table shows, except for acetic acid, the adduct products, $[\text{Cp}_2\text{ZrOH} + \text{RCO}_2\text{R}', \text{ROR}', \text{RNHR}', \text{or RCONHR}']^+$, were exclusively produced for the reactions of Cp_2ZrOH^+ with esters, ethers, amines, or amides, respectively. The general reaction can be illustrated by equation 4.13.



Isotopic studies of the reactions of $\text{Cp}_2\text{ZrO}^{18}\text{H}^+$ with acetic acid, methyl acetate, and ethyl acetate were carried out under the same experimental conditions as used for the unlabeled studies. The results obtained are given in **Table 4-2**. The isotopic labeling studies generated similar results to the unlabeled studies. For methyl acetate and ethyl acetate, the adducts were still observed as the main gas phase products, and the reaction mechanism is given in equation 4.14.



The reaction of the isotopic labeling study for acetic acid is illustrated in equation 4.15. The experimental results showed that $\text{Cp}_2\text{ZrO}_2\text{CCH}_3^+$ was the primary gas phase product. The isotopic studies confirmed that $\text{Cp}_2\text{ZrO}_2\text{CCH}_3^+$ was formed by replacing the $-\text{O}^{18}\text{H}$ substituent of $\text{Cp}_2\text{ZrO}^{18}\text{H}^+$ with the $-\text{O}_2\text{C}_2\text{H}_3$ part of the acetic acid and the

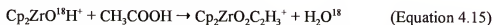
Table 4-4.

Data collected for the reactions of Cp_2ZrOH^+ with various esters, ethers, amines, and amides.

Name of the compound	Product	m/z
* $\text{CH}_3\text{CO}_2\text{H}$ (acetic acid)	$((\text{Cp}_2\text{ZrO}_2\text{CCH}_3)$	279
$\text{CH}_3\text{CO}_2\text{CH}_3$ (methyl acetate)	$(\text{Cp}_2\text{ZrOH} + \text{CH}_3\text{CO}_2\text{CH}_3)^+$	311
$\text{CH}_3\text{CO}_2\text{CH}_2\text{CH}_3$ (ethyl ester)	$(\text{Cp}_2\text{ZrOH} + \text{CH}_3\text{CO}_2\text{CH}_2\text{CH}_3)^+$	325
$\text{CH}_3(\text{CH}_2)_2\text{CO}_2\text{CH}_3$ (methyl butyrate)	$(\text{Cp}_2\text{ZrOH} + \text{CH}_3(\text{CH}_2)_2\text{CO}_2\text{CH}_3)^+$	339
$\text{C}_6\text{H}_5\text{CO}_2\text{CH}_2\text{CH}_3$ (ethyl benzoate)	$(\text{Cp}_2\text{ZrOH} + \text{C}_6\text{H}_5\text{CO}_2\text{CH}_2\text{CH}_3)^+$	387
$\text{Cl}(\text{F})_2\text{C}_2\text{O}_2\text{CH}_3$	$(\text{Cp}_2\text{ZrOH} + \text{Cl}(\text{F})_2\text{C}_2\text{O}_2\text{CH}_3)^+$	381
$(\text{F})_3\text{C}_2\text{O}_2\text{CH}_2\text{CH}_3$ (ethyl trifluoroacetate)	$(\text{Cp}_2\text{ZrOH} + (\text{F})_3\text{C}_2\text{O}_2\text{CH}_2\text{CH}_3)^+$	379
$\text{C}_8\text{H}_7\text{O}_4\text{N}$ (4-nitrophenyl acetate)	$(\text{Cp}_2\text{ZrOH} + \text{C}_8\text{H}_7\text{O}_4\text{N})^+$	418
$(\text{CH}_3\text{CH}_2)_2\text{O}$ (diethylether)	$(\text{Cp}_2\text{ZrOH} + (\text{CH}_3\text{CH}_2)_2\text{O})^+$	311
$((\text{CH}_3)_2\text{CH})_2\text{O}$ (diisopropylether)	$(\text{Cp}_2\text{ZrOH} + ((\text{CH}_3)_2\text{CH})_2\text{O})^+$	339
$(\text{CH}_3\text{CH}_2\text{CH}_2)_2\text{NH}$ (dipropylamine)	$(\text{Cp}_2\text{ZrOH} + (\text{CH}_3\text{CH}_2\text{CH}_2)_2\text{NH})^+$	338
$(\text{CH}_3\text{CH}_2)_3\text{NH}$ (triethylamine)	$(\text{Cp}_2\text{ZrOH} + (\text{CH}_3\text{CH}_2)_3\text{NH})^+$	338
$\text{HCON}(\text{CH}_3)_2$ (N,N-dimethyl formamide)	$(\text{Cp}_2\text{ZrOH} + \text{HCON}(\text{CH}_3)_2)^+$	310
$\text{CH}_3\text{CON}(\text{CH}_3)_2$ (N,N-dimethylacetamide)	$(\text{Cp}_2\text{ZrOH} + \text{CH}_3\text{CON}(\text{CH}_3)_2)^+$	324

* indicate different product is observed.

elimination of one H_2O^{18} molecule during the reaction. The reaction mechanism of the acetic acid reaction is similar to the one proposed earlier for the alcohols, but it is different from the rest of esters studied in this chapter.



One possible explanation for the discrepancy in results occurring within the ester family (with general formula $\text{RCO}_2\text{R}'$) relates to the $-\text{R}'$ group of the compound. When comparing the formula of acetic acid ($\text{CH}_3\text{CO}_2\text{H}$) to methyl acetate ($\text{CH}_3\text{CO}_2\text{CH}_3$) and ethyl acetate ($\text{C}_2\text{H}_5\text{CO}_2\text{C}_2\text{H}_5$), it can be seen that the H atom is the $-\text{R}'$ group for acetic acid which is same as the $-\text{R}'$ of the alcohols (ROH), but the $-\text{R}'$ groups of methyl acetate and ethyl acetate are $-\text{CH}_3$ and $-\text{C}_2\text{H}_5$, respectively. Since the ion/molecule reactions of Cp_2ZrOH^+ with alcohols and acetic acid were observed in this study, and the similar reactions were not observed for other esters, these results suggest that the H atom as $-\text{R}'$

of the organic compound plays an important role for the formation of the final products. When the -R' is an alkyl group other than the H atom, only adduct products are formed for the reactions of the Cp_2ZrOH^+ complex. When the -R' of the organic compound is a H atom, an ion/molecule reaction occurs.

In the reactions for the rest of the ethers, esters, amines and amides, only adduct products were observed. The results obtained are summarized in **Table 4-4**. These reactions will be examined thermodynamically and kinetically to investigate the factors that prevent the formation of the expected gas-phase products which are seen for acetic acid and the alcohols.

The studies of the alcohol family have shown that the Zr-O bond of a $\text{Cp}_2\text{Zr-OR}^+$ complex is relatively stronger than the Zr-O bond of the $\text{Cp}_2\text{Zr-OH}^+$ complex. If $\text{Zr-O}_2\text{R}^+$ was formed as the final product for the reaction of an ester compound, its Zr-O bond strength would be stronger than one single Zr-O bond and weaker than two single Zr-O bonds. Therefore, the formation of $\text{Zr-O}_2\text{R}^+$ for esters would be more favorable than the formation of Zr-OR^+ for alcohols, and this can be demonstrated numerically. With the values $\Delta\Delta G^\circ_{\text{Zr-O}}$ shown in **Figure 4-7** and the derivation steps illustrated in equations 4.6 to 4.10, the $\Delta\Delta G^\circ_{\text{Zr-O}}$ values for the reactions of Cp_2ZrOH^+ with methyl acetate and ethyl acetate are estimated to be greater than -12.22 kcal/mol. With the values of the standard enthalpy of formation found in CRC handbook, $\Delta G^\circ_{\text{rxn}}$ for the methyl acetate and ethyl acetate reactions is determined as -19.36 and -5.9 kcal/mol, respectively. After $\Delta\Delta G^\circ_{\text{Zr-O}}$ and ΔG° are determined, $\Delta G^\circ_{\text{eq}}$ of the reactions for methyl acetate and ethyl acetate can be estimated using equation 4.9. The derivations show that $\Delta G^\circ_{\text{eq}}$ is ≤ -31.58 kcal/mol for the methyl acetate reaction and ≤ -25.26 kcal/mol for ethyl acetate. The negative $\Delta G^\circ_{\text{eq}}$

values indicate that both reactions of Cp_2ZrOH^+ with methyl and ethyl acetates are thermodynamically favorable for producing the products $\text{Cp}_2\text{ZrO}_2\text{CCH}_3^+$ and $\text{Cp}_2\text{ZrO}_2\text{CC}_2\text{H}_5^+$, respectively. However, there is no evidence that such products were experimentally observed.

The other probable explanation for why the expected products $\text{Cp}_2\text{ZrO}_2\text{CCH}_3^+$ and $\text{Cp}_2\text{ZrO}_2\text{CC}_2\text{H}_5^+$ were not observed for methyl and ethyl acetates may be due to kinetics. For example, the adduct products are probably the reaction intermediate, and the activation energy barriers for the proposed four-center/four-electron transition states (see **Figure 4-8**) are too high to be overcome under the experimental conditions; therefore, the favorable transition structures which could lead to the expected gas-phase product are prohibited.

Figure 4-9 illustrates two possible activation energy barriers that could prevent the conversion of the adducts to the final expected gas-phase products. One possible activation energy structure is that the transition energy is simply too high for the intermediate structure to get over the energy barrier (See **Figure 4-9. a**) and lead to the expected gas phase products. The second possibility is that there is an energy minimum at the transition state as shown in **Figure 4-9. b**. In this case, the transition states (see **Figure 4-8**) do not have enough energy to roll themselves out of this energy valley and to convert the transition state structures to the expected final products.

The same argument holds for the reactions of ethers, amines, and amides. Even though the reactions are thermodynamically favorable for complete reactions, the kinetic data are not favorable for complete reactions to form the expected final products. Therefore, the expected gas-phase products $\text{Cp}_2\text{ZrO}_2\text{CR}^+$, Cp_2ZrOR^+ , $\text{Cp}_2\text{ZrNHR}^+$, and

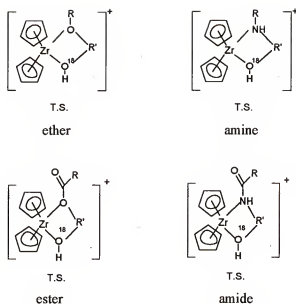


Figure 4-8.

Proposed transition states (T.S.) for the reactions of Cp_2ZrOH^+ with ester, ether, amine or amide reagents.

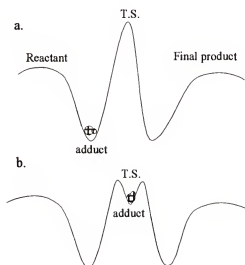


Figure 4-9.

The possible structures of the transition state which could inhibit the formation of the expected final products, $\text{Cp}_2\text{ZrO}_2\text{CR}^+$, Cp_2ZrOR^+ , $\text{Cp}_2\text{ZrNHR}^+$, and $\text{Cp}_2\text{ZrOCNHR}^+$ for the reactions of Cp_2ZrOH^+ with esters, ethers, amines, and amides.

$\text{Cp}_2\text{ZrOCNHR}^+$ for the reactions of esters (except acetic acid), ethers, amines, and amides never have the opportunity to be formed.

Comments on the Results Obtained from Both External and Internal EI Methods

The results obtained with the external EI method have shown fewer reaction channels than the results obtained from the internal EI method. For example, the external EI approach eliminated reaction channels involving $\text{Cp}_2\text{Zr}(\text{CH}_3)_2$ neutral which were observed using the internal EI approach. Since the external EI technique generates ions in the ionization source, which is located some distance from the analyzer cell, and since only ions can be transferred into the analyzer cell through a series of electrostatic lenses, the unionized neutrals in the source region are pumped away before they can enter the ICR cell. However, for the internal EI technique, the filament assembly was located adjacent to the ICR cell, and therefore any unionized $\text{Cp}_2\text{Zr}(\text{CH}_3)_2$ complex could easily enter the reaction cell to complicate the desirable reaction pathways. Comparisons of the results obtained from both the external and internal EI techniques demonstrate that the external EI approach provides a cleaner environment for the gas phase ion/molecule reactions than the internal EI approach.

Conclusions

This study has shown that under the current experimental conditions a Cp_2ZrOR^+ complex was produced when the zirconium-hydroxide complex (Cp_2ZrOH^+) reacted with selected alcohols (ROH). The results obtained from the isotopic studies have confirmed that the Cp_2ZrOR^+ product was formed by cleaving the metal oxygen bond of Cp_2ZrOH^+ . The -OH substituent of Cp_2ZrOH^+ was replaced with the -OR group of the alcohol.

However, only adduct products were produced for the reactions of Cp_2ZrOR^+ with other classes of organic compounds such as esters, ethers, amines, and amides. Unfavorably high energy barriers may be responsible for the lack of the expected final gas-phase products. Although the O^{18} labeling studies show that adduct products were observed for the methyl acetate and ethyl acetate reactions, $\text{Cp}_2\text{ZrO}_2\text{CCH}_3^+$ was seen as the primary product for acetic acid after a H_2O^{18} molecule was eliminated from the reaction complex.

In this study, the free energies ($\Delta G^\circ_{\text{eq}}$) for the reactions of several Cp_2ZrOR^+ complexes were determined and then were employed to estimate the relative Zr-O bond energies ($\Delta\Delta G^\circ_{\text{Zr-O}}$) of the Cp_2ZrOR^+ complexes. The $\Delta\Delta G^\circ_{\text{Zr-O}}$ values determined suggest that as the -R group of the Cp_2ZrOR^+ complex gets larger, the Zr-O bond becomes stronger. The results also show that the Cp_2ZrOH^+ complex has the weakest Zr-O bond among all Cp_2ZrOR^+ complexes studied. This work has demonstrated that the zirconium-hydroxide complex can affect hydrolysis of alcohols in the gas phase, but the hydrolysis reactions were not observed for ethers, esters, amines, and amides.

CHAPTER 5

INFRARED MULTIPHOTON DISSOCIATION (IRMPD) STUDIES OF SMALL PEPTIDES IN THE GAS PHASE WITH ESI-FTICR/MS

Introduction

Peptide sequencing with mass spectrometry (MS) has gained much attention in recent years since proper ionization techniques to introduce charged peptides into the gas phase have been available. A major effort of mass spectrometric peptide studies has focused on understanding the dissociation patterns of peptides.^{116,117} A better understanding of peptide dissociation patterns will obviously lead to better characterization of larger biological systems, so successful peptide sequencing using MS can provide some insights into the gas phase protein sequencing. For example, when peptide ions of differing amino acid sequences have identical mass, they can not be easily differentiated. One means of achieving this is to perform MSⁿ experiments to sequence their primary structures. If a general correlation exists between peptide fragmentation patterns and the location of a specific amino acid residue within a peptide sequence, it would simplify the mass spectral analysis and speed up the sequencing process.

A majority of the mass spectrometric research involving peptide sequencing has been done using either the collisionally activated dissociation (CAD) method or (in FTICR studies) the sustained-off-resonance collisionally activated dissociation (SORI-CAD) method. Although both of these can provide information useful in elucidating the

structure of a peptide, each has disadvantages associated with it. CAD is a high-energy dissociation method which usually gives too much fragmentation, leading to very complex spectra which can be a challenge for correct interpretation. For both CAD and SORI-CAD methods, peptide fragmentation is caused by collision with an externally introduced neutral gas such as argon. Introduction of neutral gases into the high vacuum region increases the analyzer cell pressure and reduces the optimal low pressure environment for obtaining high resolution spectra.

Previous experiments have shown that infrared multiphoton dissociation (IRMPD) is a low-energy dissociation technique that works well for structure elucidation of small and large molecules.^{80,118,119} Although SORI-CAD is also well accepted as a low-energy dissociation technique yielding fragmentation pathways of low activation energy, IRMPD combined with FT/MS has a number of advantages over SORI-CAD, summarized by Wilkins and co-workers.¹²⁰ First, the photodissociation (PD) method does not require introducing collision gas into the trap, thus the ideal low pressure conditions can be maintained for optimal instrumentation performance. Second, product ions are formed “on-axis” (along the z-axis, close to the center of the xy-plane) without any significant magnetron motion. Third, since the activation of precursor ions does not depend upon imparting translational energy, the application of IRMPD is not restricted to a certain mass range by instrumental dimensions, which limit the mass range for collision activation. Fourth, because the excitation of precursor ions is a stepwise process, energy deposition increases with irradiation time. With PD, higher energy levels for dissociation of larger biological systems with more degrees of freedom can easily be accomplished by increasing the irradiation time. One disadvantage of the IRMPD method is that it requires systems to

contain a chromophore which absorbs 10.6 μm CO_2 laser wavelength. For large biological molecules, this requirement can be easily met because they contain hundreds of amino acid residues which can absorb the specific wavelength, but small peptides with only a few residues have to be chosen carefully to meet that requirement. However, the mass spectra generated from large molecules are usually very complex to interpret, so small peptides consisting of six amino acid residues or fewer were chosen in the present study. Since previous studies indicated that arginine-containing peptides absorb the 10.6 μm fundamental wavelength of CO_2 lasers, such peptides were chosen to be the target of this study. Another reason for choosing arginine-containing peptides is that they were previously studied with other methods and the results were available for comparison.^{117,121,122}

In this chapter, the fragmentation patterns of small arginine-containing peptides (six or fewer amino acids) studied with the IRMPD method are reported. General correlations between the dissociation patterns of small peptides and the locations of arginine residues in the peptides were investigated; the dissociation spectra observed for singly and doubly charged states of the same peptide were analyzed and compared. Dissociation of the same peptides was also studied using the SORI-CAD method, and comparison of the SORI-CAD results with the IRMPD results is summarized.

Experimental

Materials and Sample Preparation

All peptide samples used in this project were purchased from Sigma Chemical Co. (St. Louis, MO) and used without further purification. All the ESI samples were prepared

with concentrations of ca. 1×10^{-6} M or less in 49/49/2 (v/v/v) methanol/water/acetic acid except for the TPRK and TKPR samples, where 50/50 (v/v) methanol/water was the solvent.

Instrumentation

The shielded 9.4 T FTICR/MS - IRMPD experiments. All IRMPD experiments were performed at the National High Magnetic Field Laboratory in Tallahassee, Florida with a shielded 9.4 T FTICR mass spectrometer equipped with a Finnigan Odyssey data system as shown in **Figure 5-1**.¹²³ The system consists of a 9.4 T superconducting horizontal bore solenoidal magnet (Oxford Instruments) with a 225 mm room temperature bore, a cylindrical homogenous region of about 10 cm diameter by 10 cm axial length, and a 90 mm thick iron shield which reduces the stray field to less than 5 gauss at a distance of 30 cm from the face of the shield. The vacuum of the instrument is divided into four sections. The first section is the electrospray source, which is a home-built Chait-type source.¹²⁴ This section contains a 20 cm long 0.6 mm i.d. resistively-heated stainless steel capillary (Alltech, Deerfield, IL). This stage is evacuated by a 30 cf/m rotary pump (Varian, Lexington, MA) to 1 torr. The second section contains a 0.8 mm diameter skimmer (Beam Dynamics, Minneapolis, MN) and a 60 cm long RF-only octopole ion guide, and this section is pumped to a pressure of 1 mtorr by a 1500 L/s hybrid turbo-drag pump (Balzers, Hudson, NH). The third section of the vacuum system contains a second octopole, 2 m in length, and is differentially pumped by a 1500 L/s cryopump (CTI Cryogenics, Waltham, MA). Both octopoles are constructed with 1.6 mm titanium rods with a 4.8 mm i.d., and they are driven at 1.3 MHz by high power RF supplies. The last section is the analyzer region, with a base pressure of 1×10^{-8} torr,

which contains a 5 cm diameter cylindrical open-ended Penning trap constructed with copper plates and Macor insulators.¹²⁵

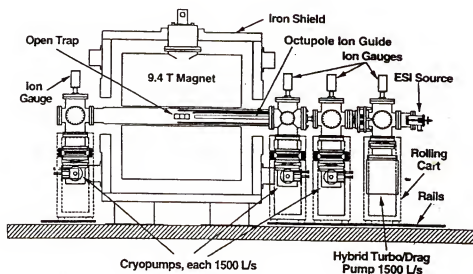


Figure 5-1.

The 9.4 Tesla mass spectrometer at NHMFL used for IRMPD experiments.

All ESI samples were sprayed at a rate of 0.3 $\mu\text{L}/\text{min}$. After the ions were produced with ESI and then transferred to the ion trap using the second octupole, the ions of interest were isolated with a combination of a chirp pulse and SWIFT. Then a model E48-2-115 Synrad CO_2 laser located on the opposite side of the magnet from the ESI source was fired for 0.3 or 0.4 sec with output power between 20 to 40 W. The laser firing time and the laser power used in all IRMPD experiments were adjusted to produce a reasonable amount of dissociation.

The shielded 4.7 T FTICR/MS for SORI-CAD experiments. All CAD and Sori-CAD data were collected using a shielded 4.7 T FTICR mass spectrometer (Bruker Analytical Systems, Inc., Billerica, MA, USA) at the University of Florida. A schematic

diagram of the instrument is shown in **Figure 5-2**. The system consists of a shielded horizontal 4.7 T superconducting solenoidal magnet (Magnex Scientific Ltd., Abingdon, England) with a 150 mm room temperature bore and a 170 mm³ cylindrical RF-shimmed InfinityTM analyzer cell.⁷⁰

The vacuum system of the instrument is divided into three sections. The first section is an external electrospray source,⁷² which utilizes a hexapole ion guide (Analytica of Branford, Branford, CT, USA). The ESI source was modified in our laboratory with a heated metal capillary for desolvation purposes, which is similar in design to that reported by Ikononov and Kebarle.¹²⁶ This stage is evacuated by a 500 L/min mechanical pump and a turbo-drag pump with a mechanical forepump to ca. 2×10^{-3} torr. A 800 L/s cryopump (liquid He) is used to pump the region between the hexapole and the first conductance limit to give a source pressure of about 2×10^{-6} torr. The second section contains all the electrostatic ion transfer optics and is pumped by a 400 L/s cryopump (liquid He). The third section of the vacuum is the ultrahigh vacuum region which contains the analyzer cell, and it is pumped by a 400 L/s cryopump (liquid He) to maintain a base pressure in the low 10^{-9} torr range. The stainless steel capillary (500 μm i.d. \times 170 mm length) was held at ground potential and was maintained at a temperature of 120 °C. After leaving the ESI source, ions were accelerated by a 3 kV potential difference and focused through the conductance limits before being decelerated and trapped in the ion trap.

The same ESI samples used for IRMPD investigations were used for SORI-CAD experiments. They were sprayed with a flow rate of 1 $\mu\text{L}/\text{min}$. The mass spectra of the molecular ions were collected with a cell pressure of 1×10^{-9} torr, and the SORI-CAD experiments were performed with Ar as the collision gas at a pressure of 1×10^{-7} torr.

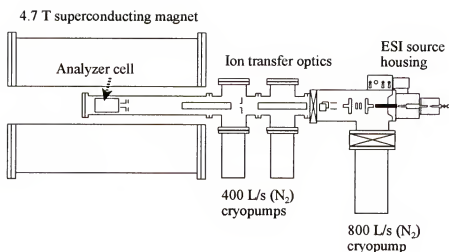


Figure 5-2.

4.7 Tesla mass spectrometer used for all SORI-CAD experiments at UF.

Results and Discussion

Nomenclature of Peptide Fragmentation in the Gas Phase

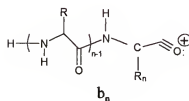
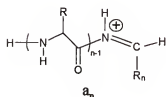
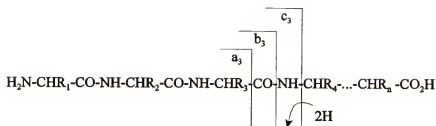
With the capability of mass spectrometry for sequencing peptides and proteins, it became necessary to develop a systematic naming system for peptide fragments produced in gas phase. The first comprehensive nomenclature was developed by Roepstorff¹²⁷ at Odense University in Denmark, and it was derived from existing naming systems used by several groups.^{128,129} Since Roepstorff proposed his nomenclature in 1984, it has been refined and extended by several groups^{130,131} to account for all possible peptide fragments seen in the gas phase. In the following section, the nomenclature used for the present work will be briefly summarized.

Amino acids are the building blocks of peptides and proteins, and they are based on linear arrangements of repeating units, -NH-CHR-CO- , which differ only in the nature of the side chain, R. When peptides or proteins undergo collisional dissociation in the gas

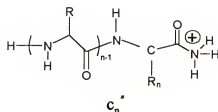
phase, at least three types of fragmentation paths are observed: N-terminal peptide fragmentation, C-terminal peptide fragmentation, and nonsequential fragmentation. The different fragmentation types are denoted a_n , b_n , c_n , and d_n when the positive charge is retained on the N-terminal peptide fragment and v_n , w_n , y_n '' , and z_n when the positive charge is retained by the C-terminal peptide fragment. When the positive charge is located on a mid-sequence fragment, the fragment is referred as nonsequential fragmentations.

1. N-terminus charge retention:

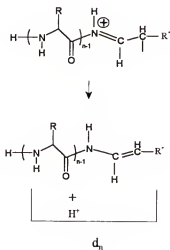
- a. The a_n , b_n , and c_n ions are formed by main-chain fragmentation:



- b. The c_n '' ions are formed by attaching two H atoms to the corresponding c_n ions.

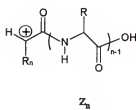
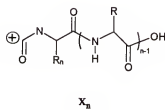
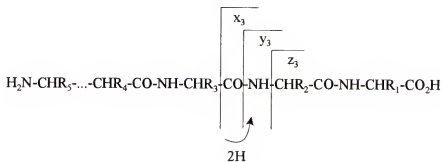


- c. The d_n ions are formed by homolytic cleavage of the bond between the β and γ carbons of the side chain of a_{n+1} ions.

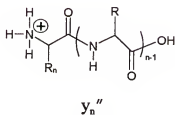


2. C-terminus charge retention:

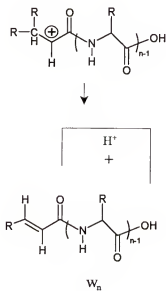
- a. The x_n , y_n , and z_n ions are formed by peptide backbone fragmentation:



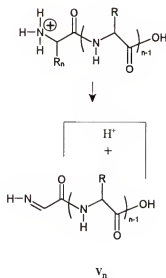
- b. The y_n'' ions are formed from adding two H atoms to the corresponding y_n ions.



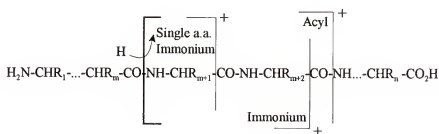
- c. The w_n ions are produced by homolytic cleavage of the bond between the β and γ carbons of the side chain of z_{n+1} ions:



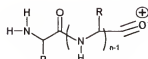
- d. The v_n ions are produced by eliminating the side chain of y_n ions along with an H-atom:



3. Nonsequential fragmentation: internal acyl ions and immonium ions:



Single a.a. immonium ion



Acyl ion

IRMPD Results

Table 5-1 summarizes the abbreviations used for amino acid residues, and **Table 5-2** lists the peptides used in this study. A typical IRMPD spectrum collected with the 9.4 T mass spectrometer at the NHMFL is given in **Figure 5-3**, which shows the IRMPD spectrum of the RGD peptide. The important peaks on the spectrum are labeled according to the nomenclature discussed above. For example, the molecular ions MH^+ occur at $m/z = 347.2$, and the fragment ions $MH^+ - NH_3$ at $m/z = 330.1$. The other main fragments seen are $b_2 + H + OH$ at $m/z = 232.1$, b_2 at $m/z = 214.1$, and $b_2 - NH_3$ at $m/z = 197.1$. It is interesting to notice that the RGD peptide only produces b type ions in the gas phase.

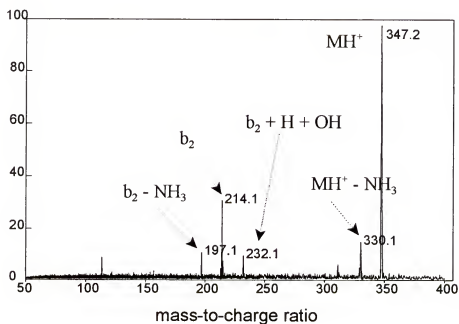


Figure 5-3.

IRMPD spectrum of RGD obtained on the 9.4 T FTICR system at the NHFML. The major peaks on the spectrum are labeled.

Table 5-1. Amino acid residues

Amino acid	Three(one) letter code	Monoisotopic mass	Average mass
Glycine	gly (G)	57.021	57.052
Alanine	Ala (A)	71.037	71.079
Serine	Ser (S)	87.032	87.078
Proline	Pro (P)	97.053	97.117
Valine	Val (V)	99.068	99.133
Threonine	Thr (T)	101.048	101.105
Cysteine	Cys (C)	103.009	103.145
Isoleucine	Ile (I)	113.084	113.160
Leucine	Leu (L)	113.084	113.160
Asparagine	Asn (N)	114.043	114.104
Aspartic acid	Asp (D)	115.027	115.089
Glutamine	Gln (Q)	128.059	128.131
Lysine	Lys (K)	128.095	128.174
Glutamic acid	Glu (E)	129.043	129.116
Methionine	Met (M)	131.040	131.199
Histidine	His (H)	137.059	137.142
Phenylalanine	Phe (F)	147.068	147.177
Arginine	Arg (R)	156.101	156.188
Tyrosine	Tyr (Y)	163.063	163.176
Tryptophan	Trp (W)	186.079	186.213

Table 5-2. List of peptides studied

Peptide #	Peptide	Average mass (Da)
1	RGD	346.2
2	RGDS	433.4
3	RGES	447.4
4	RHF	578.6
5	GRGD	403.4
6	GRGDS	490.5
7	PQRF-amide	545.6
8	GHRP	465.5
9	TPRK	500.6
10	SDGRG	490.5
11	TKPR	500.6
12	DSDPR	588.6
13	RFDS	523.5
14	YIGSR	594.7
15	GPRP	425.5
16	RGPFPI	685.8

Figure 5-4 displays the IRMPD spectrum of RGD which was obtained using a 3 T mass spectrometer at UF, and it can be seen that the results obtained with both instruments are very similar. This demonstrates that the IRMPD results are reproducible. Although both mass spectrometers provided essentially the same information, the IRMPD results reported in this chapter were acquired using the 9.4 T spectrometer.

Summary of the IRMPD results for Arg-containing peptides. It has been noted by many research groups that the presence and location of certain amino acid residues, especially Arg, influence the fragmentation spectra of proteins or peptides.^{33,132} Arginine has been identified as the most basic amino acid residue in the gas phase,¹³³ and its side chain has been pinpointed as the most favored site of protonation for singly charged ions.¹²² Therefore, most of the ions produced in a dissociation spectrum for an arginine-containing peptide contain the Arg residue. This can be illustrated by the results

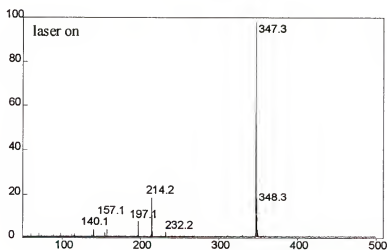


Figure 5-4.

IRMPD spectrum of collected with 3 T FTICR system at UF.

for arginine-containing peptides summarized in **Table 5-3**. The table lists the three most intense fragment ions seen for each peptide and is arranged in order as the location of Arg moves from the N-terminus to the C-terminus of the peptides. As shown in the table, three correlations between the fragmentation pattern and the location of the Arg amino acid residue within the peptide sequence can be derived from the results, (i) b_n type ion series occur as the main fragment ions when the Arg residue is located at N-terminus of the peptide; (ii) y_n type ion series are seen as the primary fragments when Arg is located at the C-terminus of the peptide sequence; and (iii) both b_n and y_n type ion series are observed when Arg is located in the middle of a peptide sequence. Correlations (i) and (ii) agree well with the results reported by Biemann's group.^{131,134} However, the IRMPD results reported above are different from the fragment ions produced from high-energy CAD experiments. As **Table 5-3** shows, the low energy IRMPD dissociation technique generates predominately b_n and y_n ion type ions which result from main-chain fragmentation of peptides. The fragmentation ions observed from CAD experiments are predominantly v_n and w_n ions which contain an Arg at the C-terminus and a_n and d_n ion series resulting from an N-terminal Arg.¹³⁵ As the definitions of v_n , w_n , and d_n ions indicate, they are produced by cleaving the side chains of y_n , z_n and a_n ions respectively. This means that interpreting CAD spectra involves an extra step of calculation of side chain loss compared to the straightforward analysis of an IRMPD spectrum since the IRMPD technique only produces peptide backbone fragments. The general trend (iii) observed for Arg-containing peptides also agrees well with the results obtained by other groups.³³ The IRMPD studies show that the three correlations enable one to distinguish Arg-containing peptides of different sequences and same mass by using MS in gas phase, and the results

also imply that a terminal Arg residue provides for optimal sequencing of a peptide due to the fact that only two ion series, y_n and b_n , are produced.

Table 5-3.
IRMPD Results of Arginine-containing Peptides

Peptide	IRMPD results	Peptide	IRMPD results
RGD	b_2 $MH^+ - NH_3$ $b_2 + H + OH$	PQRF-amide	$MH^+ - C_2H_5NHC(NH_2)NH$ b_3 y_2''
RGDS	b_3 $MH^+ - H_2O$ $b_3 - H_2O$	GHRP*	$b_3 - H_2O - NH_3$ b_3 $MH^+ - H_2O - NH_3$
RGES	$MH^+ - H_2O$ $b_3 - H_2O$ b_3	TPRK*	$b_3 + H + OH$ x_2 b_3
RHF*	b_2 $y_2'' - H_2O$ (very weak) $MH^+ - 2H_2O$	SDGRG	y_3'' $y_2'' - H_2O - NH_3$
GRGD	$MH^+ - H_2O - NH_3$ $b_2 + H_2O$ $b_3 - NH_3$	TKPR*	$MH^+ - C_2H_5NHC(NH_2)NH$ b_3 y_2''
GRGDS	b_4 $MH^+ - H_2O$ $MH^+ - H_2O - NH_3$	DSDPR	MH^+ y_2'' $y_2'' - H_2O$

* peptide contains two basic amino acids
 b_n and y_n type ions are shown in bold.

Singly charged ions ($[M+H]^+$) vs. doubly charged ions ($[M+2H]^{2+}$). Both singly (1^+) and doubly (2^+) charged ions were observed with strong intensities for the peptides PQRF-amide, DSDPR, and RGPFP. After each charge state of the peptides was individually isolated in the analyzer cell, it was studied with the IRMPD method. The IRMPD spectra obtained are given in **Figures 5-5, 5-6, and 5-7**, and the results are summarized in **Table 5-4**.

The two IRMPD spectra of the $[M+H]^+$ and $[M+2H]^{2+}$ ions of DSDPR shown in **Figure 5-5** were collected under the same conditions except stronger laser irradiation power was used to dissociate the singly charged ions than the laser irradiation power used for the doubly charged ions. The spectrum of the 1^+ ions was acquired with 28 watts of laser output power while the spectrum of 2^+ ions was obtained with only 8 watts of laser output power. **Figure 5-6** and **Figure 5-7** present the IRMPD spectra of 1^+ and 2^+ ions of PQRf-amide and RGPfPI. The PQRf-amide spectra were collected with 24 watts of laser irradiation power while the spectra of RGPfPI were collected with higher laser output power of 40 watts at 10.6 μm wavelength.

After examining the assignments listed in **Table 5-4** and comparing the appearance of the two spectra of the same peptide in **Figures 5-5** to **5-8**, it is not difficult to see that 1^+ and 2^+ molecular ions produce different fragments and generate different IRMPD spectra. For example, the singly charged ions of PQRf-amide produce primarily b_n ion series while the doubly charged molecular ions produce mainly y_n'' type ions; the singly charged molecular ions of DSDPR generate predominately y_n'' ion series while doubly charged molecular ions give a mixture of b_n and y_n'' ions; the singly charged molecular ions of RGPfPI dissociate to y_n'' ion series while the corresponding doubly charged ions provide basically b_n type ions. However, there is very little dissociation observed for the singly charged RGPfPI ions. Although different charge states of the same peptide generate different spectra, the fragment ions observed in both spectra are still dominated by only y_n'' and b_n fragment series, as observed for other peptides in this study, and reported by Hunt's group.¹³⁰

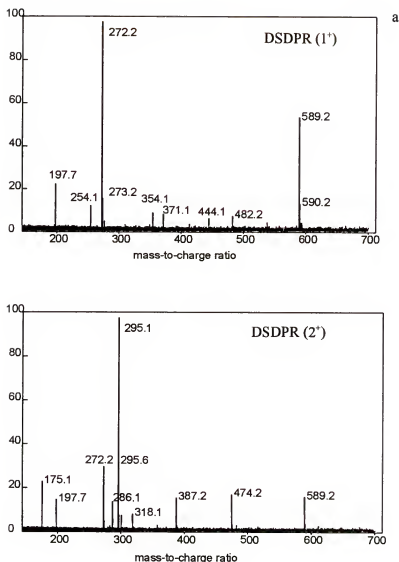


Figure 5-5.

IRMPD spectra of 1^+ and 2^+ charge states of DSDPR with both spectra collected under the same conditions except the laser output power. The 1^+ spectrum was collected with 28 watts of laser output power; the 2^+ spectrum was collected with 8 watts of laser output power at 1064 μm wavelength.

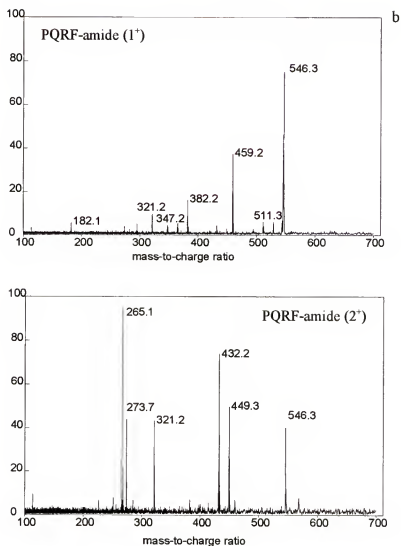


Figure 5-6.

IRMPD spectra of 1^+ and 2^+ charge states of PQRf-amide with both spectra collected under the same conditions: 24 watts of laser output power at $1064\ \mu\text{m}$ wavelength.

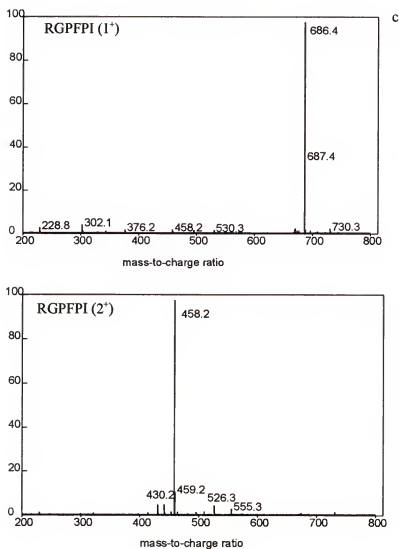


Figure 5-7.

IRMPD spectra of 1^+ and 2^+ charge states of RGPFPi with both spectra collected under the same conditions: 40 watts of laser output power at 1064 μm wavelength.

Table 5-4.

Assignments for ions produced from both 1⁺ and 2⁺ charge states of PQRf-amide, DSDPR, and RGPFPf peptides as shown in **Figure 5-4**.

Peptide	IRMPD fragments	
PQRf-amide (1 ⁺ charge state)	546.3	MH ⁺
	529.3	MH ⁺ - NH ₃
	511.3	MH ⁺ - NH ₃ - H ₂ O
	459.2	MH ⁺ - CH ₃ CH ₂ NHC(NH ₂)(NH) [*]
	382.2	b ₃
	365.2	b ₃ - NH ₃
	364.2	b ₃ - H ₂ O
	348.2	b ₃ - NH ₃ - H ₂ O
	347.2	b ₃ - H ₂ O - NH ₃
	321.2	y ₂ ^{''}
PQRf-amide (2 ⁺ charge state)	546.3	MH ⁺
	449.3	y ₃ ^{''}
	432.2	y ₃ ^{''} - NH ₃
	321.2	y ₂ ^{''}
	273.7	(M + 2H) ²⁺
	265.1	(M - NH ₃ + 2H) ²⁺
DSDPR (1 ⁺ charge state)	589.3	MH ⁺
	272.2	y ₂ ^{''}
	254.1	y ₂ ^{''} - H ₂ O
	197.7	noise
DSDPR (2 ⁺ charge state)	589.3	MH ⁺
	474.2	y ₄ ^{''}
	387.2	y ₃ ^{''}
	318.1	b ₃ (very weak)
	300.1	b ₃ - H ₂ O
	295.1	(M + 2H) ²⁺
	286.1	(MH ₂ - H ₂ O) ²⁺
	272.2	y ₂ ^{''}
	175.1	y ₁ ^{''}

^{*}CH₃CH₂NHC(NH₂)(NH) is the side chain of arginine residue.

Table 5-4--continued:

Peptide	IRMPD fragments	
RGPFPI (1 ⁺ charge state)	686.4	MH ⁺
	573.3	c ₅ ^{''}
	530.3	y ₅ ^{''}
	495.2	y ₅ ^{''} - H ₂ O - NH ₃
	458.2	b ₄
	376.2	y ₃ ^{''}
	302.1	c ₂ ^{''} +H
RGPFPI (2 ⁺ charge state)	555.3	b ₅
	526.3	b ₅ - HCO from Proline at C-terminal
	509.3	b ₅ - NH ₂ CH ₂ NH ₂ from Arg side chain
	495.2	b ₅ - H ₂ O - NH=C=NH (60)
	458.2	b ₄
	441.2	b ₄ - NH ₃
	430.2	b ₄ - CO
	413.2	b ₄ - NH ₃ - CO

By comparing the results generated from 1⁺ and 2⁺ molecular ions of the same peptide, it can also be concluded that the doubly charged molecular ions experience a greater extent of dissociation than the corresponding singly charged ions. This can be seen for all three peptides whose spectra are given in **Figures 5-5 to 5-8**. The greater extent of fragmentation for the higher charge state than the lower charge state is consistent with the charge/charge repulsion explanation of why multiply-charged proteins readily fragment in the gas phase.

Peptide fragmentation vs. laser power. The extent of fragmentation of a peptide versus the laser irradiation power was studied with the randomly chosen GRGDS, RGEs, and RGDS peptides. The relative intensities of the main fragment ions observed for each peptide are plotted against the laser output power used for producing the spectra in **Figures 5-9, 5-10, and 5-11**. The plots demonstrate that the relative intensities of the major fragment ions of each peptide increase with the laser power. Although all peptides studied show a greater extent of dissociation with higher laser power, the fragment ions remain as the main-chain cleavage ions. As the laser power increases, the losses of NH₃ and H₂O from fragment ions are common to see as shown by the plot of RGDS given in **Figure 5-9**. For example, both b₃ - H₂O and b₃-H₂O-NH₃ ions are seen along with the b₃ ion at higher laser power. Since the intensities of two newly formed ions from b₃ ions increase with the laser power, the growth of intensity of b₃ ions is slowed. Therefore, in IRMPD experiments the proper laser power needs to be controlled for producing maximal amount of low-energy dissociation fragments.

TPRK vs. TKPR. When two strong basic amino acid residues, K and R, are present in the same peptide, such as TPRK and TKPR, the fragmentation pattern does not

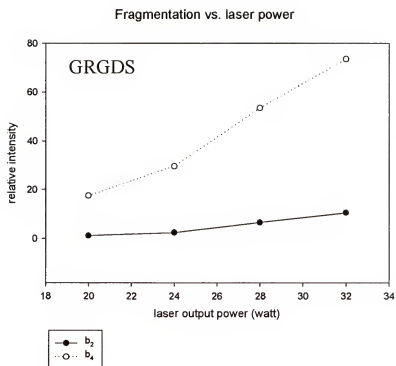


Figure 5-9.

Plots of relative intensities for major fragment ions b_2 and b_4 of GRGDS observed in the IRMPD spectra vs. laser output power of the experiments.

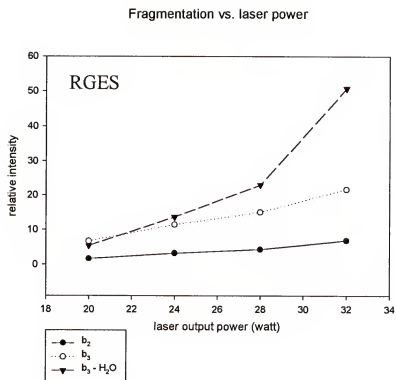


Figure 5-10.

Plots of relative intensities for major fragment ions b_2 , b_3 , and b_3-H_2O of RGES observed in the IRMPD spectra vs. laser output power of the experiments.

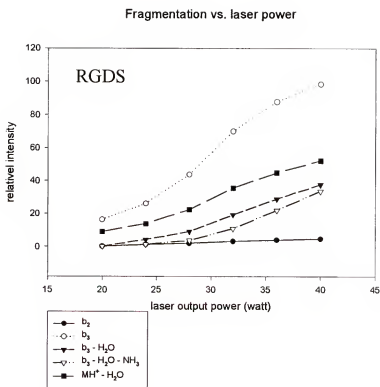


Figure 5-11.

Plots of relative intensities for major fragment ions b_2 , b_3 , b_3-H_2O , $b_3-H_2O-NH_3$, and $MH^+ - H_2O$ of RGDS observed in the IRMPD spectra vs. laser output power of the experiments.

always strictly follow the predictions from earlier in this chapter: b_n type of fragment ions are observed for N-terminal Arg-containing peptides and y_n type of ions are generated for C-terminal Arg-containing peptides. Discrepancies can be seen from the results for TPRK and TKPR peptides summarized in **Table 5-5**. The table shows that TKPR produces both b_n and y_n ion series rather than only y_n type of ions which are seen for C-terminal Arg-containing peptides. For the TPRK peptide, x_n ions are observed along with b_n ions, instead of the mixture of y_n and b_n ions obtained for peptides with Arg in the mid-sequence. This observation implies that the fragmentation mechanism of these peptides with more than one strong basic residue is different from that of peptides containing only one basic amino acid. The different fragmentation mechanism is probably due to the availability of more than one protonation site in the amino acid sequence.

Although TPRK and TKPR contain exactly the same amino acid residues with only different orders of arrangement, the appearances of their IRMPD spectra are completely different, as shown in **Figure 5-12**. Even though both spectra were collected with 20 watts of laser output power and the same experimental conditions, TPRK obviously dissociates to a greater extent than TKPR. Since TPRK contains two strong basic amino acid residues, arginine and lysine, right next to each other in the peptide, stronger protonation competition between the basic R-groups of the amino acid residues could occur. Since the charge/charge repulsion mechanism guides the peptide fragmentation in the gas phase, it is not surprising that a greater extent of fragmentation occurred for peptides containing higher number of basic amino acid residues and for peptides with their basic amino acid residues located close to each other within the sequence.

Table 5-5.

List of assignments for ions observed in the IRMPD spectra of TPRK and TKPR peptides.

Peptide	IRMPD fragments	
TPRK	501.3	MH^+
	483.3	$\text{MH}^+ - \text{H}_2\text{O}$
	457.3	$\text{MH}^+ - \text{CO}_2$
	439.3	$\text{MH}^+ - \text{CO}_2 - \text{H}_2\text{O}$
	373.2	$\text{b}_3 + \text{H} + \text{OH}$
	355.2	b_3
	337.2	$\text{b}_3 - \text{H}_2\text{O}$
	329.2	x_2
	320.2	$\text{b}_3 - \text{H}_2\text{O} - \text{NH}_3$
	311.2	$\text{x}_2 - \text{H}_2\text{O}$
	293.2	$\text{x}_2 - 2\text{H}_2\text{O}$
	276.1	$\text{x}_2 - 2\text{H}_2\text{O} - \text{NH}_3$
TKPR	501.3	MH^+
	483.3	$\text{MH}^+ - \text{H}_2\text{O}$
	457.3	$\text{MH}^+ - \text{CO}_2$
	439.3	$\text{MH}^+ - \text{CO}_2 - \text{H}_2\text{O}$
	379.2	unable to assign
	345.2	$\text{b}_3 + \text{H} + \text{OH}$
	327.2	b_3
	309.2	$\text{b}_3 - \text{H}_2\text{O}$
	272.2	y_2''
	254.2	$\text{y}_2'' - \text{H}_2\text{O}$
	230.1	b_2
	212.1	$\text{b}_2 - \text{H}_2\text{O}$

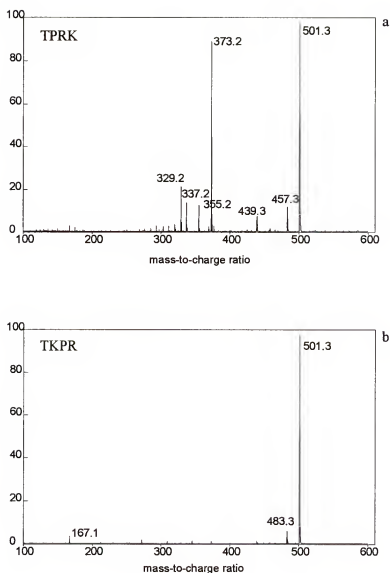


Figure 5-12.

The IRMPD spectra of TPRK and TKPR peptides. Both spectra were collected with same laser output power (20 watts) and exactly the same experimental conditions: a) TPRK, b) TKPR.

SORI-CAD vs. IRMPD

The sustained-off-resonance collisionally activated dissociation (SORI-CAD) method is another well accepted low-energy dissociation technique for protein or peptide sequencing in gas phase. Dissociation of some peptides, such as SDGRG, GPRP, and YIGSR, was studied with a pressure of 10^{-7} torr of Ar as the collision gas using the SORI-CAD method on the 4.7 T instrument at UF, and the results obtained were compared with the corresponding IRMPD results. Although most of the results obtained from both approaches are compatible (see **Figures 5-13, 5-14, and 5-15**), the IRMPD method can provide more fragmentation information for some peptides such as the GPRP peptide given in **Figure 5-13**. The IRMPD method not only provides sufficient fragment ions, it also provides a cleaner spectrum than the SORI-CAD method, especially in the low mass region, as shown in the spectrum of RGES in **Figure 5-14**.

It has been demonstrated that if experimental conditions, including neutral gas pressure, reaction delay, and excitation power are well controlled, the SORI-CAD method can produce a very similar spectrum to the one generated using the IRMPD approach. However, if one of the parameters is not optimized properly, the resultant spectrum can be very different from the IRMPD spectrum. When the collision gas pressure is too high, the reaction delay is too long, or the excitation power is too strong, complicated spectra can arise from excessive dissociation. For example, **Figure 5-15** shows a complicated spectrum obtained for the peptide RGES using SORI-CAD technique. It is obvious that the many peaks seen, especially in the low mass region, are much more difficult to analyze than a simpler IRMPD spectrum (see **Figure 5-15**).

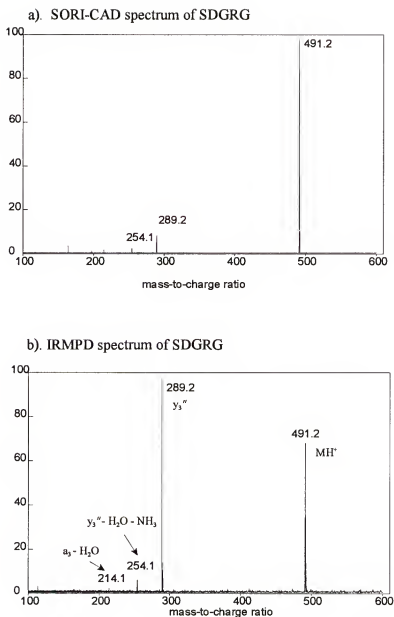


Figure 5-13.

Comparison of an IRMPD spectrum vs. a SORI-CAD spectrum obtained for the SDGRG peptide. a). IRMPD spectrum obtained with the 9.4 T instrument at NHMFL, b). SORI-CAD spectrum obtained with the 4.7 T instrument at UF.

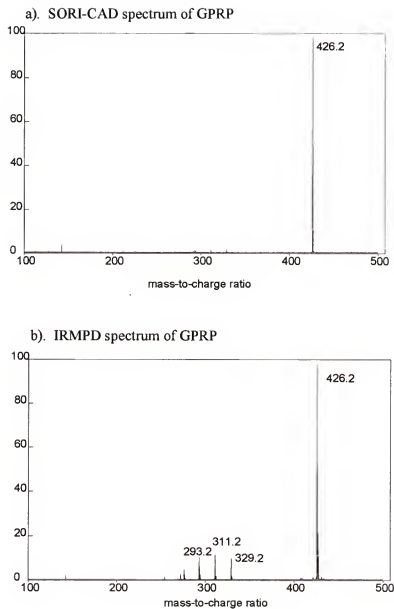


Figure 5-14.

Comparison of SORI-CAD and IRMPD spectra of the GPRP peptide.

a). SORI-CAD spectrum, b). IRMPD spectrum.

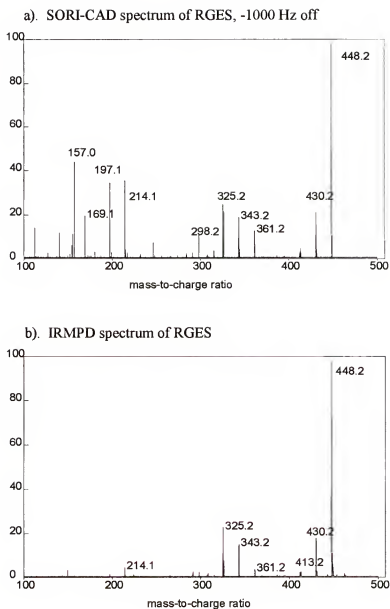


Figure 5-15.

Comparison of IRMPD and SORI-CAD spectra of the RGES peptide.

a). SORI-CAD, b). IRMPD

This study has shown that the SORI-CAD and IRMPD methods can provide essentially the same information if the experimental parameters of both methods are properly controlled. However, once one has bought the laser and has properly aligned it, the only experimental parameters that need to be adjusted are the irradiation time and the laser power. For SORI, every dissociation experiment requires that the neutral gas pressure and excitation power be properly controlled. Therefore, the IRMPD approach seems to be the ideal choice for peptide sequencing in the gas phase.

Conclusions

Studies of IRMPD of Arg-containing peptides in the gas phase reveal the importance of gas-phase fragmentation, and the correlations can be used to distinguish the location(s) of Arg in a peptide, which can lead to rapid peptide sequencing. The general relationships between the peptide fragmentation patterns in the gas phase and the location of an arginine residue in a peptide can be summarized as: b_n type ions are observed as the primary fragmentation series when the Arg residue is located at the N-terminus of the peptide; y_n type ions are seen as the principal fragmentation series when the Arg residue is located at the C-terminus of the peptide; and a mixture of mainly b_n and y_n type ions is observed in the dissociation spectra when the Arg residue is located in the middle of the peptide sequence. A second major observation for the Arg-containing peptides is that losses of H_2O and NH_3 lead to prominent fragment peaks in the spectrum.

The results of this study also show that a greater extent of fragmentation is observed for higher charge state molecular ions than lower charge state molecular ions when the dissociation spectra of 1^+ and 2^+ charge states for several peptides are examined.

It was also seen that the fragmentation pattern is not always strictly followed by the peptides that contain more than one basic amino acid residue in the sequence. When the peptide fragmentation is studied as a function of the irradiating laser power, the results show that increasing the laser power generally increases the amount of peptide dissociation. In conclusion, this study has shown that IRMPD is a true low-energy dissociation technique when compared to SORI-CAD techniques, producing only peptide backbone fragmentation. It may be the ideal method for peptide or protein sequencing with MS in the gas phase.

CHAPTER 6

INVESTIGATING CHEMICALLY MODIFIED RNASE A WITH ESI-FTICR/MS

Introduction

Over the past ten years, developments in MS have made it possible to study many biological systems, including complexes arising from noncovalent interactions between ligands and receptors,^{136,137} subunits of protein complexes,^{138,139} and oligonucleotides.²⁴ Other compelling biological problems lie in the world of modified enzymes.¹⁴⁰ Although these modified enzymes are somewhat useful, their rate enhancements do not match those of any naturally occurring enzymes. Thus, improving the turnover rate of a modified enzyme has been an important goal. One means of achieving this goal is covalent modification of a naturally occurring enzyme with a transition metal cofactor. This improves the binding properties of the enzyme with the catalytic enhancement of the cofactor.

Due to its feasibility for the direct analysis of multicomponent proteolytic peptide mixtures (peptide mapping), MS has been demonstrated as a powerful method in the identification of covalent post-translational modifications^{141,142} and of multiple chemical modification sites.²⁹ The mass spectrometric peptide mapping method has been successfully employed to investigate specific modification reactions such as amino-acylation, carboxylate-amidation, and the bifunctional cysteine-modification by phenyl

arsinoxide.¹⁴³⁻¹⁴⁵ The experiments reported in this chapter were directed at following the chemical modification process of ribonuclease.

The enzyme ribonuclease, chosen for this study, has been known as RNase, RNase A, RNase I, pancreatic ribonuclease, and a pancreatic enzyme. It is the most stable and well characterized enzyme at the molecular level. The 124 amino acid residues give the protein a molecular weight of 13,680 Da. RNase A contains four disulfide bonds, which occur between residues 26 and 84, 40 and 96, 58 and 110, and 65 and 72, as shown in **Figure 6-1**. When the bridges are reduced, the protein is denatured and becomes inactive. However, it is possible to reduce the bridges partially and retain the activity of the enzyme. Removal of four peptides at the carboxyl terminus also destroys enzyme activity. RNase A is an endoribonuclease which cleaves RNA to both mononucleotides and oligonucleotides in a two step process¹⁴⁶ as shown in **Figure 6-2**. In the first step, a cyclic 2',3'-phosphate intermediate is produced, due to intramolecular attack by the 2'-OH group of the ribose moiety on the phosphodiester linkage. The second step involves hydrolysis of the cyclic 2', 3'-phosphate, resulting in the formation of a terminal 3'-monophosphate ester. The enzyme has its highest activity with single stranded RNA, and it has very low activity with double stranded RNA.

The His-12, His-119, and Lys-41 residues have been shown to be associated with the active site of RNase A,¹⁴⁷ and the N-terminal lysine is located adjacent to Lys-41. As the 3-dimensional structure in **Figure 6-3** shows, the N-terminal Lys is more exposed to the environment, so it can be easily accessed and acetylated.¹⁴⁸ Therefore, RNase A seems to be an ideal choice for enzyme modification with the N-terminal lysine as the target for

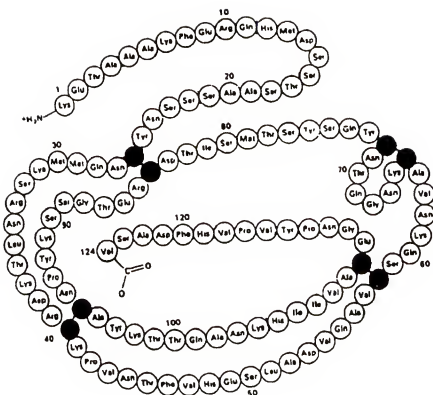


Figure 6-1.

Amino acid structure of RNase A. The four disulfide bonds formed from eight cysteine residues are shown in black.

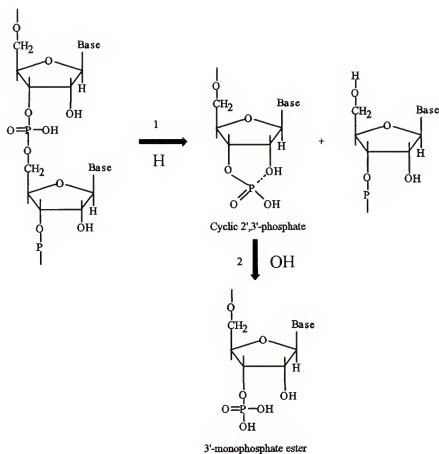


Figure 6-2.

Two-step reaction of RNase A with RNA: in the first step, a cyclic 2',3'-phosphate intermediate is produced, due to intramolecular attack by the 2'-OH group of the ribose moiety on the phosphodiester linkage; the second step involves hydrolysis of the cyclic 2', 3'-phosphate, resulting in the formation of a terminal 3'-monophosphate ester



Figure 6-3.

Ribbon structure of RNase A with N-terminal lysine labeled as N; the four disulfide bridges are shown in black balls and sticks.

modification. In this chapter, the initial results of a study of purification, modification, denaturation, and digestion obtained using ESI-FTICR/MS are reported.

Experimental

Materials

The native and oxidized RNase A samples were purchased from Sigma Chemical Co. (St. Louis, MO.) The native RNase A was purified and chemically modified with the proper modifiers, and all ESI samples were prepared in concentrations of about 1×10^{-6} M or less in 49/49/2 (v/v/v) methanol/water/acetic acid by Trisha Joy Mendez in the Inorganic Division of Chemistry Department at the University of Florida. The HPLC peptide standard mixture, used for identifying the HPLC separated peptides with MS, included five peptides: Gly-Try (238 Da), Val-Try-Val (379 Da), methionine enkephalin acetate (Try-Gly-Gly-Phe-Met, 573 Da), leucine enkephalin (Try-Gly-Gly-Phe-Leu, 555 Da), and angiotensin II acetate (Asp-Arg-Val-Tyr-Ile-His-Pro-Phe, 1046 Da). The peptide mixture was also purchased from Sigma Chemical Co. (St. Louis, MO.)

Mass Spectrometer

All mass spectrometric experiments were performed with a shielded 4.7-Tesla FT-ICR mass spectrometer (Bruker Analytical Systems Instruments, Inc., Billerica, MA) at the University of Florida. A detailed description of the instrument can be found in the experimental section of chapter 5 of this dissertation. The capillary is a heated metal capillary which was modified from an Analytica electrospray source (Analytica of Branford, Branford, CT).

All data were collected with a cell pressure of 1×10^{-9} torr, and the SORI-CAD experiments were performed with either Kr or Ar as the collision gas at a pressure of 1×10^{-7} torr. The samples were sprayed at a rate of $1 \mu\text{l}/\text{min}$, and the stainless steel capillary was maintained at a temperature of 120°C . The electrospray conditions were tuned to optimize the signals of interest. The electrospray needle was located at a distance typically about 1 cm away from the capillary, which provided maximal ion current and optimal signals. The capillary and skimmer voltage were adjusted to values which maximized the signal intensities for the ions of interest, and typical values were around 100 and 10 volts for the capillary and skimmer, respectively.

Molecular Weight (M_r) Determination for Large Biomolecules

ESI/MS has been well known for its ability to provide accurate molecular weight determination for many biological systems, including bovine insulin, bovine trypsin, and bovine carbonic anhydrase. Large biomolecules sprayed with the electrospray ionization technique have a distinctive pattern of peaks in which adjacent peaks always appear to vary by addition or subtraction of one charge for the ions observed in the spectrum, and the average charge state is observed to increase in an approximately linear fashion with the average molecular weight of the biomolecule (M_r).⁸⁹

The M_r of a macromolecule can be easily determined from mass spectra with the general assumption that adjacent peaks of a charge state distribution differ by only one charge, and that ions are produced by proton attachment to the molecular ion.⁸⁹ Although determination of M_r has been automated by many data systems, the basis used to calculate the M_r of a protein has stayed the same. In order to understand the spectra of multiply charged ions in ESI/MS, it is important to understand the basis for determining the molecular weight with MS.

A typical positive ion spectrum of a single protein consists of a series of peaks with each one representing the molecular ion plus a specific number of protons. The ions have the general form:

$$(M + nH)^{n+}$$

where M is the M_r of the protein, n is an integer represents the number of protons attached to the protein, and H is the proton with mass of 1.00794 Da. Since MS measures mass-to-charge ratios (m/z), each peak seen on a typical spectrum can be expressed as:

$$m/z = (M + nH) / n$$

If both m/z and n are known, M can be readily calculated as:

$$M = n (m/z - H)$$

If either M or n is known, M and n can be determined from two equations derived from two consecutive peaks $(m/z)_1$ and $(m/z)_2$ differing by one proton in the series,

$$(m/z)_1 = (M + n_1H) / n_1$$

$$(m/z)_2 = (M + n_2H) / n_2$$

where $(m/z)_1 < (m/z)_2$, and $n_2 = n_1 - 1$. Solving $(m/z)_1$ and $(m/z)_2$ equations yields:

$$M = n_2 ((m/z)_1 - 1)$$

and

$$n_2 = ((m/z)_1 - 1) / ((m/z)_2 - (m/z)_1)$$

For example, with two adjacent peaks in a charge state distribution of a protein with $(m/z)_1 = 1223$ and $(m/z)_2 = 1426$,

$$n_2 = ((m/z)_1 - 1) / ((m/z)_2 - (m/z)_1) = (1223 - 1) / (1426 - 1223) = 6.02$$

the charge state n_2 is calculated as 6, therefore the molecular weight of the protein can be determined with this newly determined n_2 value.

$$M = n_2 ((m/z)_1 - 1) = 6 (1223 - 1) = 7332 \text{ Da.}$$

Results and Discussion

The overview of this project and the general procedure followed are illustrated with the flow chart in **Figure 6-4**. The very first step of the project was to check the purity of the protein of interest to assure that it was initially clean. Given that the sample size in this project is quite small (100 μ l sample with concentration of 10^{-6} M), a quite small contamination of the RNase A samples could be a potential hazard which could block the effectiveness of the planned chemical modification. Impurity of the sample can also lower the effective mass resolving power of the mass spectrometer and decrease the instrumental detection limit. Hence, the goal of the very first step was to examine the purity of the native RNase A sample purchased from the Sigma Chemical Co. After the native RNase A was purified using the purification steps illustrated in the flow chart of **Figure 6-5**, the second step was to chemically modify the protein with proper modifiers and confirm the modification by measuring the molecular weight for both native and modified RNase A with ESI-FTICR/MS. At this point it is important to know that the protein only increases its molecular weight by the molecular mass difference of one modifier molecule from its native form since modifying only the N-terminal lysine is the goal of the project. After the native protein was confirmed to be singly modified, the third step was to identify the exact modification site using either MS alone or the peptide mapping MS technique. In the peptide mapping MS approach, the protein of interest is first enzymatically digested to yield a peptide mixture; then the HPLC technique is used to separate the peptide mixture; next MS is used to identify the HPLC aliquots and to sequence the peptides; and finally the peptide sequences are examined carefully and are used to derive the complete sequence of the protein. Although different dissociation methods such as Sori-CAD, Capillary-

skimmer(CS), and photodissociation (PD) were tried to fragment the gas phase proteins, no method provided enough useful information for pinpointing the modification site. Since MS alone was not successful in sequencing the protein, the peptide mapping technique, which was demonstrated as a powerful method for identifying partial protein modifications, was employed. The results obtained will be categorized and discussed in more detail below in their appropriate section.

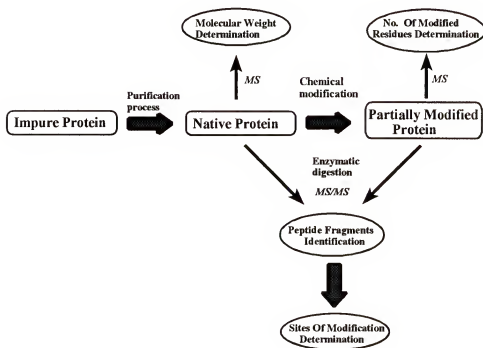


Figure 6-4.

Overview of the project with processes leading to various forms of the protein labelled.

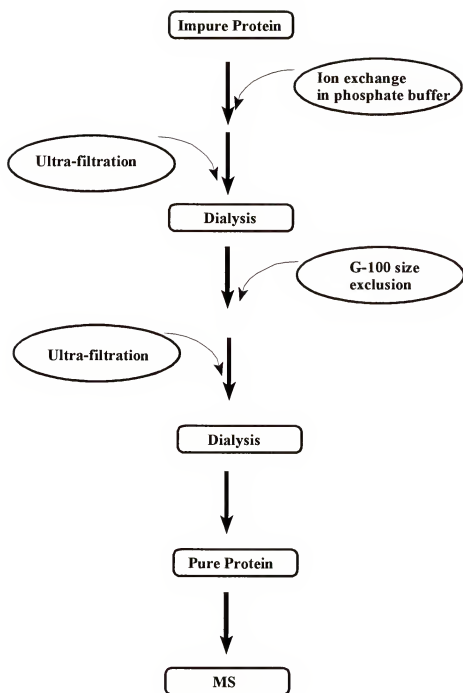


Figure 6-5.

Process used for purifying the RNase A protein.

Native RNase A

The spectrum of the unpurified RNase A sample is given on the top of **Figure 6-6** and the spectrum of the purified sample is given on the bottom of **Figure 6-6**. Each spectrum presented in **Figure 6-6** is the sum of 16 individual transients with 128k data points collected. In this chapter, while the horizontal axis represents the mass-to-charge ratio for every spectrum, the vertical axis is plotted as absolute intensity unless otherwise is specified. The impure spectrum clearly shows that the native RNase A has contamination in the region of m/z 100-1500. Comparison of the two spectra indicates that a much cleaner sample emerged following the purification process. Due to the impurity present in the sample, the top spectrum barely shows three charge states while the purified sample provides five charge states. The purified sample shows about a factor of 100 enhancement in its signal-to-noise ratio. The spectrum of purified RNase A in **Figure 6-6** was used to determine the average molecular weight of RNase A, and the calculated value was 13,686 kDa.

One distinct feature of the spectra shown in **Figure 6-6** is that every charge state of the protein has a few peaks which correspond to phosphate or sulfate adducts with a mass ca. 98 Da higher than the unaddicted peaks. It is common to see complexes with 1, 2, and 3 phosphate or sulfate groups, which are noncovalently bound to the protein in ESI/MS spectra such as these. For example, the 8^+ charge state of the molecular ion corresponds to m/z 1711.8149, and the molecular species containing one and two phosphate or sulfate groups are observed at m/z 1711.8149 and 1724.0463, respectively. Assignments of other signals seen in the spectra are listed in **Table 6-1**.

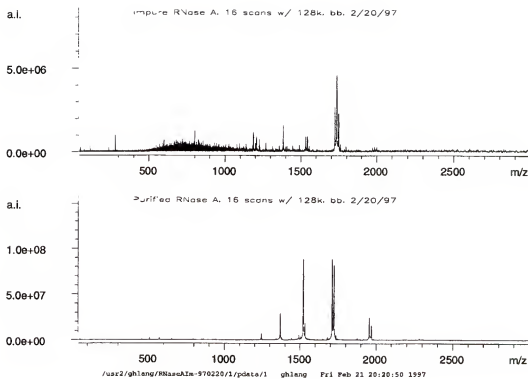


Figure 6-6.

Spectra of impure and purified RNase A collected under the same experimental conditions with a background pressure of 10^{-9} torr and a sample concentration of 10^{-6} M in 49/49/2 methanol/H₂O/acetic acid. Each spectrum is the result of accumulation of 16 individual transient with 128k data points. The top spectrum shows the impure sample purchased from Sigma Chemical Co., and the bottom one shows the purified RNase A sample.

Table 6-1.

Mass spectrometric signals observed in purified native RNase A and their assignments.

m/z	Assignment
1245.1952	$(M + 11 H)^{11+}$
1369.5558	$(M + 10 H)^{10+}$
1521.7966	$(M + 9 H)^{9+}$
1532.6397	$^*(M + 9 H + P)^{9+}$
1711.8149	$(M + 8 H)^{8+}$
1724.0463	$(M + 8 H + P)^{8+}$
1956.8958	$(M + 7 H)^{7+}$
1970.8195	$(M + 7 H + P)^{7+}$

* P is the abbreviation for phosphate

Discussion of Phosphate Adducts

Multiple additions of roughly 98 Da have been observed accompanying the molecular ions of large biomolecules, as are seen for RNase A in **Figure 6-6**. The mass increase of roughly 98 Da could correspond to addition of a phosphate or sulfate group since both of them have similar molecular mass. Because most of the published literature reports the 98 Da adducts as phosphate adducts,¹⁴⁹ the adducts will be referred as phosphate group throughout this dissertation. As previously reported by many groups,¹⁵⁰ the number of phosphate adducts increases as the charge state decreases or the m/z value increases. Chait's group has reported that the phosphate ion can be dissociated from the protein by treating the sample with barium acetate,¹²⁴ and studies by Bruce and et al.¹⁵¹ show that the phosphate can be readily dissociated in the heated capillary inlet. However, dissociation by collision activation in the capillary-skimmer region is less effective, and the dissociation is significantly reduced when the complexes are collisionally activated in the ICR cell where other dissociation processes dominate.

Dissociation Studies of the Isolated 8⁺ Charge State

One of the advantages of FT/MS is that the ions of interest can be isolated and stored for many minutes, if desired, while other reactions with the isolated ions can be carried out in the trap. This feature assures that the reactions of the ions of interest are not influenced by the contaminants in the reaction cell. For example, the 8⁺ charge state with various phosphate adducts of native RNase A at *m/z* 1711 can be isolated (see the top spectrum of **Figure 6-7**), and the complete isotopic distribution of the 8⁺ charge state without the phosphate adducts can also be isolated (shown in the bottom spectrum in **Figure 6-7**) due to the ultrahigh resolving power of the FT/MS instrument.

After the 8⁺ ions are isolated, various dissociation methods such as SORI-CAD, photo-dissociation with a UV-visible laser (355 nm and 532 nm), and capillary-skimmer dissociation (CS-CAD) were tried in order to dissociate the 8⁺ ions. However, the amount of fragmentation of the protein ions was not sufficient to be an effective aid in partial gas phase sequencing (see **Figure 6-8**). The low extent of fragmentation is probably due to the large number of degrees of freedom which exist in RNase A, so the energy absorbed by the system from the dissociation methods is not enough to raise the internal energy high enough to cause the precursor ion to dissociate.

Singly Modified RNase A

Once satisfactory purity of the RNase A sample was achieved, the next step was to chemically modify the protein at the N-terminal lysine. In this step, it is important to insure that the modification takes place at only one site on the protein; in other words, the molecular mass of the modified protein can only be different by one molecular mass of the modifier from the native protein.

Modification with 2-iminothiolane. One of the chemical modifiers tried by Ms. Mendez was 2-iminothiolane ($C_4H_7NS \cdot HCl$, $mw = 137.6$ Da) whose reaction mechanism with a lysine amino residue is illustrated in **Figure 6-9**. The mechanism indicates that 2-iminothiolane is added to the

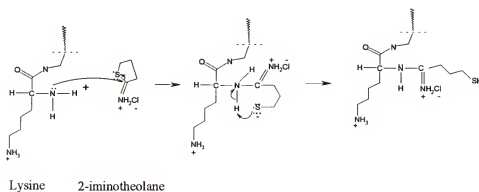


Figure 6-9.

Reaction mechanism of 2-iminothiolane with a lysine amino acid residue of a protein. The middle structure of the reaction is the intermediate, and the final product is shown on the right.

N-terminal nitrogen atom of the lysine residue. If only the N-terminal lysine is modified, the protein should increase its molecular weight by approximately 137.6 Da, corresponding to one 2-iminothiolane molecule. However, when the modified solution was examined by ESI-FTICR/MS, the mass spectrum collected (see **Figure 6-10**) implied that more complicated modifications had occurred in solution than were expected. **Figure 6-10** gives the mass spectrometric results for one of the 2-iminothiolane modifications. The top spectrum of the figure shows that three charge states of 9^+ , 8^+ , and 7^+ are clearly seen around 1500, 1700, and 2000, respectively, with many extra peaks occurring within each charge state compared to the spectrum of the native protein given in **Figure 6-6**.

Since the 8^+ ions are the most intense peaks in the spectrum, the m/z 1700-1900 mass range was expanded for a closer examination of the individual peaks. This is shown in the bottom two spectra, with the left spectrum being the expansion for all three charge states and the right one being the expansion for only 8^+ ions. When the extra peaks were closely analyzed, they actually corresponded to different combinations of 2-iminotheolane and phosphate adduct additions to the native RNase A. The peaks of 1725.28 could be the 8^+ molecular ion with one phosphate adduct, 1742.84 could correspond to the 8^+ ions with addition of one 2-iminotheolane molecule. Although the 2-iminotheolane modification did not give the expected single modification results, it would provide confidence that the RNase A protein could be modified, even singly, with proper modifiers under the proper conditions. Since 2-iminotheolane gave more modification than expected, the search for the right chemical modifier continued.

Modification with N-hydroxysuccimide acetate (NHS-acetate). The next modifying reagent tested was N-hydroxysuccimide acetate (NHS-acetate) whose reaction with a N-terminal lysine amino acid residue is given in **Figure 6-11**.¹⁵² As the reaction scheme depicts, the NHS-acetate reagent works differently from the 2-iminotheolane reagent. NHS-acetate adds only 41Da (-OCCH group from the NHS-acetate reagent) to the nitrogen atom of the N-terminal lysine while a whole molecule of 2-iminotheolane is attached to the N-terminal nitrogen atom of a N-terminal lysine residue of the protein. The addition of -OCCH “neutralizes” the side chain of the Lys, and the positive charge on the nitrogen atom relocates to another part of the protein.

The 41 Da mass addition, implying a single modification, was detected when the NHS-acetate modified protein sample was examined with ESI-FTICR/MS. A typical mass

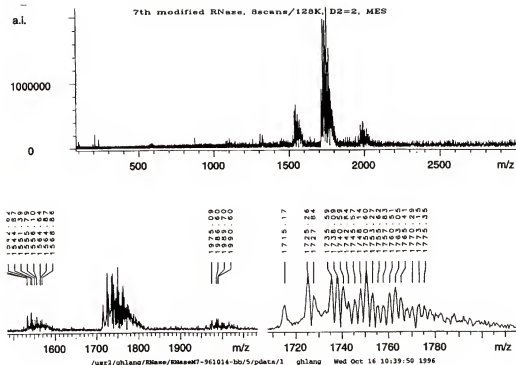


Figure 6-10.

A typical mass spectrum of the 2-iminotheolane modification on the RNase A protein. The top spectrum shows the complete mass-to-charge region between 200 to 3000; the bottom left spectrum gives the expansion of all 9⁺, 8⁺, and 7⁺ charge states; and the bottom right spectrum provides a greater expansion for only the 8⁺ charge state.

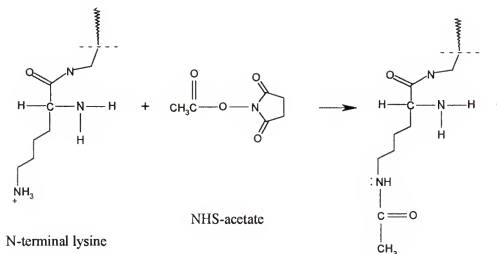


Figure 6-11.

Reaction of N-hydroxysuccinimide acetate (NHS-acetate) with the N-terminal lysine amino acid residue of a protein.

spectrum collected for the NHS-acetate modified RNase is shown in the bottom spectrum of **Figure 6-12**, and its corresponding native RNase A spectrum is given on the top of the figure. Both spectra display the region of m/z 1300-2100, where the protein signals appear. The bottom spectrum of the modified protein clearly exhibits four sets of signals which correspond to the charge states 7^+ , 8^+ , 9^+ , and 10^+ at m/z around 1900, 1700, 1500, and 1300, respectively. When the spectrum, especially the 8^+ charge state, is carefully examined, two distinctive series of signals can be revealed on the same spectrum. One ion series is more intense than the other, and the signals of one series occur in between the signals of the other series, with the observation especially pronounced for the 8^+ ions. The set of stronger signals at m/z 1716.64, 1728.92, and 1741.01 represent the modified proteins, and the set of weaker signals occurring at m/z 1711.51 and 1723.52 correspond

to the native proteins. The mass difference between 1716.64 of the modified protein and 1711.51 of the native protein is exactly 41 Da, which corresponds to the exact mass of a single acetate group. The addition of 41 Da implies that the native protein is singly and successfully modified with the NHS-acetate reagent. **Table 6-2** summarizes the assignments for all the peaks seen in the spectrum of the modified peptide shown in **Figure 6-12**. The signals of the charge state 7⁺ are not listed in the table due to their low intensities. The mass spectrometric results show that RNase A can be successfully and singly modified with the NHS-acetate reagent given the proper solution environment, including the pH value of the solution and correct ratio of protein to modifier.

Table 6-2.

List of signals observed on the modified RNase A spectrum shown in Figure 6-13, and their assignments.

m/z	Assignment
1373.58	(M + 10 H + NHS-acetate) ¹⁰⁺
1521.60	(M + 9 H) ⁹⁺
1526.08	(M + 9 H + NHS-acetate) ⁹⁺
1536.86	(M + 9 H + P + NHS-acetate) ⁹⁺
1711.51	(M + 8 H) ⁸⁺
1716.64	(M + 8 H + NHS-acetate) ⁸⁺
1723.57	(M + 8 H + P) ⁸⁺
1728.92	(M + 8 H + P + NHS-acetate) ⁸⁺
1741.01	(M + 8 H + 2P + NHS-acetate) ⁸⁺

Methodology Development for Locating the Protein Modification Site

After the protein was proven to be successfully and routinely modified with NHS-acetate reagent, the next step was to identify the exact site of the modification. One question which needed to be answered was: Does the modifying reagent really modify the N-terminal lysine as it was originally anticipated? To answer this question is not as easy as

it seems. In the following few sections, the methodology developments of searching for the proper approach will be described.

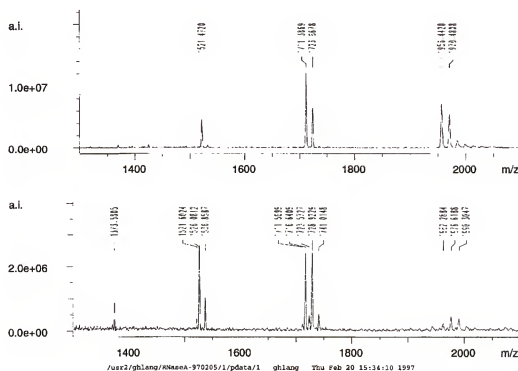


Figure 6-12.

Comparison of the spectrum between the native RNase A sample (see the top spectrum) and the singly modified RNase A with NHS-acetate (given in the bottom spectrum).

In the beginning, pure gas phase dissociation techniques such as sustained off-resonance irradiation collisionally activate dissociation (SORI-CAD), photodissociation (PD), and skimmer capillary collisionally activated dissociation (SC-CAD) were tried to achieve the goal of partially sequencing the protein in gas phase. However, as the SORI-CAD spectrum in **Figure 6-8** shows, these techniques did not generate any useful fragments which could be used to aid the partial peptide sequencing in the gas phase to identify the peptide modification site.

The next method checked was the peptide mapping method with mass spectrometry. As described earlier, the first step of the method is to digest the RNase A with a proper protease (trypsin in this case); then to apply the reverse phase high pressure liquid chromatography (HPLC) technique to separate the small peptide mixture resulting from the digestion process; and finally to use ESI-FTICR/MS to examine each HPLC aliquot and sequence the peptide using the MSⁿ method. **Figure 6-13** illustrates the general guidelines used in the present project. The first step is to denature the RNase A with guanidine HCl, which cleaves the hydrogen bonds and eliminates the Coulombic interactions within the protein. The four disulfide bonds are more accessible to the environment following the protein denaturation, so the second step is to reduce these disulfide bonds with a proper reducing reagent such as dithiothreitol (DTT). Since the process of reducing the disulfide bonds opens four sulfur-sulfur bonds, it provides eight highly reactive -SH groups, and the immediate following step is to protect or block these active -SH groups with 4-vinyl pyridine to prevent reformation of the disulfide bonds. In the last step, the protected protein is ready to be digested with the trypsin enzyme, which only cleaves the carbon side of peptide bond at arginine and lysine except when lysine is located adjacent to a proline amino acid residue, to yield a peptide mixture. Before MS is used to identify the peptides in the mixture, reverse phase HPLC is used to separate the peptide mixture.

With this method, both native and modified RNase A are digested with trypsin, which should cleave both proteins at the similar sites. The peptide mixtures resulting from both proteins are essentially the same except one or more of the digested peptides from the modified protein should be 41 Da heavier than the corresponding peptide from the

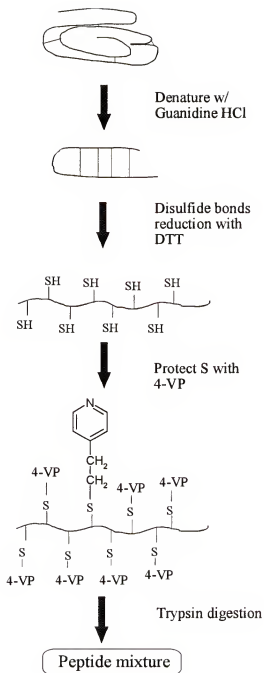


Figure 6-13.

Pictorial representation of the peptide mapping method including the processes such as protein denaturation, disulfide bonds denaturation, and protein digestion.

native RNase A. When the peptides of the native RNase A are identified, they then are compared with the digested peptides obtained from the modified RNase A to fish out the modified fragment. Once the modified fragment is identified, MSⁿ experiments will be performed to pinpoint the specific site of the RNase A modification.

Denatured and Reduced Forms of RNase A

Figure 6-14 a) and b) display the spectral results of the native RNase A and its reduced form. After examining the two spectra given in **Figure 6-14**, it can be seen that the multiple charge distribution envelope of the reduced RNase A is shifted to a lower mass-to-charge range (meaning higher charge states) than the native form. This observation can be explained by noting that the reduced protein provides more possible basic sites for protonation, leading to higher charge states following protonation. Such a charge envelope shifting phenomenon has also been observed by Smith's group.¹⁵³ For example, the charge states observed for the reduced form of RNase A range from 10⁺ to 19⁺ while the native RNase A only produces charge states ranging from 7⁺ to 11⁺. The reduced RNase A reported in **Figure 6-14 b** is about 850 Da heavier than its native form (see **Figure 6-14 a**), and the 850 Da is due to the addition of the eight protecting groups (4-vinyl pyridine) to the eight formerly bridging sulfur atoms of the reduced RNaseA.

Identifying the HPLC Separated Peptides with MS

The fourth step of the general approach of the peptide mapping method shown in **Figure 6-13** is to digest the disulfide-reduced proteins with trypsin. The peptide mixture generated from the digestion process is then diagnosed by MS after the peptides are separated using the reverse phase HPLC technique. Before MS was used to examine the

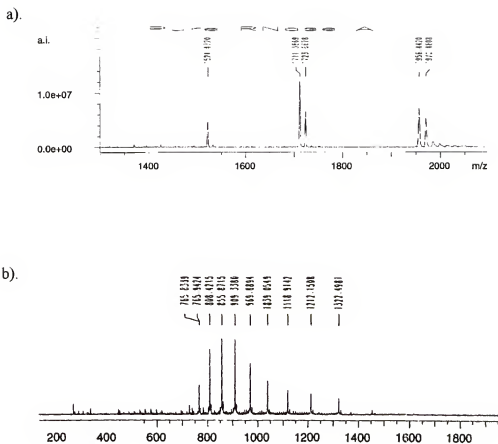


Figure 6-14.

The spectrum of the native RNase A is given in a), and the spectrum of the reduced form of RNase A is shown in b).

peptide mixture from the RNase A samples, a HPLC peptide standard mixture purchased from Sigma was used to test the reliability of HPLC and MS. The HPLC peptide standard mixture contains five peptides which are listed with their expected m/z values of 1^+ and their available 2^+ charge states in **Table 6-3**.

Table 6-3.

List of peptides, with their expected m/z values of 1^+ and the available 2^+ charge states, as contained in the HPLC standard peptide mixture purchased from Sigma Chemical Co. This peptide mixture is used to test the reliability of the reverse phase HPLC method and MS.

Peptide	m/z	Assignment
Gly-Try (1)	239.2	$(1 + H)^+$
Val-Try-Val(2)	380.2	$(2 + H)^+$
methionine enkephalin acetate (3)	574.3	$(3 + H)^+$
leucine enkephalin (4)	556.8	$(4 + H)^+$
	279.2	$(4 + 2H)^{2+}$
angiotensin II acetate (5)	1047.8	$(5 + H)^+$
	524.3	$(5 + 2H)^{2+}$

Figure 6-15 gives the complete spectrum of the peptide mixture with all five peptides simultaneously observed plus some unidentified peaks of low m/z . Peptide 1 at m/z 239.2 is seen with very weak intensity compared to others; the 2^+ charge states of 4 and 5 are also seen with strong intensities along with their 1^+ molecular ions; and the 1^+ charge states of peptides 2 and 3 are also clearly seen. The results obtained from this standard peptide mixture again illustrate the phenomenon that as a peptide gets larger, its charge states detected by MS also grow higher because larger proteins have more available sites for protonation.

The spectra in **Figures 6-16, 6-17, and 6-18** correspond to four HPLC fractions collected from the standard peptide mixture. In the first HPLC fraction, the MS spectrum a) reveals that the 1^+ charge state of the peptide 2 and the 2^+ charge state of the peptide 4

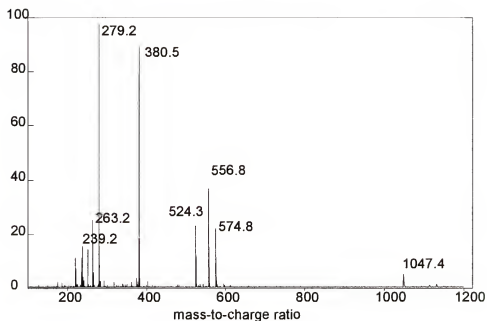


Figure 6-15.

Mass spectrum of the HPLC standard peptide mixture purchased from Sigma Chemical Co.

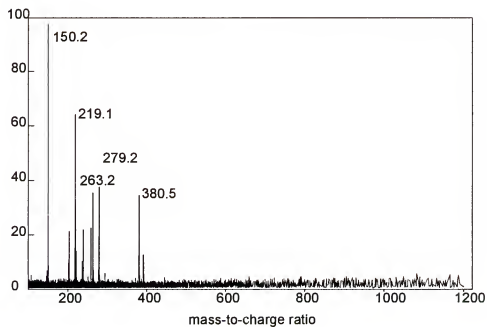


Figure 6-16.

Mass spectrum of the first HPLC aliquot collected from the HPLC standard peptide mixture.

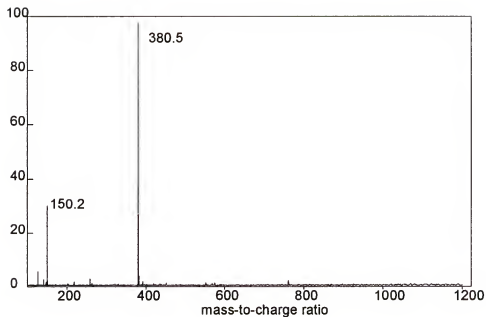


Figure 6-17.

Mass spectrum of the second HPLC aliquot collected from the HPLC standard peptide mixture.

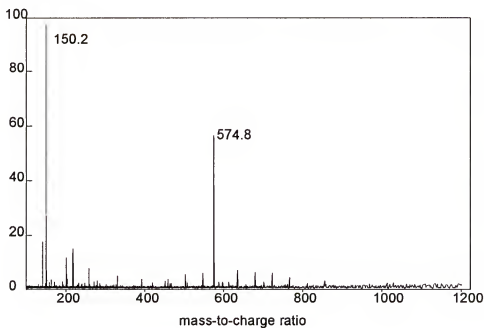


Figure 6-18.

Mass spectrum of the third HPLC aliquot collected from the HPLC standard peptide mixture.

are eluted together. The similar unidentified low m/z values seen in the peptide mixture are also seen in this HPLC fraction. One new peak at 150 is also seen in the first HPLC fraction, and it is due to some contaminations from the HPLC column since it is present in all other HPLC fractions but is absent from the peptide mixture spectrum given in **Figure 6-15**. The spectrum given in **Figure 6-17** shows that the majority of the 1^+ ions of the peptide **2** are collected in the second HPLC fraction. The spectrum given in **Figure 6-18** gives mainly the 1^+ ions of the peptide **3**.

Obviously, the results shown in **Figures 6-16 to 6-18** demonstrate that a HPLC separated peptide mixture can be unmistakably identified using ESI-FTICR/MS. These preliminary experiments confirm the capability of ESI-FTICR/MS to detect the HPLC aliquots, and show that the technique is ready to be used for investigating the digested native RNase A and its modified form to locate the exact modification site of the RNase A.

Conclusions and Future Work

Work performed on this project has demonstrated that ESI-FTICR/MS can be an important analytical technique for following chemical modifications of enzymes. The method can provide rapid sample purity screening for samples commercially bought or prepared in the laboratory. For example, the early detection of many contaminants at different stages of the project pointed out the need for sample cleaning before proceeding to the next stage. Due to its high mass resolving power characteristic, the ESI-FTICR/MS technique has been demonstrated to successfully and routinely identify the singly modified RNase A with N-hydroxysuccinimide acetate.

Studies of gas phase dissociation techniques with SORI-CAD, CS-CAD, and UV-visible photodissociation did not generate enough fragments for peptide sequencing in the gas phase. It seems likely that the combination of peptide mapping with MS detection will still be the best way to attack the problem of pinpointing the exact site of the protein modification. A proper method used to locate the exact modification site is still being intensively explored.

Much has been achieved on this project so far; however, considerable work still needs to be done in future. An outline of the future work needed to be done is shown in the flow chart of **Figure 6-19**. Once the exact modification site is accurately identified, a metal cofactor will be covalently bound to the modified protein, and then the reaction rate of the newly modified enzyme will be investigated. Of course, the FTMS technique will be one of the essential tools for every step of future studies.

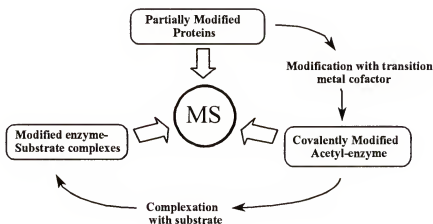


Figure 6-19.

An outline for the future work needed to be done on this project.

CHAPTER 7

CONCLUSIONS AND FUTURE WORK

As can be seen from the projects reported throughout this dissertation, Fourier transform ion cyclotron resonance mass spectrometry (FTICR/MS) is one of the most versatile analytical techniques for studying different chemical systems or different aspects of one particular system. Due to its ability to be interfaced with a variety of ionization sources, many classes of molecules which were previously not able to be introduced into the gas phase can now be studied with this technique. At present, FTICR/MS is being used to study organic, inorganic, organometallic, and large biological systems. The versatility of the technique is also illustrated by the results which can be obtained from one class of compounds, such as determination of the free energies of ionization for one organometallic complex and investigations of the reactivity of another organometallic complex. The same technique can be used to elucidate structural features of large or small biomolecules.

In chapter 3, the free energies of ionization of eight ruthenocene organometallic compounds with the general formula $(\eta^5\text{-C}_5\text{Me}_5)(\eta^5\text{-C}_5\text{H}_{5-n}\text{F}_n)\text{Ru}$ ($n = 0$ to 5), including two isomeric structures, were measured. The values determined ranged from 152.3 to 170.8 kcal/mol. Although the addition of each successive fluorine ligand to the ruthenocene complexes did not dramatically increase the free energy of ionization of the

compound, the ligand additivity effect is still seen in the results obtained. The studies also disproved the expectation that five fluorine ligands might cause the “perfluoro” effect within the ruthenocene compounds.

Investigations of the reactivity of a zirconium hydroxide complex, Cp_2ZrOH^+ (Cp = cyclopentadienyl), with selected organic compounds such as alcohols, esters, ethers, amines, and amides using external EI for ion formation showed that only the alcohol family gave a true ion/molecule reaction, producing the alkoxide complex, Cp_2ZrOR^+ . When the results from external EI studies were compared to these obtained using internal EI for ion formation, different reaction pathways were seen. For the alcohol family, both approaches for generating the ions gave rise to Cp_2ZrOR^+ after elimination of a water molecule during the reaction. The relative free energies of ionization for these Cp_2ZrOR^+ complexes were determined. The order of relative Zr-O bond strength for the alkoxide complexes studied was determined as: $\text{Cp}_2\text{ZrOH}^+ < \text{Cp}_2\text{ZrOCH}_3^+ < \text{Cp}_2\text{ZrOC}_2\text{H}_5^+ < \text{Cp}_2\text{ZrOCH}(\text{CH}_3)_2^+ < \text{Cp}_2\text{ZrOCHCH}_2(\text{CH}_3)_2^+ < \text{Cp}_2\text{ZrOC}(\text{CH}_3)_3^+$. Results obtained with the external EI technique showed that other families of organic compounds gave only adducts as primary products, while earlier internal EI experiments had suggested specific ion/molecule reactions.

FTICR/MS studies of biological molecules presented in this dissertation have shown that the technique can be used to study large biomolecules. MS sequencing of peptides or proteins in the gas phase has been demonstrated as a possible alternative method for traditional protein sequencing. Although the peptide mapping MS approach can be time saving for identifying an acetylated protein when compared to traditional chemical methods, MS alone is still not commonly used to sequence an unknown protein.

However, a more complete understanding of the general correlations between gas phase protein fragmentation and the location of an amino acid residue in the protein will be very helpful for sequencing an unknown protein. Since protein dissociation in the gas phase can be very complex, small peptides (6 or fewer amino acids) were studied to serve as models for larger biomolecules. The results of this study, reported in chapter 5, yielded three general correlations: b_n type ions are observed as the primary fragmentation series when an arginine(Arg) residue is located at the N-terminus of the peptide, y_n type ions are seen as the principal fragmentation series when the Arg residue is located at the C-terminus of the peptide, and a mixture of mainly b_n and y_n type ions is observed in the dissociation spectra when the Arg residue is located in the middle of the peptide sequence. The results obtained have also shown that the precursor ions of higher charge states provide more fragmentation information than the precursor ions of lower charge states. The IRMPD results obtained for all peptides studied are compatible with SORI-CAD results. However, the results of this work suggest that IRMPD is the better choice for peptide sequencing in the gas phase since it produces almost exclusively main peptide-backbone fragments.

The studies of ribonuclease A (RNase A) reported in chapter 6 illustrate another biological application of FTICR/MS. This work has demonstrated that FTICR/MS can provide rapid screening of the purity of samples. In addition, successful identification of a single modification of RNase A with N-hydroxysuccinimide acetate shows that ESI-FTICR/MS can be a novel tool for following chemical modifications of proteins. It can quickly measure molecular weights of unmodified and modified proteins to determine if modification has been accomplished. The work has indicated that SORI-CAD, skimmer

capillary (SC) dissociation, and photodissociation (PD) are less effective methods for sequencing large proteins in the gas phase. However, the peptide mapping mass spectrometric method has shown promising results. For future work, the next step is to examine digested peptide mixtures of both native and modified RNase A with ESI-FTICR/MS to identify the peptide fragment which contains the chemical modifier, followed by MSⁿ experiments to sequence the modified fragment and to pinpoint the exact modification site. Once the exact modification site is accurately located, the catalytic strength of the newly modified enzyme will be examined.

REFERENCES

1. Comisarow, M.B.; Marshall, A.G. *Chem.Phys.Lett.* **1974**, *25*, 282-283.
2. Aleksandrov, M.L.; Gall, L.N.; Drosnov, V.N.; Nikolaev, V.I.; Pavlenko, V.A.; Silirpv, V.A. *Dokl.Akad.Nauk, SSSR* **1984**, *277*, 379
3. Yamashita, M.; Fenn, J.B. *J.Phys.Chem.* **1984**, *88*, 4451
4. Anicich, V.G.; Kim, J.K.; Huntress, W.T. *Int.J.Mass Spectrom.Ion Phys* **1977**, *25*, 433
5. Anicich, V.G.; Sen, A.D.; Huntress, W.T., Jr.; McEwan, M.J. *J.Chem.Phys.* **1991**, *94*, 4189
6. Devlin, J.L., III; Wolf, J.F.; Hehre, W.J.; Taft, R. *J.Am.Chem.Soc.* **1976**, *98*, 1990
7. Sharpe, P.; Eyler, J.R.; Richardson, D.E. *Inorg.Chem.* **1990**, *29*, 2779
8. Bach, S.B.H.; Eyler, J.R. *J.Chem.Phys.* **1990**, *92*, 358
9. Parisod, G.; Comisarow, M.B. *Adv.Mass Spectrom.* **1980**, *8A*, 212-223.
10. Byrd, G.D.; Freiser, B.S. *J.Am.Chem.Soc.* **1982**, *104*, 5944-5950.
11. Jacobson, D.B.; Byrd, G.C.; Freiser, B.S. *J.Am.Chem.Soc.* **1982**, 2321-2323.
12. Richardson, D.E. in Freiser, B.S., Ed.; Kluwer Academic Publishers: Netherlands, 1996; pp 259-282.
13. Richardson, D.E.; Ryan, M.F.; Geiger, W.E.; Chin, T.T.; Hughes, R.P.; Curnow, O.J. *Organometallics* **1993**, *12*, 613-615.
14. Ryan, M.F.; Eyler, J.R.; Richardson, D.E. *J.Am.Chem.Soc.* **1992**, *114*, 8611-8619.
15. Zhu, L.G.; Qin, L.; Parac, J.N.; Kostic, N.M. *J.Am.Chem.Soc.* **1994**, *116*, 5218-5224.
16. Gultneh, Y.; Ahvazi, B.; Allwar, D.; Blaise, D.; Butcher, R.J.; Jasinski, J. *Inorg.Chim.Acta.* **1996**, *241*, 31-38.

17. Wahnon, D.; Bebuis, A.M.; Chin, J. *Angew.Chem.* **1995**, *34*, 2412-2414.
18. Takasaki, B.K.; Chin, J. *J.Am.Chem.Soc.* **1994**, *116*, 1121-1122.
19. Young, M.J.; Chin, J. *J.Am.Chem.Soc.* **1995**, *117*, 10577-10578.
20. Hillenkamp, F.; Karas, M.; Beavis, R.C.; Chait, B.T. *Anal.Chem.* **1991**, *63*, 1193A-1203A.
21. Smith, R.D.; Light-Wahl, K.J. *Biol.Mass Spectrom.* **1993**, *32*, 493
22. Ganem, B.; Li, Y.T.; Henion, J.D. *J.Am.Chem.Soc.* **1991**, *113*, 7818
23. Baca, M.; Kent, S.B.H. *J.Am.Chem.Soc.* **1992**, *113*, 8534
24. Goodlett, D.R.; Camp, D.G., II; Hardin, C.C.; Corregan, M.; Smith, R.D. *Biol.Mass Spectrom.* **1993**, *22*, 81
25. Busch, K.L.; Glish, G.L.; McLuckey, S.A. *Mass Spectrometry/Mass Spectrometry: Techniques and Applications of Tandem Mass Spectrometry*; VCH: New York, 1988
26. Nielsen, P.F.; Landis, B.; Svoboda, M.; Schneider, M.; Przybylski, M. *Anal.Biochem.* **1990**, *191*, 302
27. Roepstorff, P.; Nielsen, P.F.; Klarskov, K.; Hojrup, P. *Biomed.Env.Mass Spectrom.* **1988**, *16*, 9-18.
28. Svoboda, M.; Przybylski, M.; Schreurs, J.; Miyajima, A.; Hogeland, K.; Deinzer, M.L. *J.Chromatogr.* **1991**, *562*, 403-411.
29. Glocker, M.O.; Arbogast, B.; Schreurs, J.; Deinzer, M.L. *Biochemistry* **1993**, *32*, 482-488.
30. Mann, M.; Wilm, M. *Trends Biochem.Sci.* **1995**, *20*, 219-224.
31. Gauthier, J.W.; Trautman, T.R.; Jacobson, D.B. *Anal.Chim.Acta.* **1991**, *246*, 211-225.
32. Chapman, J.R. *Practical Organic Mass Spectrometry*; Wiley: Chichester, UK, 1993
33. Chapman, J.R. *Methods in Molecular Biology Volume 61: Protein and Peptide Analysis by Mass Spectrometry*; Humana Press, Inc.: New Jersey, 1996
34. Bose, G.M. *Recherches sur le cause ef sur vèritable théorie de l'-électicité*; Wittenberg: 1745

35. Dole, M.; Mack, L.L.; Hines, R.L.; Mobley, R.C.; Ferguson, L.D.; Alice, M.B. *J.Chem.Phys.* **1968**, *49*, 2240-2249.
36. Mack, L.L.; Kralik, P.; Dole, M. *J.Chem.Phys.* **1970**, *52*, 4977-4986.
37. Ashton, D.S.; Beddell, C.R.; Cooper, D.J.; Green, B.N.; Oliver, R.W.A. *Org.Mass Spectrom.* **1993**, *28*, 721-728.
38. Kebarle, P.; Tang, L. *Anal.Chem.* **1993**, *65*, 972-986.
39. Iribarne, J.V.; Thomson, B.A. *J.Chem.Phys.* **1976**, *64*, 2287
40. Thomson, B.A.; Iribarne, J.V. *J.Chem.Phys.* **1979**, *71*, 4451
41. Rayleigh, L. *Philos.Mag.* **1882**, *14*, 184
42. Dawson, P.H. *Quadrupole Mass Spectrometry and Its Applications*; Elsevier: New York, 1976
43. Duckworth, E.; Barber, R.C.; Venkatasubramanian, V.S. *Mass Spectroscopy*; Cambridge University Press: Cambridge, UK, 1988
44. Cotter, R.J. *Anal.Chem.* **1992**, *64*, 1027A-1039A.
45. Vestal, M.L.; Juhasz, P.; Martin, S.A. *Rapid Commun.Mass Spectrom.* **1995**, *9*, 1044-1050.
46. March, R.E.; Hughes, R.J. *Quadrupole Storage Mass Spectrometry*; Wiley: New York, 1989
47. Buchanan, M.V. *Fourier Transform Mass Spectrometry: Evolution, Innovation, and Applications*; ACS Symposium Series: Washington D.C., 1987
48. Lawrence, E.O.; Livingston, M.S. *Phys.Rev.* **1932**, *40*, 19
49. Sommer, H.; Thomas, H.A.; Hipple, J.A. *Phys.Rev.* **1951**, *82*, 697
50. Wobschall, D. *Rev.Sci.Instrum.* **1965**, *36*, 466
51. Wobschall, D.; Graham, J.R., Jr.; Malone, D.P. *Phys.Rev.* **1963**, *131*, 1565
52. Marshall, A.G. In *Encyclopedia of NMR*; Grant, P.M., Harris, R.K., Eds.; Wiley: London, 1996; pp 486-489.
53. Comisarow, M.B.; Marshall, A.G. *Chem.Phys.Lett.* **1974**, *26*, 489-490.
54. Guan, S.; Marshall, A.G. *Int.J.Mass Spectrom.Ion Processes* **1995**, *146/147*, 261-296.

55. Baykut, G.; Eyler, J.R. *Trends in Analytical Chemistry* **1986**, *5*, 44-49.
56. Comisarow, M.B. *Hyperfine Interactions* **1993**, *81*, 171-178.
57. Laude, D.A., Jr.; Johlman, C.L.; Brown, R.S.; Weil, D.A.; Wilkins, C.L. *Mass Spectrom.Rev.* **1986**, *5*, 167
58. Marshall, A.G.; Grosshans, P.B. *Anal.Chem.* **1991**, *63*, 215A
59. Nibbering, N.M.M. *Analyst* **1992**, *117*, 289-293.
60. Jeffries, J.B.; Barlow, S.E.; Dunn, G.H. *Int.J.Mass Spectrom.Ion Proc.* **1983**, *54*, 169-187.
61. Marshall, A.G.; Grosshans, P.B. *Anal.Chem.* **1991**, *63*, 215-229.
62. Vartanian, V.H.; Anderson, J.S.; Laude, D.A., Jr. *Mass Spectrom.Rev.* **1995**, *14*, 1-19.
63. Comisarow, M.B. *Int.J.Mass Spectrom.Ion Phys* **1982**, *37*, 251-257.
64. Marshall, A.G.; Wang, T.C.L.; Ricca, T.L. *J.Am.Chem.Soc.* **1985**, *107*, 7893
65. Kofel, P.; Allemann, M.; Dellerhals, H.; Wanczek, K.P. *Int.J.Mass Spectrom.Ion Proc.* **1985**, *65*, 97
66. Allemann, M.; Kofel, P.; Kellerhals, H.; Wanczek, K.P. *Int.* **1987**, *75*, 47
67. van der Hart, W.J.; Van de Guchte, W.J. *Int.J.Mass Spectrom.Ion Proc.* **1988**, *82*, 17
68. Wang, M.; Marshall, A.G. *Anal.Chem.* **1990**, *62*, 515
69. Hanson, C.D.; Castro, M.E.; Kerley, E.L.; Russel, D.H. *Anal.Chem.* **1990**, *62*, 520
70. Caravatti, P.; Allemann, M. *Org.Mass Spectrom.* **1991**, *29*, 514-518.
71. McIver, R.T., Jr.; Baykut, G.; Hunter, R.L. *Int.J.Mass Spectrom.Ion Proc.* **1989**, *89*, 343
72. Asamoto, B. *FT-ICR/MS: Analytical Applications of Fourier Transform Ion Cyclotron Resonance Mass Spectrometry*; VCH: Weinheim, Germany, 1991
73. Marshall, A.G.; Guan, S. *Rapid Commun.Mass Spectrom.* **1996**, *10*, 1819-1823.
74. Schweikhard, L.; Guan, S.; Marshall, A.G. *Int.J.Mass Spectrom.Ion Processes* **1992**, *120*, 71-83.
75. Allemann, M.; Kellerhals, H.; Wanczek, K.P. *Chem.Phys.Lett* **1980**, *75*, 328

76. Jennings, K.R. *Int.J.Mass Spectrom.Ion Phys* **1968**, *1*, 227-235.
77. Haddon, W.F.; McLafferty, F.W. *J.Am.Chem.Soc.* **1968**, *90*, 4745-4746.
78. Rodgers, M.T.; Campbell, S.; Marzluff, E.M.; Beauchamp, J.L. *Int.J.Mass Spectrom.Ion Proc.* **1994**, *137*, 121-149.
79. Senko, M.W.; Speir, J.P.; McLafferty, F.W. *Anal.Chem.* **1994**, *66*, 2801-2808.
80. Little, D.P.; Speir, J.P.; Senko, M.W.; O'Connor, P.B.; McLafferty, F.W. *Anal.Chem.* **1994**, *66*, 2809-2815.
81. Chen, J.H.; Hays, J.D.; Dunbar, R.C. *J.Phys.Chem.* **1984**, *88*, 4759-4764.
82. Ranatunga, D.R.A.; Freiser, B.S. *Chem.Phys.Lett* **1995**, *233*, 319-323.
83. McLuckey, S.A. *J.Am.Chem.Soc.* **1992**, *3*, 599-614.
84. Cooks, R.G. *J.Mass Spectrom.* **1995**, *30*, 1215-1221.
85. Cody, R.B.; Burnier, R.C.; Freiser, B.S. *Anal.Chem.* **1982**, *54*, 96-101.
86. Williams, E.R.; Henry, K.D.; McLafferty, F.W. *J.Am.Chem.Soc.* **1990**, *112*, 6157-6177.
87. Guan, S.; Hofstadler, S.A.; Laude, D.A., Jr. *Anal.Chem.* **1993**, *65*, 1588-1593.
88. Boering, K.A.; Rolfe, J.; Brauman, J.I. *Rapid Commun.Mass Spectrom.* **1992**, *6*, 303-305.
89. Smith, R.D.; Loo, J.A.; Edmonds, C.G.; Barinaga, C.J.; Udseth, H.R. *Anal.Chem.* **1990**, *62*, 882-899.
90. Little, D.P.; Chorush, R.A.; Speir, J.P.; Senko, M.W.; Kelleher, N.L.; McLafferty, F.W. *J.Am.Chem.Soc.* **1994**, *116*, 4893-4897.
91. Mabud, M.A.; Dekrey, M.J.; Cooks, R.G. *Int.J.Mass Spectrom.Ion Proc.* **1985**, *67*, 285-294.
92. Cody, R.B.; Freiser, B.S. *Anal.Chem.* **1987**, *59*, 1054-1056.
93. Gord, J.R.; Horning, S.R.; Wood, J.M.; Cooks, R.G.; Freiser, B.S. *J.Am.Soc.Mass Spectrom.* **1992**, *4*, 145-151.
94. Peiris, D.M.; Cheeseman, M.A.; Ramanathan, R.; Eyler, J.R. *J.Phys.Chem.* **1993**, *97*, 7839-7843.
95. Price, W.D.; Schnier, P.D.; Williams, E.R. *Anal.Chem.* **1996**, *68*, 859-866.

96. Loo, J.A.; Udseth, H.R.; Smith, R.D. *Rapid Commun.Mass Spectrom.* **1998**, *2*, 207-210.
97. Beauchamp, J.L.; Martinbo, S. *J.A.Chem.Rev.* **1990**, *90*, 629
98. Franklin, A.J.L.; Dillard, J.G.; Rosenstock, H.M.; Herron, J.T.; Draxl, K.; Field, F.H. *Nat.Stand.Ref.Data Ser., Nat.Bur.Stand.* **1969**, *26*, 1
99. Levin, R.D.; Lias, S.G. *Nat.Stand.Ref.Data Ser., Nat.Bur.Stand.* **1982**, *71*, 1
100. Rosenstock, H.M.; Draxl, K.; Steiner, B.W.; Herron, J.T. *J.Phys.Chem.Ref.Data* **1977**, *6*, 1
101. Skinner, H.A.; Conner, J.A. *Pure Appl.Chem.* **1985**, *57*, 79
102. Green, J.C. *Struct.Bonding* **1986**, *43*, 37
103. Rabalais, J.W. *Principles of Ultraviolet Photoelectron Spectroscopy*; Wiley-Interscience: New York, 1977
104. Lias, S.G.; Bartmess, J.E.; Liebman, J.F.; Holmes, J.L.; Levin, R.D. *Gas-phase Ion and Neutral Thermochemistry*; American Institute of Physics: New York, 1988
105. Nelsen, S.F.; Rumack, D.T.; Meot-Ner(Mautner), M. *J.Am.Chem.Soc.* **1988**, *110*, 7945-7952.
106. Curnow, O.J.; Hughes, R.J. *J.Am.Chem.Soc.* **1992**, *114*, 5895
107. Hughes, R.P.; Zheng, X.; Ostrander, R.L.; Rheingold, A.L. *Organometallics* **1994**, *13*, 1567
108. Ryan, M.F.; Siedle, A.R.; Burk, M.F.; Richardson, D.E. *Organometallics* **1992**, *11*, 4231
109. Bruce, J. E. *Kinetic Energies and Reactions of Trapped Ions in a Fourier Transform Ion Cyclotron Resonance Mass Spectrometer*, 1993, University of Florida, Ph. D. Dissertation.
110. Lias, S.G.; Ausllos, P. *J.Am.Chem.Soc.* **1978**, *100*, 6027
111. Lias, S.G.; Jackson, J.A.; Argenian, H.; Liebman, J.F. *J.Org.Chem.* **1985**, *50*, 333
112. Meot-Ner(Mautner), M.; Nelsen, S.F.; Wili, M.R.; Frigo, T.B. *J.Am.Chem.Soc.* **1984**, *106*, 7384
113. Hartnup, M. *Ester Hydrolysis Catalysis by a Zinc Enzyme Model Complex and Synthesis of a Bioconjugatable Model Complex Derivative*, 1994, University of Florida, Ph. D. Dissertation.

114. *Handbook of Chemistry and Physics*; CRC Press, Inc.: Boston, 1990, pp 5-16 and 9-86.
115. Bartmess, J.E.; Georgiadis, R.M. *Vacuum* **1983**, *33*, 149
116. Vachet, R.W.; Bishop, B.M.; Erickson, B.W.; Glish, G.L. *J.Am.Chem.Soc.* **1997**, *119*, 5481-5488.
117. Vachet, R.W.; Asam, M.B.; Glish, G.L. *J.Am.Chem.Soc.* **1996**, *118*, 6252-5256.
118. Peiris, D.M.; Yang, Y.J.; Ramanathan, R.; Williams, K.R.; Watson, C.H.; Eyler, J.R. *Int.J.Mass Spectrom.Ion Proc.* **1996**, *157/158*, 365-378.
119. Zimmerman, J.A.; Watson, C.H.; Eyler, J.R. *Anal.Chem.* **1991**, *63*, 361-365.
120. Dienes, T.; Pastor, S.J.; Schurch, S.; Scott, J.R.; Yao, J.; Cui, S.; Wilkins, C.L. *Mass Spectrom.Rev.* **1996**, *15*, 163-211.
121. Deery, M.J.; Summerfield, S.G.; Buzy, A.; Jennings, K.R. *J.Am.Soc.Mass Spectrom.* **1997**, *8*, 253-261.
122. Vath, J.E.; Bishop, B.M. *Int.J.Mass Spectrom.Ion Processes* **1988**, *86*, 137
123. Senko, M.W.; Hendrickson, C.L.; PasaTolic, L.; Marto, J.A.; White, F.M.; Guan, S.; Marshall, A.G. *Rapid Commun.Mass Spectrom.* **1996**, *10*, 1824-1828.
124. Chowdhury, S.K.; Katta, V.; Chait, B.T. *Rapid Commun.Mass Spectrom.* **1990**, *4*, 81
125. Gabrielse, G.; Haarsma, L.; Rolston, S.L. *Int.J.Mass Spectrom.Ion Processes* **1989**, *88*, 319
126. Ikononov, M.G.; Kebarle, P. *J.Am.Soc.Mass Spectrom.* **1994**, *5*, 791
127. Roepstorff, P. *Biomedical Mass Spectrometry* **1984**, *11*, 601
128. Biemann, K. *Biochemical Application of Mass Spectrometry*; Wiley: New York, 1972, 405
129. Buko, A.M.; Phillips, L.R.; Fraser, B. *Biomed.Mass Spectrom.* **1983**, *10*, 387
130. Hunt, D.F.; Zhu, N.Z.; Shabanowitz, J. *Rapid Commun.Mass Spectrom.* **1989**, *3*, 122
131. Biemann K. *Methods Enzymol.* **1990**, *193*, 455
132. Wu, Z.; Fensleau, C. *Rapid Commun.Mass Spectrom.* **1992**, *6*, 403-405.
133. Harrison, A.G. *Mass Spectrom.Rev.* **1997**, *16*, 201-217.

134. Biemann K. *Biomed. Environ. Mass Spectrom.* **1988**, *16*, 99-111.
135. Johnson, R.S.; Martin, S.A.; Biemann, K.; Stults, J.T.; Watson, J.T. *Anal. Chem.* **1987**, *59*, 2621
136. Fang, K.; Hashimoto, M.; Jockusch, S.; Turro, N.J.; Nakanishi, K. *J. Am. Chem. Soc.* **1998**, *120*, 8543-8544.
137. Kristensen, C.; Wiberg, F.C.; Schaffer, L.; Andersen, A.S. *J. Biol. Chem.* **1998**, *273*, 19190-19197.
138. Fouques, D.; Ralet, M.C.; Molle, D.; Leonil, J.; Meunier, J.C. *Nahrung* **1998**, *42*, 148-150.
139. Nettleton, E.J.; Sunde, M.; Lai, Z.H.; Kelly, J.W.; Dobson, C.M.; Robinson, C.V. *J. Biol. Chem.* **1998**, *281*, 553-564.
140. Prieto, J.A.; Jimenez, R.M.; Alonso, R.M. *J. Chromatogr. B.* **1998**, *714*, 285-292.
141. Kussmann, M.; Roepstorff, P. *Spectrosc-Int. J.* **1998**, *14*, 1-27.
142. Ransom, W.D.; Lao, P.C.; Gage, D.A.; Boss, W.F. *Plant Physiol.* **1998**, *117*, 949-960.
143. Fiedler, W.; Borchers, C.; Macht, M.; Deininger, S.O.; Przybylski, M. *BioConjugate Chem.* **1998**, *9*, 236-241.
144. Laidler, P.; Cowan, D.A.; Houghton, E.; Kicman, A.T.; Marshall, D.E. *Rapid Commun. Mass Spectrom.* **1998**, *12*, 975-981.
145. Suckau, D.; Mák, M.; Przybylski, M. *Proc. Natl. Acad. Sci.* **1992**, *89*, 5630-5634.
146. Burrell, M.M. *Enzymes of Molecular Biology-methods in Molecular Biology*; Humana Press Inc.: 1993.
147. Wladkowski, B.D.; Svensson, L.A.; Sjolín, L. *J. Am. Chem. Soc.* **1998**, *120*, 5488-5498.
148. Glocker, M.O.; Borchers, D.; Fiedler, W.; Suckau, D.; Przybylski, M. *BioConjugate Chem.* **1994**, *5*, 583-590.
149. Camilleri, P.; Haskins, N.J.; Rudd, P.M.; Saunders, M.R. *Rapid Commun. Mass Spectrom.* **1993**, *7*, 332
150. Burlingame, A.L.; Carr, S.A. *Mass Spectrometry in the Biological Science*; Humann Press: 1996.

151. Bruce, J.E.; Hofstadler, S.A.; Winger, B.E.; Smith, R.D. *Int.J.Mass Spectrom.Ion Processes* **1994**, *132*, 97-107.
152. Lindsay, D.G.; Shall, S. *Biochem.J.* **1971**, *121*, 737-745.
153. Loo, J.A.; Edmonds, C.G.; Smith, R.D. *Science* **1990**, *243*, 201-204.

BIOGRAPHICAL SKETCH

Gui-hua Lisa Lang was born on July 29, 1969, in LiaoNing, China. She spent her childhood years in a small beautiful village and attended the elementary school which was about two minutes walking distance from home. During her elementary school years, she experienced the famous Chinese cultural revolution, and tasted the consequences of being a granddaughter of a wealthy landowner, Huilin Lang, who owned a lot of land and almost the whole village before the communist party took control of China in 1949. Due to the family wealth, her family became the labeled people whom the communist party condemned. After losing everything to the communist headquarters of the village, the family found no place to live and no food to eat. She still vividly remembers those days when the family was without any food to eat. Although she was a very good student in her elementary school, she was not allowed to join the Young Pioneer club which was supposed to be made up of “good students.”

After finishing her middle high school education in a boarding school, which was about an half hour walking distance from home, she attended a boarding high school, which took two hours by train after a one hour walk to the train station. Before she completed her freshman year in high school, she immigrated to the United States with her family to reunite with her uncle in August 1985.

Since then, Northern Virginia has become her “home sweet home.” There she attended Washington and Lee High School in Arlington, Virginia for two years, then

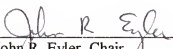
moved to Stonewall Jackson High School in Manassass , Virginia, where she completed her high school education in 1989. Without any previous knowledge of the language, she attended the English as second language (ESL) classes to learn English for two years at Washington and Lee. After transferring to Stonewall Jackson, she was admitted to regular English classes since ESL class was not offered there. Due to the time lost for taking ESL classes, she was two years behind in her English requirement to graduate from Stonewall Jackson, so she attended every summer school, including the summer of 1989, to fulfil the language requirement. Even though her language was poor during the high school years, her science background was strong. In the spring semester of her junior year at Stonewall Jackson, she had already finished taking the highest mathematics class (1st semester of calculus) the school offered at the time, so the school sent her to a local college for higher math classes. For convenience, she chose a local branch of Northern Virginia Community College which was about 15 minutes driving distance from home to complete the 2nd and 3rd semesters of calculus and two classes including ordinary and differential equations. At Stonewall Jackson, she was inducted into the National Honor Society and graduated with honors. During the last two years of high school, Lisa also helped out at the family restaurant as hostess, bar tender, and waitress.

In the fall of 1989, Lisa started her college education at Mary Washington College (MWC), a four year liberal arts and science school, where she double majored in chemistry and mathematics with strong interest in physics. She obtained her B.S. degree in May of 1993. During the summer of her junior year, through a research experience for undergraduate students (REU) program, she joined Dr. Michael A. Duncan's laboratory at the University of Georgia to conduct laser spectroscopic research on metal clusters such

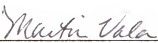
as Al-CO₂ with time-of-flight mass spectrometry. In the senior year, she studied molecular orbitals of aluminum complexes by using semi-empirical methods under the direction of Dr. John K. George. At MWC, Lisa was involved in community service and served in various positions such as vice president or secretary for various clubs such as the local chapter of American Chemical Society, Asian Students Association, and the Citizens of the World Club. During her years at MWC she received honors including Kiwanis Awards, Outstanding General Chemistry Student Award, Chi Beta Phi Scholarship, and Cook Chemistry Scholarship, and she was also inducted into different honor societies including Phi Beta Kappa, Alpha Phi Sigma, Mortar Board, and Pi Mu Epsilon.

In the fall of 1993, she joined the chemistry graduate program with a chemical physics scholarship at the University of Florida, Gainesville, Florida. Shortly thereafter, she affiliated with Professor John R. Eyler's laboratory with her research focus on exploring several applications of Fourier transform ion cyclotron resonance mass spectrometry.

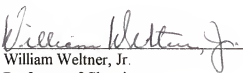
I certify that I have read this study and that in my opinion it conforms to acceptable standards of scholarly presentation and is fully adequate, in scope and quality, as a dissertation for the degree of Doctor of Philosophy.


John R. Eyler, Chair
Professor of Chemistry

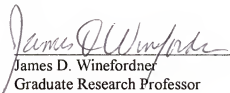
I certify that I have read this study and that in my opinion it conforms to acceptable standards of scholarly presentation and is fully adequate, in scope and quality, as a dissertation for the degree of Doctor of Philosophy.


Martin T. Vala
Professor of Chemistry

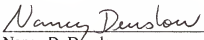
I certify that I have read this study and that in my opinion it conforms to acceptable standards of scholarly presentation and is fully adequate, in scope and quality, as a dissertation for the degree of Doctor of Philosophy.


William Weltner, Jr.
Professor of Chemistry

I certify that I have read this study and that in my opinion it conforms to acceptable standards of scholarly presentation and is fully adequate, in scope and quality, as a dissertation for the degree of Doctor of Philosophy.


James D. Winefordner
Graduate Research Professor
of Chemistry

I certify that I have read this study and that in my opinion it conforms to acceptable standards of scholarly presentation and is fully adequate, in scope and quality, as a dissertation for the degree of Doctor of Philosophy.


Nancy D. Denslow
Associate Scientist of Biochemistry
and Molecular Biology

This dissertation was submitted to the Graduate Faculty of the Department of Chemistry in the College of Liberal Arts and Sciences and to the Graduate School and was accepted as partial fulfillment of the requirements for the degree of Doctor of Philosophy.

December, 1998

Dean, Graduate School